

**Department of Physics and Astronomy
University of Heidelberg**

Master Thesis in Physics
submitted by

Mathias Neidig

born in Bad Friedrichshall

2013

A realization of a two-dimensional Fermi gas in a standing wave trap

This Master Thesis has been carried out by Mathias Neidig at the
Physikalisches Institut Heidelberg
under the supervision of
Prof. Selim Jochim

Abstract

This thesis reports on the progress towards the realization of an ultracold three-component Fermi gas of ${}^6\text{Li}$ in a two-dimensional optical lattice.

A standing wave of pancake shaped optical dipole traps in vertical direction was set up and ultracold atoms were transferred into these traps from the optical dipole trap in which the evaporative cooling is performed. In these pancake shaped traps the atoms are tightly confined in the vertical direction, thereby creating a quasi two-dimensional confinement. The relative intensity noise of the trap laser was measured and it was shown that noise induced heating is negligible in the experiment.

We measured the aspect ratio of the trap frequencies to be 1.2:1:357, thereby confirming the tight confinement in the vertical direction as well as the approximate cylindrical symmetry of the trap in the horizontal plane. The lifetime of atoms in the traps was measured to be approximately 50 s which is long enough to observe dynamics in the lattice without being severely limited by hole heating. Using Kapitza-Dirac diffraction, we were able to confirm the spacing between the traps of about $4\ \mu\text{m}$ as well as estimate the trap depth. To measure the population in each trap we employed a radio-frequency tomographic measurement. With this method we were able to count the number of atoms in each trap individually and show that long term phase drifts of the trap positions are smaller than $\pi/8$.

Zusammenfassung

Diese Arbeit beschreibt den Fortschritt hinsichtlich der Realisierung eines ultrakalten drei-komponentigen Fermi-Gases aus ${}^6\text{Li}$ in einem zweidimensionalen optischen Gitter.

Eine stehende Welle oblatenförmiger optischer Dipolfallen in vertikaler Richtung wurde aufgebaut und ultrakalte Atome wurden aus einer elliptisch, langgestreckten optischen Dipolfalle, in der das evaporative Kühlen stattfindet, in diese umgeladen. In diesen Fallen sind die Atome sehr stark in der vertikalen Richtung eingeschlossen wodurch ein quasi zweidimensionaler Einschluss der Atome erreicht wird. Eine Messung des relativen Intensitätsrauschen des Fallen-Lasers konnte nachweisen, dass das durch Rauschen verursachte Heizen im Experiment vernachlässigbar ist.

Wir haben das Verhältnis der Fallenfrequenzen als 1.2:1:357 gemessen und damit den starken Einschluss in der vertikalen Richtung sowie die annähernd zylindrisch-symmetrische Form der Fallen in der horizontalen Ebene bestätigt. Die Lebensdauer der Atome in den Fallen beträgt ungefähr 50 s, was ausreichend ist um dynamische Prozesse im Gitter zu beobachten ohne durch Loch-Heizen beschränkt zu sein. Mittels Kapitza-Dirac Beugung konnten wir den geplanten Abstand zwischen den Fallen von $4\ \mu\text{m}$ bestätigen sowie die Fallentiefe abschätzen. Um die Atomzahl in den einzelnen Fallen zu messen, haben wir eine tomographische Radio-Frequenz Spektroskopie angewandt. Mit dieser Methode konnten wir die Atomzahl in den einzelnen Fallen bestimmen und wir konnten zeigen, dass Phasenänderungen der Fallenpositionen auf lange Sicht kleiner als $\pi/8$ sind.

Contents

1. Introduction	1
2. Theory of Ultracold Atoms and Optical Trapping	5
2.1. Ideal Fermi Gas	5
2.2. Ultracold Scattering	6
2.3. Feshbach Resonances	11
2.4. Properties of Lithium	15
2.5. Optical Trapping	18
2.5.1. Crossed Beam Traps	23
2.5.2. Heating in Optical Traps	24
3. Experimental Setup	27
3.1. Preparation of an Ultracold Fermi Gas	27
3.1.1. Experimental Control	27
3.1.2. Vacuum, Oven & Experiment Chamber	29
3.1.3. Laser Cooling and Magneto-Optical Trapping	30
3.1.4. Transfer into the Optical Dipole Trap and Evaporative Cooling	35
3.2. The Pancake Trap Setup	37
3.2.1. Optical Setup	38
3.2.2. Noise Characterization	41
3.3. Radio-Frequency Setup	49
3.4. Imaging	50
4. Characterization of the Pancake Trap	53
4.1. Transfer into the Pancake Trap	53
4.2. Trap Frequencies in the Pancake Trap	54
4.3. Lifetime in the Pancake Trap	56
4.4. Making the Pancakes visible: Kapitza-Dirac Diffraction	58
4.4.1. Basics of Kapitza-Dirac Diffraction	59
4.4.2. Experimental Results	61
4.5. Counting the Filled Pancakes: Radio-Frequency Tomography	65
4.5.1. Basics on Radio-Frequency Transitions	65
4.5.2. Experimental Results	68
4.6. Towards the Preparation of Only a Single Pancake	77

5. Conclusion and Outlook	81
A. Fundamental Constants and Properties of Lithium	85
B. Noise Characterization of the NUFERN	87
Bibliography	97

1. Introduction

The complexity of a quantum many-body system scales exponentially with the particle number. Thus, the resources required to calculate e.g. the time evolution of such a system with classical computers increase very rapidly even for moderate particle numbers. This poses a major challenge when investigating theoretical models and one can often only satisfactorily describe the physics in certain parameter regimes. To solve this dilemma, R. Feynman proposed the use of a universal quantum simulator [Fey82]. Such a hypothetical quantum computer would allow to compute any quantum system of interest. In contrast to such a universal quantum simulator, it has become feasible in recent years to use controllable quantum systems where the Hamiltonian is well known to mimic specific systems which are not easily accessible experimentally but share essential properties. Then all results obtained with these quantum simulators can be directly applied to the mimicked system.

In 1995, the first experimental realization of a Bose-Einstein condensate (BEC) of ultracold bosonic atoms [And95, Dav95] demonstrated spectacularly that trapped dilute clouds of ultracold atoms can act as such controllable quantum systems. The importance of this milestone was highlighted by the fact that E. A. Cornell, C. E. Wieman and W. Ketterle were awarded the Nobel prize already in 2001. A few years after the first BEC, also the first quantum degenerate gas of fermionic atoms was achieved [DeM99] in 1999.

Ultracold atoms are perfectly suited as quantum simulators since the trapping potential and thus the confinement of the atoms can be controlled very precisely. In addition, by applying homogeneous magnetic offset fields it is possible to tune the interaction strength between the atoms via so-called Feshbach resonances [Ino98]. This controllability of the confinement and the interactions makes these systems a powerful tool to investigate theoretical models as one can access different parameter regimes in a very controlled manner with the same setup.

A research field where ultracold atoms have proved to be very successful in recent years is condensed matter physics. For example it was long known that some materials are insulators although they were predicted to be conductors by band theory. N. Mott explained this phenomena already in 1937, showing that the tunneling of the electrons can be suppressed when the interaction between them dominates their behavior [Mot37]. The simplest theoretical model which can describe this transition is the Fermi-Hubbard model which has two free parameters: the tunneling rate and the interaction energy. Studying this model in a solid-state system however is challenging since one has to deal with finite size effects, defects in the lattice and most importantly the fixed coulomb interaction between the electrons.

Ultracold fermions trapped in an optical lattice however do not have these limitations. There the lattice is perfectly periodical and both the tunneling rate and the interaction strength can be controlled independently. Two distinguishable fermions -

either different atomic species or different internal states of the same atomic species - can then be directly mapped onto the up and down spin configuration of the electrons in the metal and thus it is possible to observe the transition from a tunneling dominated superfluid phase to the Mott-insulating phase. The emergence of the Mott-insulator phase was experimentally first shown in a one-component bosonic gas [Gre02], which is governed by the Bose-Hubbard model, and then later for a two-component fermionic mixture [Jör08, Sch08].

In nature there are of course more complex fermionic systems than the simple spin-1/2 configuration of the electrons in a solid. Thus by adding a third distinguishable fermion to the mixture one can study new phenomena which are related to high-energy physics like color superfluidity or baryon formation [Rap07, Rap08, Wil07]. The first step towards such a system was done in our group in 2008 with the first realization of a quantum degenerate three-component Fermi gas of ${}^6\text{Li}$ atoms [Ott08]. There the three distinguishable fermions were realized by the three lowest Zeeman sublevels of the electronic ground state. ${}^6\text{Li}$ is a perfect candidate for such studies since the two-body interactions between the different states all have broad Feshbach resonances which overlap and thus the interaction between all the states can be simultaneously tuned. In addition, for high magnetic fields the interactions between the different states are approximately equal and thus the system has an almost perfect SU(3) symmetry.

In the interesting regime of strong interactions however, a three-component mixture is short-lived because inelastic three-body collisions¹ then dominate which lead to strong atom losses from the trap. To circumvent this inherent loss it was proposed to put the three-component mixture in an optical lattice. Then so-called Quantum-Zeno loss blocking should occur which suppresses tunneling of atoms onto already doubly occupied sites and therefore stabilizes the sample [Dal09, Kan09]. The system is then stable on time scales which should be large enough to observe phase transitions like the aforementioned color superfluid [Pri11] or the emergence of off-site trions [Poh13]. In our experiment we want to investigate such a three-component Fermi gas in a two-dimensional optical lattice. A sketch of our planned preparation scheme can be seen in Figure 1.1. After laser cooling the atoms in a magneto-optical trap (MOT), we transfer them into an optical dipole trap where we do evaporative cooling to prepare a quantum degenerate two-component mixture. Then we transfer the atoms into another optical dipole trap which is strongly confined in the vertical direction and only weakly confined in the horizontal plane and hence provides a quasi two-dimensional confinement. Ramping up the optical lattice and transferring a fraction of the atoms into the third spin state using radio-frequency transitions, we will then prepare a three-component Fermi gas in a 2D optical lattice.

During this thesis, the optical setup to create the round, flat trapping potential for the quasi 2D confinement was implemented and the properties of the trapping potential were measured.

¹These collisions lead to the formation of Efimov trimers which are an interesting field of research in themselves and have also been studied in our group [Ott08, Wen09, Lom10b, Lom10a].

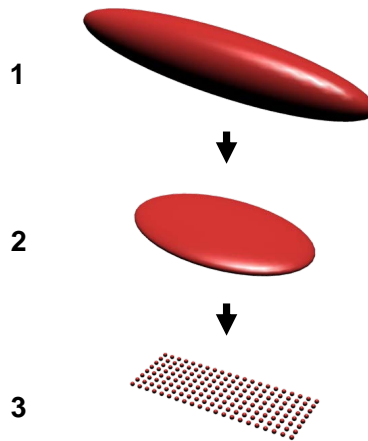


Figure 1.1.: **Scheme to create a three-component Fermi gas in a 2D optical lattice.** A two-component Fermi mixture is evaporatively cooled into quantum degeneracy in a 3D optical dipole trap (1). The atoms are then transferred into a second optical dipole trap with a large aspect ratio (2), which leads to a quasi 2D confinement of the atoms. Then the standing light waves are ramped up to create the optical lattice (3). The picture is taken from [Rie10].

Outline of the thesis

This master thesis is structured as follows: It starts in Chapter 2 with a summary of the basic theory of the interactions in ultracold Fermi gases, especially the concept of the scattering length and Feshbach resonances. Since the thesis also deals with the characterization of an optical dipole trap, the basics of optical dipole trapping are reviewed in this chapter as well. Then in Chapter 3 the experimental apparatus is described. At first the status quo at the beginning of the master thesis is summarized before introducing the parts which were implemented in the course of this thesis. This includes the optical setup we use to create the quasi 2D confining potential as well as a characterization of the noise spectrum of the used laser, which is important since laser noise can lead to heating in the trap. In Chapter 4 we then show how we transfer atoms into this new trap and characterize it using various measurements. The characterization includes the trap frequencies, the lifetime of the atoms in the trap, the trap depth and the positional stability of the trap. Finally, Chapter 5 summarizes the most important results of this thesis and gives a short outlook on what we hope to achieve in the future.

2. Theory of Ultracold Atoms and Optical Trapping

This chapter provides a summary of the physics of ultracold Fermi gases and their interactions with an emphasis on ${}^6\text{Li}$ since we use it in our experiments. In addition, the optical trapping technique needed to investigate such systems is explained.

At first in Section 2.1 the basic properties of an ideal Fermi gas are shortly summarized. Then in Section 2.2 the concept of universality in ultracold scattering is introduced and a derivation for the scattering length is given. Subsequently in Section 2.3, the concept of a magnetic Feshbach resonance is introduced which allows one to tune the scattering length. After that, the most important properties of ${}^6\text{Li}$ are summarized in Section 2.4.

Finally in Section 2.5, the technique of optical trapping is introduced and the basic formulas are derived, following the deduction given in [Gri00].

2.1. Ideal Fermi Gas

In quantum mechanics, the position and momentum of each particle is described by a wave function corresponding to a probability density. Thus there is a position uncertainty Δx for the particle which is given by the width of the wave function and is on the order of the de-Broglie wavelength λ_{dB} . This position uncertainty is coupled to the momentum uncertainty Δp via the Heisenberg uncertainty principle as $\Delta x \cdot \Delta p \geq \hbar/2$ and thus Δx behaves inversely to Δp . In a thermal cloud the momentum uncertainty can be interpreted as the width of the Maxwell-Boltzmann distribution which becomes narrower with decreasing temperature. Thus when cooling down a cloud of atoms, the width of the wave function of each particle gets larger until at a certain temperature threshold the width of each individual wave function which is on the order of λ_{dB} gets comparable to the inter-particle spacing $d \sim n^{-\frac{1}{3}}$ at a given density n . Then the wave functions of the individual particles start to overlap and the atoms become indistinguishable. This leads to a breakdown of the classical description of a thermal cloud and one enters the quantum degenerate regime. In this regime, there is a fundamental difference between the statistics of fermions and bosons. Whereas bosons obey Bose-Einstein statistics and tend to accumulate in the ground state as $T \rightarrow 0$ [Ein25], fermions are forbidden to occupy the same quantum state due to the Pauli exclusion principle and obey Fermi-Dirac statistics described by an occupation probability¹

$$f(E, \mu, T) = \frac{1}{e^{(E-\mu)/k_B T} + 1} \quad (2.1)$$

¹Here in its grand canonical formulation.

for each quantum state which depends on the energy E , the chemical potential μ and the temperature T of the system. For $T = 0$ this results in a step function where each level is occupied by a single fermion up to the Fermi energy $E_F \equiv \mu(T = 0)$ and higher levels are not occupied. Thus the Fermi energy is the natural energy scale for the system and one usually compares the energy, temperature and momentum of a given system to its Fermi energy E_F , the Fermi temperature $T_F = E_F/k_B$ and the Fermi wave vector $k_F = \sqrt{2mE_F/\hbar^2}$.

In a harmonic trap with a trapping potential

$$V(x, y, z) = \frac{1}{2}m(\omega_x^2 x^2 + \omega_y^2 y^2 + \omega_z^2 z^2), \quad (2.2)$$

the Fermi energy is given by [Gio08]

$$E_F = (6N)^{1/3} \hbar\bar{\omega} \quad (2.3)$$

where N is the atom number and $\bar{\omega} = (\omega_x\omega_y\omega_z)^{1/3}$ is the mean trapping frequency.

At zero temperature, the spatial and momentum distribution is given by [Gio08]

$$n(\mathbf{r}, T = 0) = \frac{8N}{\pi^2 x_F y_F z_F} \left(1 - \frac{x^2}{x_F^2} - \frac{y^2}{y_F^2} - \frac{z^2}{z_F^2}\right)^{3/2} \quad (2.4)$$

$$n(\mathbf{p}, T = 0) = \frac{8N}{\pi^2 p_F^3} \left(1 - \frac{p^2}{p_F^2}\right)^{3/2} \quad (2.5)$$

where the Fermi radii i_F are defined as $E_F = 0.5m\omega_i^2 i_F^2$ and $p_F = \hbar k_F$ is the Fermi momentum. Thus the spatial density profile of an ideal Fermi gas at zero temperature has a rather flat top compared to the Gaussian profile of a thermal cloud. This characteristic difference is used to detect the onset of quantum degeneracy when cooling a Fermi gas. While the spatial density profile is affected by anisotropies in the trapping potential, the momentum distribution remains isotropic. Thus any anisotropies in the expansion after releasing the Fermi gas from the trap can be attributed to interaction effects and are a signature of hydrodynamic behavior [O'H02, Tre11].

2.2. Ultracold Scattering

To obtain detailed structural information in physics requires to perform scattering experiments at high energies and thus small de-Broglie wavelengths λ_{dB} . Then the scattered particles resolve the exact shape of the interaction potential and detailed information of the potential can be gained. This is displayed for example in the improved resolution of an electron microscope compared to a light microscope. Reversing this argument, if one wants to access a regime where the exact shape of the short range interaction potential does not influence the scattering process, one has to go to very small energies where the de-Broglie wavelength λ_{dB} is much larger than the finite range of the interaction r_0 . Then the microscopic details of the short-range interaction are no longer resolved and the long-range effects of the scattering can

be described by a few effective parameters. All quantities which depend in turn on these parameters are called universal since they are unaffected by the exact details of the short-range physics.

In typical experiments with ultracold atoms we deal with the situation that we have a very dilute gas with densities on the order of 10^{12} - 10^{15} cm^{-3} because at lower densities elastic collision rates would be too small for efficient cooling and at higher densities three body losses would dominate [Ket08]. Thus to be in the quantum degenerate regime one needs large de-Broglie wavelengths λ_{dB} on the order of $1 \mu\text{m}$ which is typically achieved at temperatures between 100 nK and $50 \mu\text{K}$. The interaction between neutral atoms is mediated via the short-ranged van-der-Waals potential with a finite range $r_0 = r_{\text{vdW}}$. Since it scales as r^{-6} , the range of the potential is usually limited to values below $5 \text{ nm} \sim 100 a_0$, where a_0 is the Bohr radius. Therefore the condition $\lambda_{\text{dB}} \gg r_{\text{vdW}}$ is met very well and the scattering can be almost perfectly described by a single parameter, the s-wave scattering length a . This simplicity makes these system an ideal playground to test fundamental theories with high precision. Another advantage of these ultracold systems is their diluteness: as the inter-particle distance $n^{-1/3}$ is usual several orders of magnitude larger than the range of the interaction, this means that the atoms only interact via two-body collisions which are fully described by the scattering length a . Thus also many-body quantities like the mean energy only depend on a and are thus universal.

If furthermore the condition $a \gg r_{\text{vdW}}$ is met, then also the most shallow bound state of two scattering atoms does not depend on the exact potential anymore but its binding energy is solely determined by the scattering length a as

$$E_B = \frac{\hbar^2}{ma^2}. \quad (2.6)$$

The universality allows to approximate the scattering between two particles almost perfectly as a point-like contact interaction which can be described by an effective δ -function potential $V_{\text{cp}} = g\delta(r)$ where the coupling strength is given by $g = \frac{4\pi\hbar^2}{m}a$ [Dal99]. Due to this simple description of the interaction, the Hamiltonians are well known for these systems and thus they are ideal quantum simulators to test fundamental theories in a controlled manner. In addition, the existence of magnetic Feshbach resonances allow to tune the scattering length to arbitrary values by applying a homogeneous offset field and thus one can access different interaction regime with the same apparatus, making ultracold systems a very powerful tool to investigate theoretical models.

The s-wave scattering length

The derivation of the scattering length can be found in many textbooks e.g. [Sak11, Bra03]. In the following, the important steps of the derivation are summarized and the results are given.

Elastic scattering of two non-identical particles at low-energies can be described in a non-relativistic framework by solving the time-independent Schrödinger equation

$$\left[-\frac{\hbar^2}{2m_r} \nabla^2 + V(\mathbf{r}) \right] \psi(\mathbf{r}) = E\psi(\mathbf{r}), \quad (2.7)$$

where \mathbf{r} is the relative position and $m_r = m/2$ is the reduced mass of the particles. If one assumes a spherically symmetric potential $V(r)$ with a potential drop-off faster than $1/r$, then the wave function $\psi(\mathbf{r})$ satisfies the free-particle Schrödinger solution in the long-distance limit $r \rightarrow \infty$ and can be written as the sum of an incoming plane wave ψ_{inc} and an outgoing spherical wave ψ_{sc} :

$$\psi(\mathbf{r}) \xrightarrow{r \rightarrow \infty} \psi_{\text{inc}}(\mathbf{r}) + \psi_{\text{sc}}(\mathbf{r}) \sim \exp(ikz) + f(k, \theta) \frac{\exp(ikr)}{r}. \quad (2.8)$$

Here the incoming particles are considered to have energy $E_k = \frac{\hbar^2 k^2}{2m_r}$ with momentum k along the z -axis and the scattering amplitude $f(k, \theta)$ is independent of the azimuthal angle ϕ due to the symmetry of the system. In the experiment, the long-distance limit is satisfied when the relative distance $|\mathbf{r}|$ is much larger than the range of the van der Waals potential, $r \gg r_{\text{vdW}}$, which is very well met in ultracold atom experiments. From the scattering amplitude one can then immediately calculate the differential cross-section to be

$$\frac{d\sigma}{d\Omega} = |f(k, \theta)|^2. \quad (2.9)$$

As an ansatz to derive the scattering amplitude, one expands the wave function into a series of Legendre polynomials

$$\psi(k, r, \theta) = \sum_{l=0}^{\infty} R_l(k, r) P_l(\cos \theta). \quad (2.10)$$

Putting this ansatz into the Schrödinger equation (2.7) then separates it into a radial part and a spherical part. In the long-distance limit $r \rightarrow \infty$, the radial solutions for R_l are identical with the free-particle solutions apart from phase shifts $\delta_l(k)$ which display the effect of the short-ranged interaction

$$R_l(k, r) \xrightarrow{r \rightarrow \infty} \frac{A_l(k)}{kr} \sin \left[kr - \frac{\pi}{2}l + \delta_l(k) \right]. \quad (2.11)$$

In Figure 2.1 this phase shift for each partial wave ψ_l is displayed exemplary for the case of ψ_0 . To obtain an expression for the scattering amplitude, one has to expand the plane and spherical waves in equation (2.8) in a series of Legendre polynomials as well and compare the coefficients with the ones obtained by putting equation (2.11) into equation (2.10). This yields the following expression for the scattering amplitude

$$f(k, \theta) = \frac{1}{2ik} \sum_{l=0}^{\infty} (2l+1) \left(e^{2i\delta_l(k)} - 1 \right) P_l(\cos \theta) = \sum_{l=0}^{\infty} f_l(k, \theta) P_l(\cos \theta). \quad (2.12)$$

By integrating the differential cross-section over the full solid angle, one obtains the total cross-section

$$\sigma(k) = \sum_{l=0}^{\infty} \sigma_l(k) = \frac{4\pi}{k^2} \sum_{l=0}^{\infty} (2l+1) \sin^2 \delta_l(k). \quad (2.13)$$

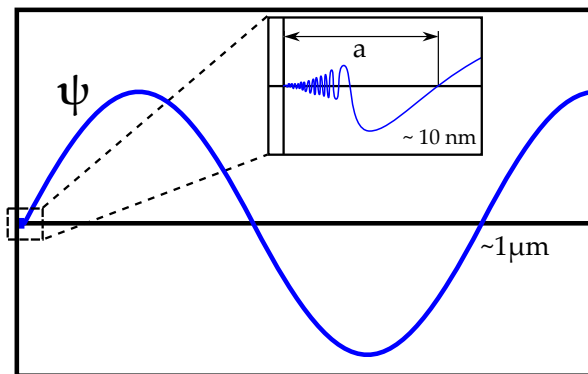


Figure 2.1.: **Illustration of the interaction induced phase shift of the wave function.** At low energies, the wave function at distances $r \gg r_{\text{vdW}}$ is the free-particle solution which is shifted by a phase δ_0 . The inset shows the short-range effect of the interaction on the wave function. The scattering length a can then be understood as the distance by which the free-particle solution is shifted with respect to the non-interacting case. The picture is adapted from [Wei09].

For small momentum $k \ll 1/r_{\text{vdW}}$ and therefore low scattering energies, the phase shifts scale as $\tan \delta_l \propto k^{2l+1}$ due to the centrifugal barrier². Thus in the ultracold regime, scattering processes with $l > 0$ are strongly suppressed and the interaction can be described by only considering the $l = 0$ (s-wave) term. Since the zeroth order Legendre polynomial P_0 is independent of the angle θ , s-wave scattering is isotropic which simplifies the interactions in ultracold systems a lot and makes it possible to account for the effect of the interactions by a single parameter.

This universal parameter is the scattering length a which is defined as³

$$a = - \lim_{k \cdot r_{\text{vdW}} \ll 1} \frac{\tan \delta_0}{k}. \quad (2.14)$$

As can be seen in Figure 2.1, the scattering length can be interpreted as the distance the free-particle solution of the Schrödinger equation is pushed out of the center. The strength of the interaction is given by the amplitude of a and is for alkali atoms usually on the order of 10 to $100a_0$, where a_0 is the Bohr radius. Since the range r_{vdW} of the interaction is much smaller than the de-Broglie wavelength λ_{dB} , the details of the potential are not probed by the interaction and thus for calculations one can assume a point-like contact potential $V_{\text{cp}} = g\delta(r)$ where the coupling strength is given by $g = \frac{4\pi\hbar^2}{m}a$ [Dal99]. Hence, although the van-der-Waals interaction is always attractive on the microscopic scale, the overall effect in the long-distance limit can be either attractive or repulsive depending on the sign of the scattering length.

²In ${}^6\text{Li}$, the centrifugal barrier is $\simeq k_B \cdot 10 \text{ mK}$ [Geh03].

³The truncation of the expansion $k \cot \delta_0(k) = -\frac{1}{a} + \frac{1}{2}r_{\text{eff}}k^2 + \mathcal{O}(k^4)$ is correct if k is much smaller than the effective range r_{eff} of the potential where r_{eff} is identical with r_{vdW} up to a numerical factor on the order of 1.

From the scattering length one can then calculate the total cross-section of the s-wave scattering for distinguishable particles as

$$\sigma_{\text{dist}} = \frac{4\pi a^2}{1 + k^2 a^2}. \quad (2.15)$$

In the limit of weak interactions, $ka \ll 1$ holds and thus the total cross-section becomes energy independent with

$$\sigma_{\text{dist}} = 4\pi a^2. \quad (2.16)$$

For resonantly enhanced interactions it is however also possible to reach the regime where $ka \gg 1$. Then the total cross-section does not depend on the scattering length anymore but becomes energy dependent with

$$\sigma_{\text{dist}} = \frac{4\pi}{k^2}. \quad (2.17)$$

This is also called the unitarity regime as the physics of the system can then be described solely by the natural energy scale E_F of the system⁴. Since for ultracold

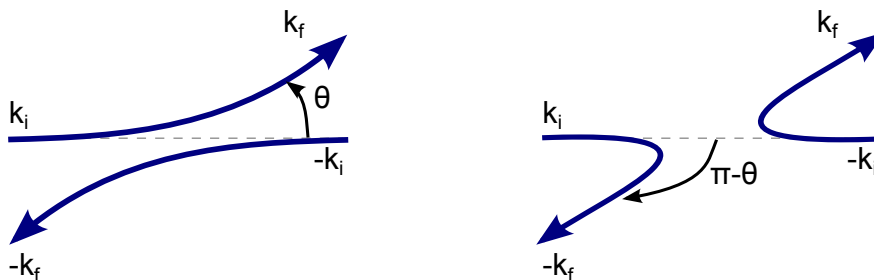


Figure 2.2.: **Illustration of identical scattering.** For indistinguishable particles the two scattering processes are equivalent and thus the wave function has to be symmetrized (anti-symmetrized) in the bosonic (fermionic) case. The picture is adapted from [Dal99].

gases the atoms become indistinguishable, one is not able to differentiate anymore between the two scattering processes depicted in Figure 2.2. Then the wave function has to be symmetrized (anti-symmetrized) in the bosonic (fermionic) case which leads to a differential cross-section

$$\frac{d\sigma}{d\Omega} = |f(k, \theta) \pm f(k, \pi - \theta)|^2, \quad (2.18)$$

where the plus sign indicates the bosonic case and the minus sign the fermionic case. Since the scattering amplitude is angle independent in s-wave scattering, the scattering of identical bosons is enhanced as $\sigma_{\text{boson}} = 4\sigma_{\text{dist}}$ while the scattering of identical fermions completely vanishes with $\sigma_{\text{fermion}} = 0$. Therefore to have interactions in ultracold Fermi gases, one either needs an additional atomic species or has to use distinguishable internal states of the same atomic species.

⁴The attractive Bose gas is only stable on the repulsive side. There the Bose gas fermionizes as the interaction increases and in the limit of $a \rightarrow \infty$ can be mapped onto a non-interacting Fermi gas.

Mean field interaction

If we want to calculate the interaction energy in a many-body system of N distinguishable atoms, we can use a mean field approach to approximate the effect. Assuming a dilute gas and using the point-like contact potential, the mean field interaction can be calculated as⁵

$$U_{\text{mf}} = \lim_{V \rightarrow 0} \frac{1}{V} \sum_{i=1}^N \int_V d\mathbf{r} g \delta(\mathbf{r} - \mathbf{r}_i) = \frac{4\pi\hbar^2}{m} a n, \quad (2.19)$$

where V is the enclosed volume, \mathbf{r}_i is the position of the distinguishable atoms and $n = \frac{N}{V}$ is the density of the cloud as depicted in Figure 2.3. Thus the interparticle

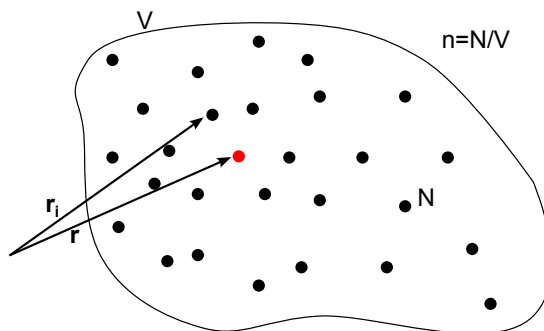


Figure 2.3.: **Illustration of the mean field interaction.** The red particle experiences an effect of the mean field mediated by the neighboring particles. The picture is adapted from [Joc04].

interactions are attractive for $a < 0$ and repulsive for $a > 0$ on a macroscopic scale, although the van der Waals interaction is always attractive on the microscopic scale.

2.3. Feshbach Resonances

Scattering of two particles can be understood in the terms of scattering channels. Each scattering channel depends on the spin configuration of the colliding particles and thus has a different interaction potential and continuum energy. Depending on the incident energy of the particles, the channels can then be separated into so-called open channels which are energetically allowed, and closed channels which are energetically forbidden in the long-distance limit. This is depicted in Figure 2.4 (a) where the incident energy is not large enough to reach the continuum of the closed red channel.

When considering only scattering in the open channel, the scattering length is fixed and depends on the atomic species. The scattering length is very sensitive if there is a bound state closely below (above) the continuum. The scattering is then resonantly enhanced and the scattering length becomes large and positive (large and negative) [Lan81]. Thus to have a large scattering length, one has to use an atomic species where there is a bound state close to the continuum. However, if one

⁵For indistinguishable, non-condensed particles one has to take also into account the exchange symmetry which leads to a multiplicative factor of two for the mean field interaction [Gri96].

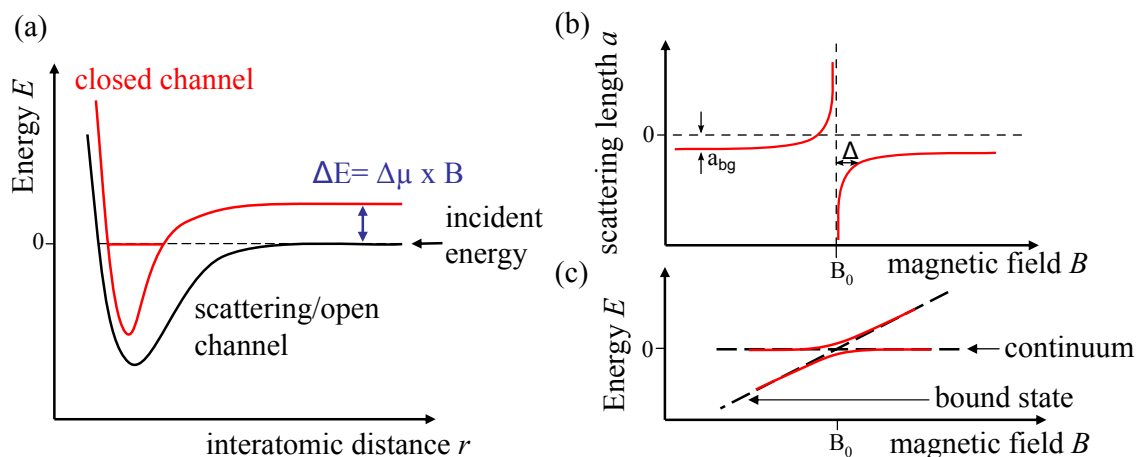


Figure 2.4.: **Basic concept of a magnetic Feshbach resonance.** The resonance occurs when the energy difference between a bound state of a closed channel (red) and the incident energy in the scattering/open channel (black) is tuned to zero via an applied magnetic offset field (a). The scattering length is then resonantly enhanced, leading to a divergence $a \rightarrow \infty$ at the resonance position B_0 (b). When tuning the interaction across the resonance, there is an avoided crossing between the open and closed channel which adiabatically connects the molecular bound state to the continuum (c). The picture is adapted from [Wen08].

considers also an additional closed channel and there is a coupling between the open channel and a bound state in this closed channel, the particles can undergo a second-order process, entering the bound state in the closed channel before coupling back to the open channel. If there is a difference $\Delta\mu$ in the magnetic moment between the channels, one can tune the bound state energy to be close to the continuum of the open channel by applying a homogeneous magnetic field (see Figure 2.4 (a)). As in the resonantly enhanced case, this leads to a divergence of the scattering length a at the resonance position B_0 where the bound state is exactly at the zero energy threshold and thus one can tune the interaction to arbitrary values⁶ (see Figure 2.4 (b)).

Such a resonant enhancement of the scattering due to a coupling of two channels is called a Feshbach resonance⁷. The arbitrary tuning of the scattering length and thus the interaction strength around a Feshbach resonance makes ultracold systems a perfect playground to study theoretical models because it allows one to enter different interaction regimes with the same experimental apparatus.

The effect of the Feshbach resonance on the scattering length is depicted in Figure 2.4 (b) and can be calculated as [Moe95]

$$a(B) = a_{\text{bg}} \left(1 - \frac{\Delta}{B - B_0} \right), \quad (2.20)$$

where a_{bg} is the background scattering length of the open channel, B_0 is the reso-

⁶Depending on the magnetic field stability in the experiment and the width of the resonance.

⁷H. Feshbach investigated this first in his studies on nuclear reactions [Fes58].

nance position and Δ is the width of the resonance, which depends on the coupling strength g of the channels and the magnetic moment difference $\Delta\mu$. Thus by tuning across the resonance, one can go from a repulsively to an attractively interacting gas and vice versa.

The coupling dresses the energy of the particles and new ground states are formed as superpositions of the continuum of the open channel and the bound state of the closed channel as depicted in Figure 2.4 (c). This leads to an avoided crossing at the resonance and one can adiabatically go from a molecular bound state to the free-atom continuum when tuning the magnetic field slowly across the resonance.

More information on Feshbach resonances can also be found in [Chi10].

The BEC-BCS crossover

The transition from a molecular bound state to the free-atom continuum is known as the BEC-BCS crossover and has been extensively studied [Bar04b, Kin04, Bar04a, Chi04, Par05, Kin05, Zwi05].

The transition can be understood as a smooth process which connects two different regimes (see Figure 2.5). On the repulsive side of the resonance, the ground state consists of tightly bound molecules. Therefore below a critical temperature T_c , the molecules can condense into a Bose-Einstein condensate, which is why this side of the Feshbach resonance is also called the BEC side. On the attractive side of the resonance, the ground state consists of free atoms. For weak attraction, the atoms can form pairs in momentum space - so-called Cooper pairs - which then can become superfluid below a critical temperature given by BCS theory [Bar57]. Therefore that side of the Feshbach resonance is also known as the BCS side. On resonance, one enters the unitarity regime where the size of the pairs becomes comparable to the interparticle distance. Then the scattering length is not a meaningful quantity anymore and all physics becomes universal, being only characterized by the natural energy scale E_F of the system.

Molecule Formation

To form molecules, one can tune the interaction close to the resonance on the BEC side where the binding energy of the weak molecular state can be calculated as [Pet04]

$$E_B = \frac{\hbar^2}{ma^2}. \quad (2.21)$$

Three-body recombination, where the excess momentum is transferred to a third particle, then leads to a population of these weakly bound molecules, whose size is on the order of the scattering length a .

This equation only holds as long as the dimer size is much larger than the effective range

$$r_{\text{eff}} = \left(\frac{mC_6}{\hbar^2} \right)^{1/4} \quad (2.22)$$

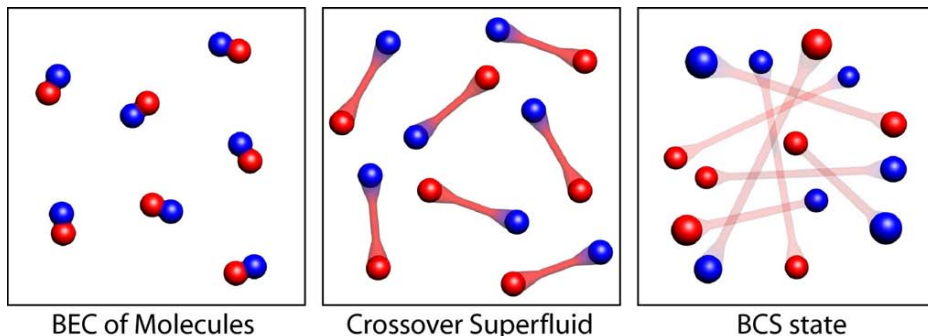


Figure 2.5.: **Illustration of the BEC-BCS crossover.** Tuning the interaction strength via a Feshbach resonance, one can go smoothly from the BEC-limit of tightly bound molecules to the BCS-limit of long-ranged Cooper pairs, where the size of the pairs is much larger than the inter-particle spacing. On resonance, one enters the unitarity regime where the pair size is on the same order as the inter-particle spacing. The picture is taken from [Ket08].

of the potential. It can be extended to lower values of a however by subtracting a so-called mean scattering length \bar{a} from a which leads to [Gri93]

$$E_B = \frac{\hbar^2}{m(a - \bar{a})^2}. \quad (2.23)$$

For ${}^6\text{Li}$ this correction can be calculated to be [Gri93, Joc04]

$$\bar{a} = \frac{\Gamma(3/4)}{2\sqrt{2}\Gamma(5/4)} r_{\text{eff}} \approx 0.478 r_{\text{eff}} \approx 29.9 a_0. \quad (2.24)$$

This weakly bound state is of course not the vibrational ground state of the system and thus the molecules can relax into deeper states, releasing a lot of binding energy in the process. This leads ultimately to loss of atoms in the trap because the kinetic energy acquired exceeds the trapping potential.

In a two-component Fermi gas however, these relaxation processes are highly suppressed due to Pauli blocking since atom-dimer or dimer-dimer collisions always involve at least two identical particles. The scattering properties of these collisions were calculated in a series of papers by D. Petrov et al. [Pet03, Pet04, Pet05]. They found that the scattering length of these atom-dimer or dimer-dimer collisions are directly related to the atom-atom scattering length a via

$$a_{ad} = 0.6a, \quad (2.25)$$

$$a_{dd} = 1.2a, \quad (2.26)$$

and that the relaxation rate constant α_{rel} scales as

$$\alpha_{\text{rel}} = \begin{cases} a^{-3.33} & \text{atom-dimer} \\ a^{-2.55} & \text{dimer-dimer} \end{cases} \quad (2.27)$$

with the atom-atom scattering length. Therefore both relaxation processes are strongly suppressed close to the resonance, making the gas more stable. This is not the case in bosonic gases where one has strong losses close to the resonance. Thus in a Fermi gas one can prepare long-lived molecules which can then be cooled down into a molecular BEC [Joc03, Zwi03, Gre03].

2.4. Properties of Lithium

In our experiment we use ${}^6\text{Li}$ and thus this section gives a brief summary about the important properties of ${}^6\text{Li}$. The information given here can be found in [Geh03, Chi10].

Level structure

Lithium is an alkali atom and hence only has one valence electron with a total electron spin $S = 1/2$. The fermionic isotope ${}^6\text{Li}$ has a nuclear spin of $I = 1$. At zero magnetic field, the total orbital angular momentum $\mathbf{J} = \mathbf{L} + \mathbf{S}$ couples to the nuclear spin, making the total angular momentum $\mathbf{F} = \mathbf{J} + \mathbf{I}$ a good quantum number and leads e.g. for the ground state to a hyperfine splitting into $F = 1/2$ and $F = 3/2$. The level scheme including the hyperfine interaction can be seen in Figure

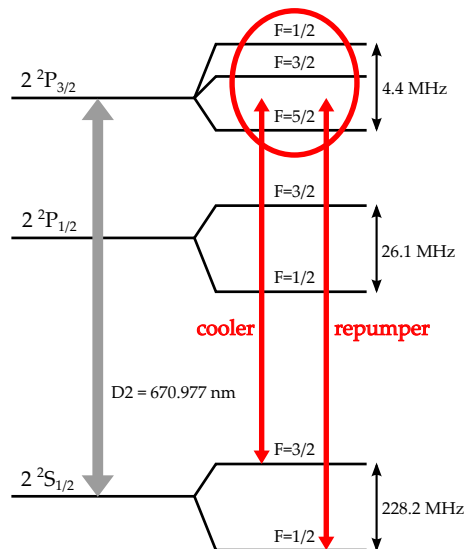


Figure 2.6.: **Level scheme of ${}^6\text{Li}$.** The hyperfine structure of the excited state of the D2-line is not resolved since the splitting is smaller than the natural linewidth Γ of the transition. A closed cycle between the ground and excited state - used for cooling and trapping - can be achieved using the transitions labeled as cooler and repumper. The picture is taken from [Boh12].

2.6. In our experiment we use the ground state $2^2S_{1/2}$ and the excited state $2^2P_{3/2}$ for cooling and trapping. The electronic transition between these states is called the D2-transition and has a wavelength of 670.977 nm, thus being in the visible regime. The

ground state splits into the hyperfine states $|2^2S_{1/2}, F = 1/2\rangle$ and $|2^2S_{1/2}, F = 3/2\rangle$ with a separation of 228.2 MHz. The excited state splits into three sub-states which are separated by 4.4 MHz. Because the separation of the excited state is smaller than the natural linewidth $\Gamma = 5.9$ MHz of the D2-transition, the hyperfine structure is not resolved and the atoms can relax from the excited states into both ground states.

Thus one needs two laser frequencies separated by 228.2 MHz - called cooler and repumper - to create a closed cycle between the ground state and the excited state. These transitions are then used to laser cool the atoms and trap them in the magneto-optical trap (MOT) as explained in Section 3.1.3.

At zero magnetic field, the hyperfine states are degenerate in their magnetic sub-levels $m_F = -F, \dots, F$. When applying a magnetic field however, the degeneracy is removed as can be seen in Figure 2.7 for the ground state. For magnetic fields above $B \approx 30$ G, the electron spin S^8 and the nuclear spin I decouple and thus F is not a good quantum number anymore. The states then have to be described by the set of quantum numbers $|S = 1/2, I = 1, m_S, m_I\rangle$ and one can see that the states separate into two groups: the high-field seeking states $|1\rangle$ - $|3\rangle$ with $|m_S = -1/2, m_I = 0, \pm 1\rangle$, which minimize their internal energy at high magnetic fields, and the low-field seeking states $|4\rangle$ - $|6\rangle$ with $|m_S = +1/2, m_I = 0, \pm 1\rangle$ which minimize their internal energy at low magnetic fields. Since the coupling of the electron spin to the magnetic field is much larger than the coupling of the nuclear spin, the behavior at high magnetic fields almost entirely depends on the orientation of the electron spin and thus the states with identical m_S tune approximately parallel in respect to the magnetic field. In the experiment, one operates usually at high magnetic fields $B > 100$ G and thus

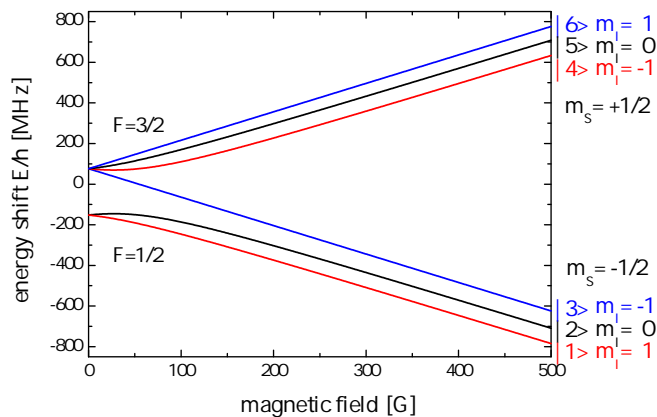


Figure 2.7.: **Energy splitting of the ground state $2^2S_{1/2}$ in ^6Li .** At high magnetic fields the electron spin S and the nuclear spin I decouple and the states separate into the high-field seeking states $|1\rangle$ - $|3\rangle$ and the low-field seeking states $|4\rangle$ - $|6\rangle$. We use the high-field seeking states in our experiment since any binary mixture of these is stable if the magnetic field is not close to zero.

one is deeply in the decoupled regime. Since binary mixtures of the low-field seeking

⁸For the ground state $L = 0$ and thus $J = S$.

states $|4\rangle$ - $|6\rangle$ can decay into the states $|1\rangle$ - $|3\rangle$ via spin-changing collisions, we use the high-field seeking states for our experiments. These are stable on the lifetimes of our experiments and one can use radio-frequency (rf) pulses to drive transitions between them (see Section 4.5.1).

Feshbach Resonances

When using the three lowest hyperfine states of ${}^6\text{Li}$, there are three different scattering channels depending on the states of the colliding particles. This leads to different scattering lengths a_{12}, a_{13}, a_{23} which tune slightly different with respect to an external magnetic field. As can be seen in Figure 2.8, each channel supports a broad Feshbach resonance below 1000 G which is experimentally accessible. The graphs have been calculated using a coupled channel method where the position of the $|1\rangle$ - $|2\rangle$ resonance has been determined in our group using precise rf-spectroscopy of weakly bound molecules [Zür13]. The results of these calculations are summarized in Table 2.1. For the $|1\rangle$ - $|2\rangle$ channel, there is also an additional resonance at about 543 G which is very narrow and thus not often used in our experiments. The background scattering length is very sensible whether the atoms collide in a

Scattering channel	B_0 [G]	Δ [G]	a_{bg} [a_0]
$ 1\rangle$ $ 2\rangle$	832.18	-262.3	-1582
$ 1\rangle$ $ 3\rangle$	689.68	-116.6	-1770
$ 2\rangle$ $ 3\rangle$	809.76	-200.3	-1642

Table 2.1.: **Position B_0 , width Δ and background scattering length a_{bg} of the Feshbach resonances for the states $|1\rangle$, $|2\rangle$ and $|3\rangle$.** The values are obtained from calculations as explained in [Zür13]. The background scattering length is valid above the resonance. Note that the position of the zero-crossings in Figure 2.8 is not given by the simple equation (2.20) as this equation only holds close to the resonance.

singlet or triplet configuration of their respective electron spins. In ${}^6\text{Li}$, the triplet scattering length is enhanced because there is a virtual bound state slightly above the continuum⁹. Therefore the triplet scattering length a_t is large and negative with values of about $a_t \sim -2000 a_0$. The singlet scattering length a_s on the other hand has no bound state close to the continuum and thus is only on the order of $a_s \sim 40 a_0$. At low magnetic fields, the scattering states are in a superposition of singlet and triplet states and thus their scattering length is small. As one goes to higher magnetic fields, the contribution of the triplet state becomes stronger. This explains the local minima of the scattering lengths a_{ij} below the resonance. At high magnetic fields above the resonance, the scattering potentials are almost completely governed by the electronic $m_S = -1/2$ state of the two colliding atoms and thus the scattering state is almost a pure triplet. Therefore one obtains large negative background scattering lengths a_{bg} for ${}^6\text{Li}$ above the resonance.

⁹A change of less than 10^{-3} of the potential depth would already cause the triplet scattering length to change its sign [Joc04].

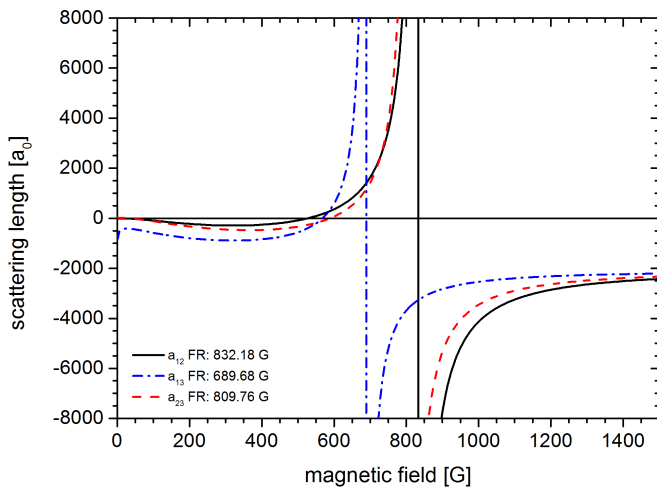


Figure 2.8.: **S-wave scattering length a in units of the Bohr radius a_0 of ${}^6\text{Li}$ for all combinations of the three lowest hyperfine states.** All combinations a_{ij} have a broad Feshbach resonance below $B = 1000$ G. The position of the $|1\rangle - |2\rangle$ resonance was determined in our group using precise rf-spectroscopy of weakly bound molecules [Zür13]. The scattering lengths a_{ij} were then determined using a coupled-channel calculation.

2.5. Optical Trapping

Cooling atoms down into the ultracold regime where the interaction is universal and tunable via magnetic Feshbach resonances requires a trapping mechanism which fulfills the following conditions: it must not depend on magnetic fields since one needs a magnetic offset field as a free parameter to control the interaction. Furthermore, the heating introduced by the trapping has to be sufficiently low to not severely limit the achievable temperature.

Far off-resonant optical dipole traps fulfill both these requirements. They rely on the electric dipole interactions between the strong electric field of a laser beam and the induced dipole moment in the neutral atoms. Compared to other trapping methods like e.g. magnetic traps, this mechanism is quite weak and thus one has to pre-cool the atoms before applying optical trapping.

To calculate the main properties of optical traps, we use a classical oscillator model as derived in [Gri00]. This assumption provides a very good approximation for atoms with a strong dipole allowed transition and when one can neglect any saturation effects. In our case of ${}^6\text{Li}$ as an alkali atom with a single valence electron, this approach is valid since we are operating far away from resonance.

Although neutral atoms have no permanent dipole moment, the electric field \mathbf{E} of the laser induces a dipole moment \mathbf{p} oscillating at the driving frequency ω . The

usual complex notation for this is

$$\mathbf{E}(\mathbf{r}, t) = \hat{\mathbf{e}} \tilde{E}(\mathbf{r}) \exp(-i\omega t) + c.c. \quad (2.28)$$

$$\mathbf{p}(\mathbf{r}, t) = \hat{\mathbf{e}} \tilde{p}(\mathbf{r}) \exp(-i\omega t) + c.c., \quad (2.29)$$

where $\hat{\mathbf{e}}$ is the unit polarization vector. The amplitude \tilde{p} of the dipole moment is connected to the electric field amplitude \tilde{E} by

$$\tilde{p} = \alpha(\omega) \tilde{E}, \quad (2.30)$$

where α is the complex polarizability which depends on the driving frequency ω .

The interaction potential of the induced dipole moment \mathbf{p} in the driving field \mathbf{E} is then given by

$$U_{\text{dip}} = -\frac{1}{2} \langle \mathbf{p} \mathbf{E} \rangle = -\Re(\alpha) |\tilde{E}(\mathbf{r})|^2 = -\frac{1}{2\epsilon_0 c} \Re(\alpha) I(\mathbf{r}), \quad (2.31)$$

where $\langle \rangle$ denotes a time average over the rapid oscillations¹⁰ and $I(\mathbf{r}) = 2\epsilon_0 c |\tilde{E}(\mathbf{r})|^2$ is the spatially dependent laser intensity. The factor 1/2 takes into account that the dipole moment is only induced and not permanent. Thus the dipole potential is directly related to the real part $\Re(\alpha)$ of the polarizability which describes the in-phase component of the oscillation. It is also called the dispersive part since it determines the phase shift the electric field experiences.

The dipole force acting on the atom

$$\mathbf{F}_{\text{dip}}(\mathbf{r}) = -\nabla U_{\text{dip}} = \frac{1}{2\epsilon_0 c} \Re(\alpha) \nabla I(\mathbf{r}) \quad (2.32)$$

is thus proportional to the intensity gradient of the laser and is a conservative force.

Apart from feeling the dipole force, the oscillator also absorbs a power P_{abs} from the driving field. In a quantum mechanical picture, this can be interpreted as the absorption and subsequent re-emission of photons with energy $\hbar\omega$ at a scattering rate Γ_{sc} which is given by

$$\Gamma_{\text{sc}} = \frac{P_{\text{abs}}}{\hbar\omega} = \frac{\langle \dot{\mathbf{p}} \mathbf{E} \rangle}{\hbar\omega} = \frac{1}{\hbar\epsilon_0 c} \Im(\alpha) I(\mathbf{r}). \quad (2.33)$$

Thus the scattering rate Γ_{sc} is directly connected to the imaginary part $\Im(\alpha)$ of the polarizability which describes the out-of-phase component of the oscillation and is related to absorption and subsequent re-emission of a photon. This leads to heating in the trapped atomic cloud and thus sets a limit to the achievable temperature. At very low trap depths this can also lead to a loss of atoms and thus a decreasing lifetime. Therefore one wants to operate in a regime where the dipole potential is still large enough for trapping but the scattering rate is already negligible.

To calculate the polarizability α we start by considering the atom in Lorentz's model of a classical oscillator. In this simple model the valence electron (mass m_e , elementary charge e) is bound elastically to the atomic core with an eigenfrequency

¹⁰The averaging eliminates all terms with a factor $e^{\pm 2i\omega t}$.

ω_0 which corresponds to the optical transition frequency. The movement of the electron can then be described by the equation of motion for a damped, driven oscillator

$$\ddot{x} + \Gamma_\omega \dot{x} + \omega_0^2 x = -\frac{eE(t)}{m_e}, \quad (2.34)$$

where Γ_ω is a damping term due to the dipole radiation of the accelerated electron and can be calculated by Larmor's formula [Jac75]

$$\Gamma_\omega = \frac{e^2 \omega^2}{6\pi \epsilon_0 m_e c^3}. \quad (2.35)$$

Solving this equation and considering that the dipole moment is just given by the displacement of the charge $\mathbf{p} = e\mathbf{x}$, this yields for the polarizability

$$\alpha(\omega) = 6\pi \epsilon_0 c^3 \frac{\Gamma}{\omega_0^2 \omega_0^2 - \omega^2 - i(\omega^3/\omega_0^2)\Gamma}, \quad (2.36)$$

where we have introduced the on-resonance damping rate $\Gamma \equiv \Gamma_{\omega_0} = (\omega_0/\omega)^2 \Gamma_\omega$. Note that in a semiclassical approach with a two-level system, the damping rate corresponds to the spontaneous decay rate of the excited state and is related to the dipole matrix element between ground and excited state. However, for alkali atoms the results obtained with the classical approximation are correct within a few percent.

Using the derived expression for the polarizability and putting it into equations (2.31) and (2.33), we obtain explicit expressions for the dipole potential U_{dip} and scattering rate Γ_{sc}

$$U_{\text{dip}}(\mathbf{r}) = \frac{3\pi c^2}{2\omega_0^3} \left(\frac{\Gamma}{\Delta} + \frac{\Gamma}{\Delta + 2\omega_0} \right) I(\mathbf{r}), \quad (2.37)$$

$$\Gamma_{\text{sc}}(\mathbf{r}) = \frac{3\pi c^2}{2\hbar\omega_0^3} \left(\frac{\omega}{\omega_0} \right)^3 \left(\frac{\Gamma}{\Delta} + \frac{\Gamma}{\Delta + 2\omega_0} \right)^2 I(\mathbf{r}), \quad (2.38)$$

where $\Delta = \omega - \omega_0$ is the detuning with respect to the resonance. Thus both the dipole potential and the scattering rate scale linearly with the applied laser power. If the laser is tuned relatively close to the resonance such that $|\Delta| \ll \omega_0$, one can neglect the second term and see that the potential scales as $U_{\text{dip}} \propto 1/\Delta$ whereas the scattering rate scales as $\Gamma_{\text{sc}} \propto 1/\Delta^2$. This makes it possible to have sufficiently low heating rates while still being able to have a strong enough trapping potential when using a far detuned laser at high power. In this approximation, the sign of the potential only depends on the sign of the detuning and the two possible trap configurations can be seen in Figure 2.9. For red detuned light ($\Delta < 0$) the dipole potential is negative and thus the atoms are trapped in the intensity maximum of the beam. Thus by simply focusing a red detuned laser beam with a Gaussian intensity distribution one can create an optical trap. For blue detuned light ($\Delta > 0$) on the other hand, the dipole potential is positive and the atoms are trapped in an intensity minimum. Thus to achieve e.g. trapping of atoms in a plane, one requires a 'donut' shaped beam which is harder to achieve than a Gaussian beam. Therefore

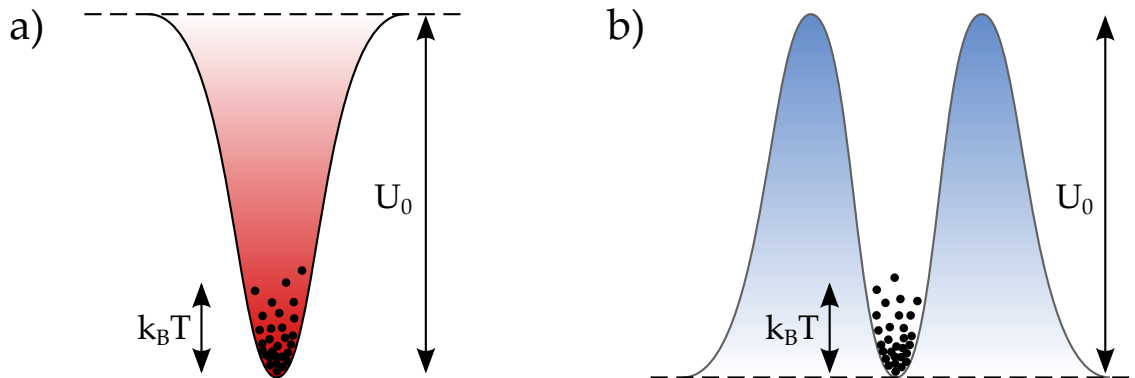


Figure 2.9.: **Illustration of red and blue detuned optical traps.** The color shaded areas show the dipole potentials of a red (a) and blue (b) detuned optical trap with a trap depth U_0 . The atoms (black dots) are always pulled towards the minimum of the dipole potential. If the energy of the atoms $E = k_B T$ is much smaller than the trap depth U_0 , the atoms only probe the center of the trap and one can use harmonic approximations. The picture is adapted from [Gri00].

blue detuned lasers are often used as optical plugs to prevent atoms from occupying certain areas. In our experiment we use a red detuned laser at wavelength of 1064 nm which is far detuned from the atomic transition frequency at about 671 nm of ${}^6\text{Li}$. Therefore our detuning $|\Delta| \approx \omega_0/2$ is on the order of the resonance frequency and thus dropping the second term would introduce an error of about 20 % for the dipole potential. Since this large detuning decreases the trap depth considerably, we have to compensate this by having a very high laser power of about 200 W.

In our dipole traps we use focussed Gaussian beams to create the confinement. Taking the z -axis as the line of propagation, their intensity profile is given by

$$I(x, y, z) = \frac{2P}{\pi w_x(z) w_y(z)} \exp \left[-2 \frac{x^2}{w_x^2(z)} - 2 \frac{y^2}{w_y^2(z)} \right], \quad (2.39)$$

with

$$w_i(z) = w_{0,i} \sqrt{1 + \left(\frac{z}{z_{R,i}} \right)^2}. \quad (2.40)$$

Here w_i denotes the $1/e^2$ radii of the beam, the beam waist $w_{0,i}$ defines the minimal radii at the focus and the Rayleigh lengths $z_{R,i} = \pi w_{0,i}^2 / \lambda$ define the distances from the focus where the according beam waist has increased by a factor of $\sqrt{2}$. In Figure 2.10 a) this case is depicted. The trapping volume is then basically determined by the beam waists $w_{x,y}$ and the Rayleigh length $z_R = \min[z_{R,x}, z_{R,y}]$. For typical beam sizes the Rayleigh length is always larger than the beam waists and thus the confinement along the propagation axis of the beam is weakest. However, one can improve the axial confinement by crossing two beams of perpendicular polarization under an angle 2ϕ which is depicted in Figure 2.10 b). Then the axial confinement is determined by the overlap length $l \approx 2w_y / \sin\phi$ given that $l < z_R$ and one can achieve a better confinement. In the experiment one often realizes this by recycling

the beam to cross it with itself. This also increases the power of the laser effectively by a factor of two, thus improving the achievable trap depths. As one can see in

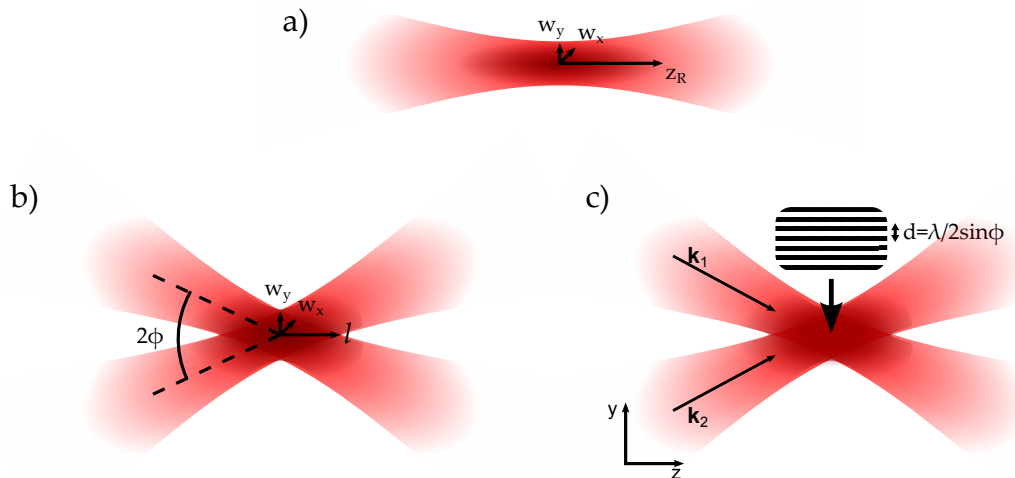


Figure 2.10.: **Illustration of different type of red-detuned optical traps.** a) Single beam trap where the atoms are confined at the focus of a Gaussian beam. The trapping volume is determined by the beam waists $w_{x,y}$ in radial direction and the Rayleigh length z_R in axial direction. b) A crossed beam trap where the beams have perpendicular polarization enhances the axial confinement to the overlap length l . c) For identical polarizations in the beams, the crossed beam trap creates an interference pattern where the distance between adjacent trap sites is determined by the crossing angle 2ϕ . The picture is adapted from [Boh12].

Figure 2.9, in our experiments we usually have the condition that the thermal energy $k_B T$ of the atoms is much smaller than the trap depth U_0 . The atoms then probe only a small volume of the trap and one can apply a harmonic approximation to calculate the energy levels. This then leads to the form

$$U_{\text{dip}} \approx -U_0 \left[1 - 2 \left(\frac{x}{w_{0,x}} \right)^2 - 2 \left(\frac{y}{w_{0,y}} \right)^2 - \left(\frac{z}{z_R} \right)^2 \right], \quad (2.41)$$

where U_0 is the trap depth at the center which is proportional to the applied laser power. This has the form of a harmonic oscillator where the level spacings $\hbar\omega_i$ are given by the trap frequencies

$$\omega_{x,y} = \sqrt{\frac{4U_0}{mw_{0,x,y}^2}} \quad \text{and} \quad \omega_z = \sqrt{\frac{2U_0}{mz_R^2}}. \quad (2.42)$$

Since U_0 scales linearly with the laser power P , this implies that $\omega_i \propto \sqrt{P}$.

Further away from the center of the trap the harmonic approximation is not good anymore. There the trap frequencies changes which has the effect that the levels closer to the edge of the trap are spaced by less than $\hbar\omega$.

Confinement in 2D and 1D

In the harmonic approximation, the axes are decoupled and the energy of each atom [Sch04]

$$E_{\text{ho}} = \hbar\omega_x \left(n_x + \frac{1}{2} \right) + \hbar\omega_y \left(n_y + \frac{1}{2} \right) + \hbar\omega_z \left(n_z + \frac{1}{2} \right) \quad (2.43)$$

depends only on the trap level n_i it occupies in each axis i . Thus by introducing large aspect ratios for the trap frequencies and limiting the number of atoms in the trap, one can achieve conditions where the dimensionality of the system is effectively reduced.

Since we deal with identical fermions, each trap level can be occupied only by a single fermion. At zero temperature, this has the effect that N identical atoms will occupy the N energetically lowest trap states up to the Fermi energy E_F . However finite temperature effects and interactions between the different spin states in the trap leads to excitations and thus also higher energy levels can be occupied.

In the case of a single beam trap where the axial trap frequency is much weaker than the radial trap frequencies ($\omega_z \ll \omega_{x,y}$) and for temperatures $k_B T \ll \hbar\omega_{x,y}$, this means that as long as the atom number N satisfies the condition

$$\hbar\omega_z N \ll \hbar \min[\omega_x, \omega_y] \quad (2.44)$$

the atoms will only be excited in the axial direction and thus the system can be regarded as quasi one-dimensional. Therefore the maximal number of atoms while still being in the 1D regime is given by the aspect ratio $N_{\text{max}} \ll \min[\omega_x, \omega_y] / \omega_z$.

In the case of an optical lattice (see Section 2.5.1), one can achieve that the confinement along one axis e.g. the z-axis, is much stronger than in the other axes and hence $\omega_{x,y} \ll \omega_z$. For temperatures $k_B T \ll \hbar\omega_z$ and demanding that the atoms are only excited in x- and y-direction to have a quasi two-dimensional system leads to the condition

$$\hbar\omega_x n_x + \hbar\omega_y n_y \ll \hbar\omega_z, \quad (2.45)$$

where the maximal number of atoms is now given by $N_{\text{max}} = n_x \cdot n_y$. This limit is reached for

$$N_{\text{max}} \ll \frac{\omega_z^2}{2\omega_x\omega_y}. \quad (2.46)$$

Hence the achievable number of atoms depends also in the 2D case only on the ratio of the trapping frequencies.

2.5.1. Crossed Beam Traps

Starting with the simple single-beam dipole trap derived above, the possibility of creating interference patterns in the intensity profile by using additional beams with identical polarization provides a tool to create all sorts of trap structures.

Interference occurs because the overall intensity of two laser beams is given by

$$I_{\text{tot}} \propto |\tilde{E}_1 + \tilde{E}_2|^2 \quad (2.47)$$

and thus depends on the relative phase between the two electric fields. In Figure 2.10 c) the general case of two Gaussian beams with identical power propagating

along \mathbf{k}_1 and \mathbf{k}_2 is depicted. If the crossing angle is again 2ϕ , this yields the total intensity

$$I_{\text{tot}} \propto I_0 |e^{ik(\cos\phi z - \sin\phi y)} + e^{ik(\cos\phi z + \sin\phi y)}|^2 = 4I_0 \cos^2\left(\frac{2\pi y}{\lambda \sin\phi}\right), \quad (2.48)$$

where $k = 2\pi/\lambda$ is the wave vector and I_0 is the intensity of a single beam. Since the trap depth is proportional to the intensity this leads directly to a periodical trap structure along the y -axis of the form

$$U_0(y) \propto \cos^2\left(\frac{\pi y}{d}\right), \quad (2.49)$$

where

$$d = \frac{\lambda}{2 \sin\phi} \quad (2.50)$$

is the spacing between adjacent trap sites. Note that the trap depth of each site is four times as large as that of a single beam trap. For the case of different beam intensities the minima are not completely dark anymore and thus the potential wall between adjacent sites is reduced.

Optical Lattices

In the case of retro-reflected beams ($\phi = 90^\circ$) one obtains a standing wave pattern which minimizes the spacing to $d = \lambda/2$ and is called an optical lattice. This can be seen in Figure 2.11 a). Since the beam waists w_i and the Rayleigh length z_R are usually much larger than the wavelength, this allows for very tight traps and thus large trapping frequencies. Therefore optical lattices are perfectly suited to create the conditions required to reduce the dimensionality of a system. Superimposing several of these standing waves, one can then e.g. create structures like arrays of one-dimensional tubes or a three-dimensional lattice where each site is effectively zero-dimensional (see Figure 2.11). Especially the latter ones allow to investigate theoretical models from solid state physics and are thus a main field of research.

2.5.2. Heating in Optical Traps

Heating in dipole traps is a major concern since most of the interesting physics in lattices happens at temperatures far below the Fermi temperature $T_F = E_F/k_B$ ¹¹ and thus heating can impose severe limitations to the accessible regimes. The fundamental mechanism of heating in a dipole trap is the spontaneous scattering of trap photons. As can be seen from equation (2.38), when using the approximation $|\Delta| \ll \omega_0$ the scattering rate Γ_{sc} in the center of the trap directly relates to the trap depth U_0 as

$$\Gamma_{\text{sc}} = \frac{\Gamma}{\hbar\Delta} U_0. \quad (2.51)$$

As already mentioned, it is therefore advantageous to be far detuned from resonance to have low heating rates. However, one can also see that in optical lattices the

¹¹It denotes the energy of the highest occupied state at $T = 0$.

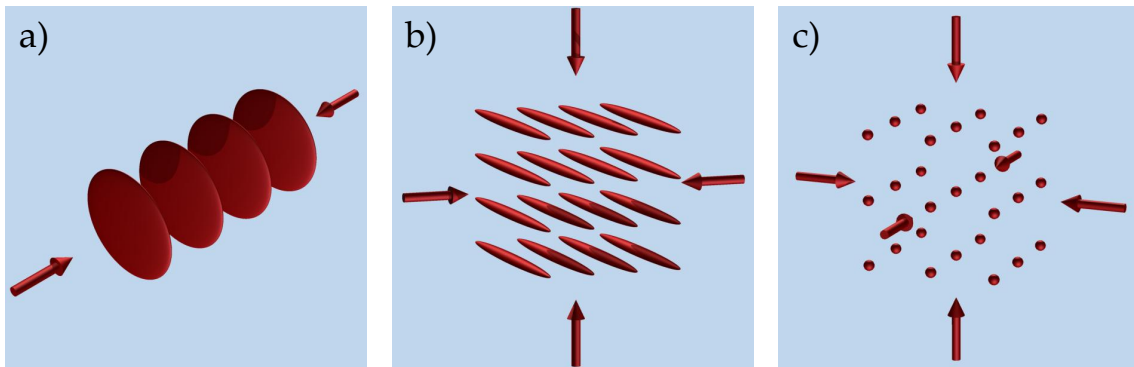


Figure 2.11.: **Illustration of the different kind of lattice structures.** Assuming Gaussian beams, one retro-reflected beam creates a one-dimensional lattice of pancake shaped traps (a). Two orthogonal retro-reflected beams create a two-dimensional array of cigar shaped traps (b). Using three orthogonal standing waves then creates a three-dimensional optical lattice (c). The picture is taken from [Boh12].

problem increases as well since the trap depth U_0 is enhanced by interference effects and thus the scattering rate is increased as well.

Introducing a mean photon scattering rate $\bar{\Gamma}_{sc}$ across the trap, this leads to a linear heating rate of

$$\dot{T} = \frac{1}{3} T_{rec} \bar{\Gamma}_{sc}, \quad (2.52)$$

where $T_{rec} = \hbar^2 k^2 / (2mk_B)$ is the recoil temperature. Thus for lighter alkali atoms like ${}^6\text{Li}$ this heating is more pronounced due to their larger recoil temperature.

Apart from this fundamental source, heating can also occur due to technical reasons like intensity fluctuations or pointing instabilities in the trapping beams [Geh98]. These mechanisms lead to heating which strongly increases for larger trap frequencies. Therefore they can be a limiting factor in lattice experiments, where the trap frequencies can be on the order of 100 kHz and thus one relies on low-noise laser sources and very stable optics to create the lattices.

In Section 3.2.2, the heating caused by intensity fluctuations is explained in more detail and its influence compared to the photon scattering is estimated for our experimental setup.

3. Experimental Setup

Conducting experiments on ultracold atoms requires to first trap a sample of atoms and then use a sequence of cooling schemes to enter the quantum degenerate regime. In this chapter our preparation of such an ultracold atomic sample is summarized and the main features of our apparatus are explained.

A detailed description of the status quo of our experiment at the beginning of this thesis can be found in the Diploma Theses of Johanna Bohn [Boh12], Phillip Simon [Sim10] and Martin Ries [Rie10]. Up to this point, a mixture of atoms in states $|1\rangle$ and $|2\rangle$ inside a 3D optical dipole trap had been evaporatively cooled both into a quantum degenerate Fermi gas (DFG) and a molecular Bose-Einstein condensate (mBEC). All the required steps to achieve this are briefly reviewed in Section 3.1. Subsequently the newly added setup to create the pancake shaped dipole traps which provide the 2D confinement in the optical lattice is introduced in detail in Section 3.2. At last, our rf-setup which is used to transfer atoms between different hyperfine states is described in Section 3.3 and all our current imaging possibilities are listed in Section 3.4.

3.1. Preparation of an Ultracold Fermi Gas

In the following, we summarize the basic characteristics of our apparatus as well as explain the required steps to prepare an ultracold Fermi gas as depicted in the timing graph in Figure 3.1.

3.1.1. Experimental Control

All devices that need to be controlled during an experimental cycle are addressed with a combination of digital and analog channels. To regulate these channels we use an ADwin Pro II real-time control system with 32 digital outputs, 16 analog outputs and 8 analog inputs.

Using analog-digital converters (ADC) and digital-analog converters (DAC), one can use the analog input channels to provide a digital PID-feedback to the analog output channels. The speed of the ADC's and DAC's sets the limit on the achievable bandwidth to 100 kHz, implying that each analog channel is updated every $10\ \mu\text{s}$. In contrast, the digital channels have a bandwidth of 1 MHz and can thus be updated each μs .

The ADwin Pro II receives its timing table for all the channels from a LabView user interface via Ethernet. This user interface also controls the cameras and evaluates their data. The whole setup is such that one can do automated runs while simultaneously analyzing the data. More details on the experimental control can also be found e.g. in [Lom08, Zür09].

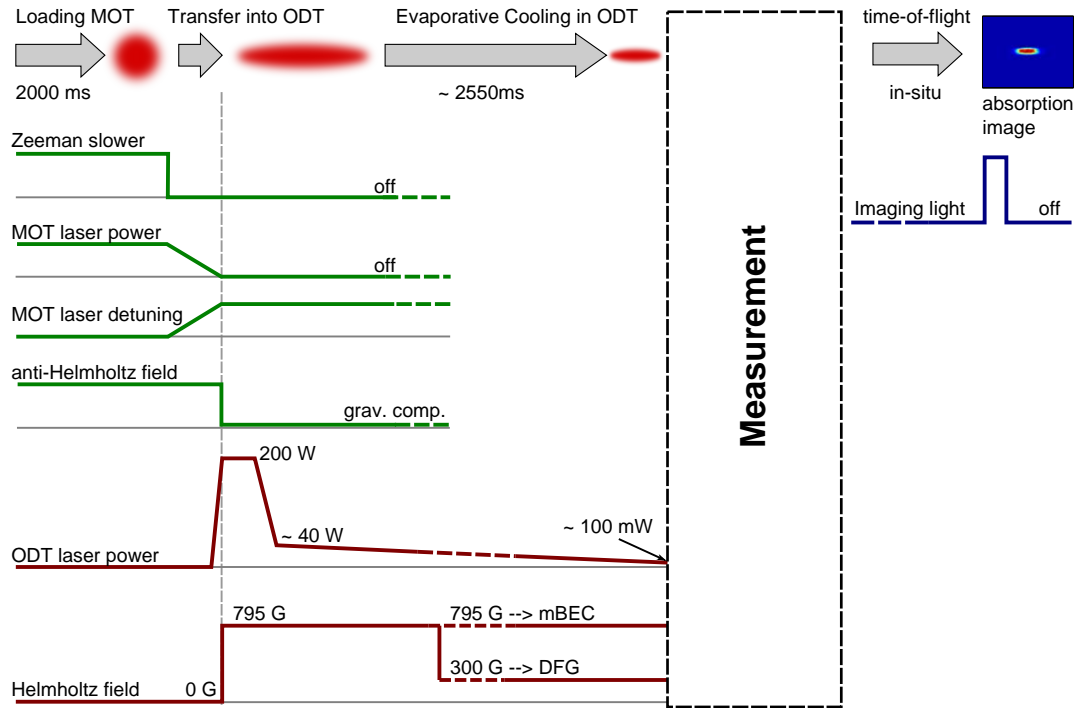


Figure 3.1.: **Illustration of the timing graph to produce an ultracold Fermi gas.** At the top the main steps are shown: the loading of the MOT, the transfer into the optical dipole trap and subsequent evaporative cooling of the atomic cloud. This is then the starting point for our measurements after which we can investigate the density profile of the cloud either in time-of-flight (TOF) or in-situ absorption imaging. Depending at which magnetic offset field the final evaporation is performed, one ends up either with a molecular BEC ($B \approx 795$ G) or a degenerate Fermi gas ($B \approx 300$ G). Note that this is a simplification of our experimental sequence and that the times and amplitudes do not scale and just show the qualitative behavior.

3.1.2. Vacuum, Oven & Experiment Chamber

Cooling atoms down to ultracold temperatures requires an ultra high vacuum (UHV) since any collisions with thermal background gas would eject atoms from the trap immediately. A drawing of our vacuum setup can be seen in Figure 3.2. The experiment chamber is connected to the oven via a differential pumping stage¹ to suppress any negative effect of the higher pressure inside the oven chamber. This leads to a pressure $P_{\text{exp}} \leq 10^{-11}$ mbar inside our experiment chamber and a vacuum limited lifetime of 23 min in the magneto-optical trap (MOT). Therefore on the timescale of our experiments (~ 10 s) we can neglect any losses due to the background gas. The experiment chamber is pumped by a titanium sublimation pump (VARIAN) in addition with an ion-pump (VARIAN StarCell 75) to pump non-reactive gases like He or Ar. In addition, the octagonal chamber itself is coated from the inside with a so-called 'Non Evaporable Getter coating' (NEG) from GSI, which consists of a TiZrV alloy. It acts as another getter surface and also prevents outgassing from the octagon walls, thus further reducing the pressure inside the experiment chamber. The oven chamber is pumped with another titanium sublimation pump (VARIAN)

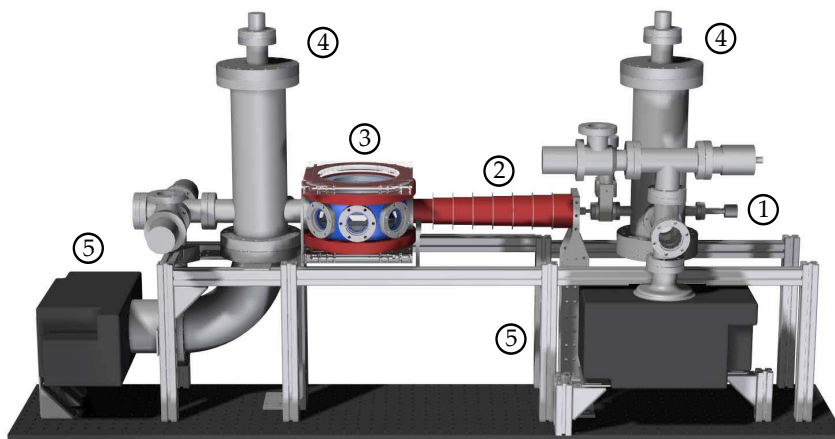


Figure 3.2.: **The vacuum chamber.** ${}^6\text{Li}$ is heated up to $\sim 350^\circ\text{C}$ in the oven (1). This produces a flux of atoms going through the Zeeman slower (2) to the experiment chamber (3). There, the atoms are first trapped in a MOT and later transferred to optical traps. Six viewports on the side of the spherical octagon and two re-entrant viewports on its top and bottom allow optical access to the experiment. The two towers (4) provide the gettering surfaces for the titanium sublimator pumps as well as connections to the ion pumps (5). The picture is adapted from [Rie10].

and a slightly smaller ion-pump (VARIAN StarCell 40). The pressure at the oven is $P_{\text{oven}} \approx 3 \cdot 10^{-11}$ mbar and it is connected to the experiment chamber via the Zeeman slower tube which also acts as a differential pumping stage.

The oven itself is filled with a few grams of ${}^6\text{Li}$ and operated at $T_{\text{oven}} = 350^\circ\text{C}$,

¹The differential pumping stage is provided by the Zeeman slower tube.

well above the melting point of $T \approx 180^\circ\text{C}$. To block the atomic flux from the oven, a mechanical shutter can be rotated into the atomic beam path.

The experiment chamber itself is a spherical octagon which is constructed with non-magnetic steel. This is important because one does not want any magnetization disturbing the magnetic offset fields needed to tune the interactions. For optical access, the chamber has six viewports on the sides and two re-entrant viewports at the top and bottom. This enables us to shine in all the necessary beams for the magneto-optical trapping (MOT), optical trapping and imaging. The side viewports have a numerical aperture of $\text{NA}_{\text{hor}} = 0.15$ and therefore limit the theoretical maximal achievable resolution to $d_{\text{min}}^{\text{hor}} = \frac{0.61\lambda}{\text{NA}} = 2.78 \mu\text{m}$ ($\lambda = 671 \text{ nm}$, Rayleigh criterium). As one can see in Figure 3.3, the vertical viewports are much closer to the center of the chamber and thereby provide a larger numerical aperture of $\text{NA}_{\text{vert}} = 0.88$. In comparison, this leads to a maximal achievable resolution of $d_{\text{min}}^{\text{vert}} = 465 \text{ nm}$. We want to use this in the future when we put in a new objective with a numerical aperture of $\text{NA} = 0.6$ which was designed in our group [Ser11] and has been tested in a soon to be published master thesis [Ber13]. For $\lambda = 671 \text{ nm}$, the new objective was tested to have at least² a resolution of $d_{\text{min}}^{\text{hor}} = 1.01 \mu\text{m}$.

As one can see in Figure 3.3, the design of the chamber is also such that the coils which produce the homogeneous magnetic offset field can be placed very close to the atoms. This means that we do not need that many windings in the coil (30 windings at a current of 200 A), which reduces its inductivity and thus accelerates any switching processes during an experiment cycle.

More information on the vacuum chamber or the oven can also be found in [Rie10].

3.1.3. Laser Cooling and Magneto-Optical Trapping

In order to prepare ultracold atoms, the hot atomic flux coming from the oven has to be cooled down low enough to allow for trapping. The technique to do this and the first trapping and cooling step is explained in the following.

Zeeman Slower

Since the atoms emerging from the oven have an average velocity $\bar{v} \approx 1500 \text{ m/s}$, but the maximum capture velocity in the magneto-optical trap (MOT) is $v_{\text{capture}} \approx 50 \text{ m/s}$, they have to be slowed down before entering the experiment chamber.

This can be done by decelerating the atoms with a resonant laser beam which is directed opposite to the flux of atoms. This so-called laser cooling can be understood quite simply by considering the atom as a two-level system³ described by a ground state $|g\rangle$ and an excited state $|e\rangle$ (see e.g. [Met99]). When getting excited by a laser photon to state $|e\rangle$, the atom absorbs the photon momentum \mathbf{p}_λ which is directed

²The calculated resolution is 680 nm. However the pinhole used to measure the point-spread-function had a size of 650 nm which is on the same order and thus affects the measurement negatively.

³In the experiment, this condition is not always fulfilled and one has to consider additional atomic energy levels.

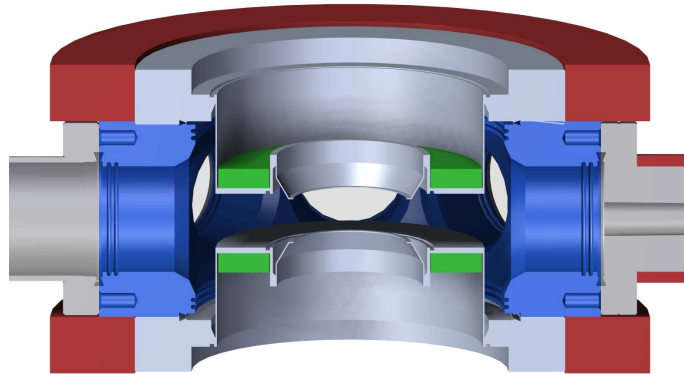


Figure 3.3.: **Vertical cut through a drawing of the experiment chamber.**

The MOT coils (red) produce the anti-Helmholtz magnetic configuration needed for trapping in the MOT. By switching the current flow direction, they can also be used to compensate gravitation during experiments in the optical traps. The Feshbach coils (green) produce the strong magnetic offset field needed to tune the interaction via Feshbach resonances. They are mounted very close to the atoms to reduce the required currents. The picture is taken from [Rie10].

opposite to the atom's initial momentum \mathbf{p}_{atom} . Spontaneous emission of a photon after some lifetime τ in the excited state $|e\rangle$ then leads to a decay of the atom back into the ground state $|g\rangle$. Since this spontaneous process has no preferred direction to emit the photon, the experienced recoil $-\mathbf{p}_\lambda$ is randomly distributed and thus evens out when averaging over many of these events. Therefore the atom will only add up the directed recoil from absorbing the laser photons and thus will slow down⁴. This effect is known as the spontaneous light force and can be described by [Met99]

$$\langle F \rangle = \hbar \mathbf{k} \Gamma_{sc}, \quad (3.1)$$

where Γ_{sc} is the scattering rate of photons and \mathbf{k} is the momentum of the absorbed photon. The scattering rate depends on the linewidth γ of the excited state, the intensity saturation $s_0 \equiv I/I_s$ and the detuning δ of the laser from the resonance frequency as follows [Met99]

$$\Gamma_{sc} = \frac{s_0 \gamma / 2}{1 + s_0 + \left(\frac{2\delta}{\gamma}\right)^2}. \quad (3.2)$$

Therefore, to have a large scattering rate and thus a strong deceleration, one needs to be in resonance ($\delta = 0$) and have enough power to saturate the transition ($s_0 > 1$).

Because the atoms move towards the laser source, one also has to consider the Doppler shift $\delta_{\text{Doppler}}(\mathbf{v})$ the atoms experience. This requires the laser light to be red-detuned to the transition by a detuning δ_{Laser} . However if the atoms are initially in resonance to the transition, the deceleration would quickly move them out of

⁴In fact it makes a jittering movement, since the spontaneous emission can be seen as a random walk process perpendicular to the beam [Jof93].

resonance leading to non-efficient cooling. One can compensate for this effect by applying a spatially varying magnetic field which introduces an additional spatially dependent Zeeman shift $\delta_{\text{Zeeman}}(\mathbf{x})$. Thus when taking all effects into account, one can satisfy the resonance condition

$$0 \equiv \delta_{\text{Laser}} + \delta_{\text{Doppler}} + \delta_{\text{Zeeman}} \quad (3.3)$$

along the whole length of the slower and achieve an efficient deceleration. Due to the use of the Zeeman shift, this is called a Zeeman slower.

In our setup we use a decreasing field configuration for the Zeeman slower. This has the advantage that the additional magnetic fields due to the slower are small at the place of the atoms but the disadvantage that the laser light is not far detuned from the resonance frequency which can cause unwanted excitations during the MOT trapping. An additional advantage of this slower configuration is that we can use the magnetic field of the MOT coils to provide the last part of the slower field. This makes the Zeeman slower more compact and we capture the atoms closer to the end of the slower where their expansion perpendicular to the slower axis is smaller.

More information on the Zeeman slower can be found in [\[Sim10\]](#).

Magneto Optical Trap (MOT)

The slow atoms entering the experiment chamber are then trapped using a magneto-optical trap (MOT). The principle of MOT trapping is as follows: shining in perpendicular, counter-propagating near-resonant laser beams from all three directions damps down the movement of the atoms, thus cooling them. Such a configuration is called an optical molasses and its basic properties can be found in many textbooks e.g. [\[Met99\]](#). Although optical molasses provide velocity dependent cooling of the atoms, there is no spatial confinement and thus the atoms can move out of the overlap of the beams and are lost from the trap. Therefore one needs an additional spatial confinement which is provided by applying a magnetic field gradient (see Figure 3.4 a)). The magnetic field gradient splits the energy levels of different magnetic sublevels m_J and thus allows for spatially dependent absorption of photons. The basic principle of the 1D case can be seen in Figure 3.4 b)). In a two-level system, the excited state $|e\rangle$ splits into three different magnetic sublevels $m_J = 0, \pm 1$ which tune differently in respect to the magnetic field gradient. Because we work in a local spin picture and the magnetic field and thus the quantization axis changes its sign at $B = 0$, the energy of the $m_J = -1$ excited state always decreases with increasing magnetic field amplitude. The near-resonant lasers have a detuning δ_0 and polarization σ^- thus allowing for transitions from the ground state $|g, m_J = 0\rangle$ to the excited state $|e, m_J = -1\rangle$. When an atom now moves out of the trap center to the left, the laser beam coming from the left becomes resonant at $z = -R_c$ thus pushing the atom back towards the center of the trap. Although this laser is also resonant at $z = +R_c$, it does not effect the atoms there because the quantization axis changes at $B = 0$ and thus the beam is seen from atoms on the right side as σ^+ -polarized. For more details on this one can again refer to [\[Met99\]](#).

Thus the combination of an optical molasse with a magnetic field gradient provides the first step to effectively trap and cool our atoms into the sub mK regime. The

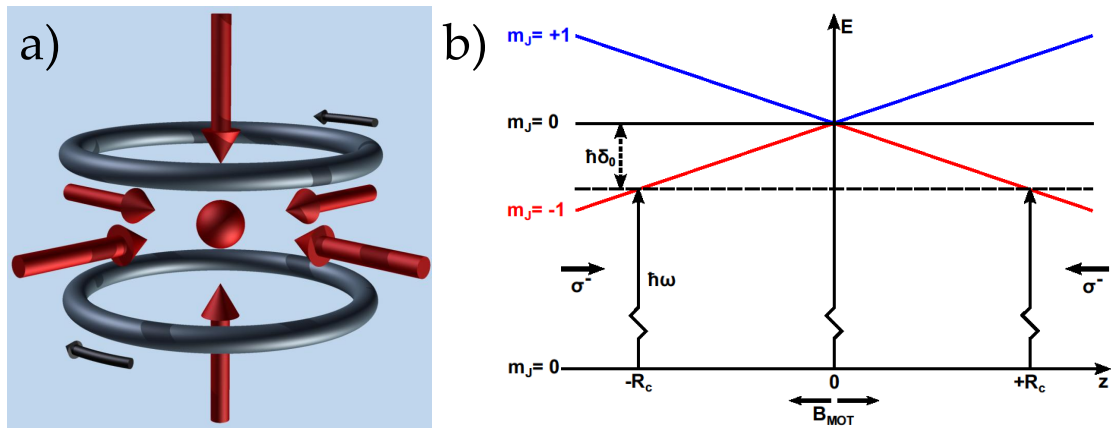


Figure 3.4.: **Basic principles of a MOT.** a) Six laser beams in combination with two coils in anti-Helmholtz configuration supply the spatial confinement and cooling. b) A magnetic gradient splits the magnetic sublevels of the excited state. At the center of the trap the magnetic field is zero and hence the quantization axis changes. This has the effect that the atomic transition becomes resonant with the laser at positions $\pm R_c$. Since the atom can only absorb light with the correct circular polarization, this leads to a net force which is directed towards the center of the trap. The picture is adapted from [Rie10, Boh12].

achievable temperature in the MOT is limited by the Doppler limit T_D [Met99]. In our case of ${}^6\text{Li}$, we achieve typical final temperatures on the order of about $300\ \mu\text{K}$ in the MOT which is close to the Doppler limit of $T_D = 137.6\ \mu\text{K}$. More information on the performance of the MOT can be found in [Rie10].

Optical Setup

${}^6\text{Li}$ is not a simple two-level system because after being excited to the $|2^2P_{3/2}\rangle$ state⁵, the atoms can relax into the $|2^2S_{1/2}F = 1/2\rangle$, as well as into the $|2^2S_{1/2}F = 3/2\rangle$ ground state⁶. Therefore one needs two laser frequencies, a *cooler* ($|g, F = 3/2\rangle \rightarrow |e\rangle$) and a *repumper* ($|g, F = 1/2\rangle \rightarrow |e\rangle$) to address both transitions. The hyperfine splitting between the ground states is approximately 228 MHz and can be achieved by shifting the cooler (repumper) laser light by $-114\ \text{MHz}$ ($+114\ \text{MHz}$) with an acousto-optic modulator (AOM).

We produce all the near-resonant laser light required for laser cooling and MOT trapping on a separate optical table using a TOPTICA TA Pro, consisting of a grating stabilized diode laser [Ric95] which seeds a tapered amplifier and provides an output power of approximately 350 mW with a linewidth of less than 1 MHz. The frequency of the laser is stabilized using a beat offset lock to a frequency reference. This reference is a TOPTICA DL 100 which is stabilized using Doppler-free frequency-modulation spectroscopy of ${}^6\text{Li}$ -vapor [Ser07].

⁵The hyperfine states of the excited state are not resolved since their splitting is smaller than the natural linewidth of the transition.

⁶The ratio is 1:2.

3. Experimental Setup

The output beam from the TA is then split into two beams which are subsequently shifted by 228 MHz with respect to each other using the first order diffraction of two AOMs to allow for a cooler and a repumper beam. Each of these beams is then split into three separate beams for the MOT and one additional beam for the Zeeman slower which is again shifted by an AOM. The cooler and repumper beams are then overlapped again before coupling them into polarization maintaining single-mode fibers which link the optical setup to the experiment table. The whole optical setup is described in detail in [Rie10]. We create the counterpropagating MOT beams

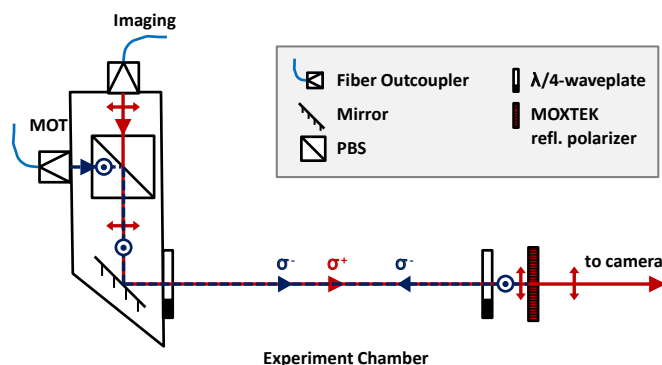


Figure 3.5.: **Sketch of the Imaging/MOT outcoupler.** The imaging and MOT beam have perpendicular linear polarization and are overlapped using a polarizing beam splitter (PBS). Before entering the experiment chamber, the beams pass a $\lambda/4$ -waveplate, resulting in perpendicular circular polarizations for the beams. After the chamber, an additional $\lambda/4$ -waveplate undoes this transformation and the beams are separated using a MOXTEK reflective polarizer, transmitting the imaging beam but reflecting the MOT beam. Passing the $\lambda/4$ -waveplate again on its way back, the MOT beam has then the correct circular polarization for the atoms in the MOT.

via reflection using a combination of a $\lambda/4$ -waveplate and a MOXTEK reflective polarizer. This is done because we also want to image along the MOT axes and hence need to separate the imaging beam from the MOT beam. A sketch and explanation of our outcoupler setup can be seen in Figure 3.5.

MOT coils

The magnetic field gradient for the MOT is generated via two coils in anti-Helmholtz configuration which are directly mounted on top and bottom of the experiment chamber (see Figure 3.3). Each of the coils consists of four stacked coils with 25 windings each. Therefore the MOT coils have a larger inductivity compared to the Feshbach coils thus making any switching process slower. To avoid overheating, the coils are glued with thermally conductive epoxy onto water cooled copper heat sinks. The current direction and thus the gradient can be reversed using a logical

circuit. Thereby we can use the MOT coils later in the experiment to compensate the gravitational force on the atoms by applying an appropriate gradient.

For more information on the coils, one can again refer to [Rie10].

3.1.4. Transfer into the Optical Dipole Trap and Evaporative Cooling

After cooling down the atoms in the MOT to several hundred μK , we have to transfer them into an optical dipole trap (ODT). It relies on the conservative dipole force in an electrical field and its theory is described in more detail in Section 2.5. Since the far off resonant light does not get scattered, one does not heat up the atoms and thus can apply further cooling.

As our source for the far off-resonant light, we use a diode pumped single-mode, linearly polarized Ytterbium fiber laser (IPG Photonics) with an output power of 200 W. It is not single mode in frequency space which degrades its noise characteristics (see Section 3.2.2) but plays no role in our application. We use crossed, elliptical beams to create a surfboard shaped trap with an optical setup which is shown in Figure 3.8 and described in detail in [Boh12].

The transfer from the MOT into the ODT is done as follows: 1 ms before the dipole trap is turned on, the repumper light is turned off and the intensity in the cooler beam is reduced. Thereby the atoms accumulate in the ground state $|2^2S_{1/2}F = 1/2\rangle$, thus providing us with atoms in state $|1\rangle$ and $|2\rangle$ when increasing the magnetic offset field during evaporation. Simultaneously we use the Feshbach coils in anti-Helmholtz configuration to produce a steeper MOT gradient, thus compressing the MOT and allowing for a better overlap of the traps. Then the dipole trap laser is switch on to 200 W to begin the transfer. At this high power, thermal lensing occurs which shifts the trap and thus the position of the ODT at high power does not coincide with the position at low power. In addition, the position of the zero-crossing of the Feshbach gradient does not coincide with the final position of the dipole trap. Therefore the position of the MOT has to be moved during the transfer. For this purpose we implemented several features. To shift the MOT position vertically, a parallel circuit was added to the lower coil to 'steal' current and thus move the trap center. In the horizontal plane, we can use the last Zeeman slower coil to shift the position along the slower axis and an additional coil at the viewport where the dipole trap beam enters the chamber to shift the MOT along the dipole trap axis. This control in all three axes then enables us to overlap the traps satisfyingly during the transfer.

After the transfer the power in the dipole trap laser is reduced to 40 W which then shifts the dipole trap to its final position. In total, this allows us to transfer about 1 % of the atoms into the dipole trap which leaves us about 10^7 atoms to start the further cooling process.

Evaporative Cooling

The cooling mechanism of choice is so-called evaporative cooling. Its basic idea is very simple: the atoms in a thermal cloud have a Maxwell-Boltzmann velocity

distribution and the temperature of the cloud is connected to the mean velocity of the gas. Hence by removing the fastest (and therefore most energetic) atoms in the cloud, one reduces the mean velocity of the remaining atoms. When given time to re-thermalize via collisions, the atoms then again have a Maxwell-Boltzmann velocity distribution but now at a lower temperature. Hence by spilling fast atoms from the trap in a controlled manner and giving the cloud time to re-thermalize, one can cool down the cloud into the ultracold regime at the cost of atom number.

In the experiment, the spilling is done by lowering the trap depth via the applied laser power. The laser power can be monitored with the help of two photodiodes which collect the transmitted light behind a mirror (see Figure 3.8) and is stabilized using a PID-feedback which controls the diffraction efficiency of two perpendicularly crossed AOMs. To allow for fast re-thermalization, the evaporation is normally done on the repulsive side at magnetic field strengths where the scattering length a is large and positive. If one wants to create a mBEC, one chooses a magnetic field close to the resonance where the Feshbach molecules are still stable (typically $B \approx 796$ G). If one is interested in a Fermi gas of atoms in $|1\rangle$ and $|2\rangle$, one evaporates further away from the resonance (typically $B \approx 300$ G) where the scattering length is negative and thus no molecules are formed. Since at low temperatures collisions can only occur between different spin states, a long rf-pulse (~ 600 ms) is applied directly before the evaporation to balance the atoms between state $|1\rangle$ and $|2\rangle$ and thus enable efficient cooling.

Feshbach coils

To produce the homogeneous magnetic offset fields on the order of 1000 G required to tune the scattering length a in the vicinity of the Feshbach resonance, we use two coils in Helmholtz configuration which are mounted very close to the position of the atoms (see Figure 3.3). Each coil has 30 windings and currents up to 200 A can flow through them. Therefore they are glued onto water-cooled heat sinks.

The coils are mounted slightly farther apart than in the exact Helmholtz configuration. Thereby one creates a magnetic field saddle which causes a weak anti-trapping potential in vertical direction and a trapping potential in the horizontal plane for the high-field seeking states $|1\rangle$, $|2\rangle$ and $|3\rangle$. This helps to strengthen the trapping along the axis of the dipole beam which has the weakest optical confinement. Because the current connectors introduce asymmetric distortions to the desired magnetic field, we inserted small blocks of ferromagnetic steel on the Feshbach coils to counteract these. By iteratively positioning these blocks on the coils, we could achieve that the magnetic field saddle, onto which we align the ODT, is closer to the position of the MOT, which increases the efficiency of the transfer.

To stabilize the magnetic offset field at the required value, we measure the current through the coils using a Danfysik Ultrastab 866 current transducer and use a PID-feedback loop to control the voltage of the Delta Elektronika SM 30-200 power supply. In the other experiment in our group the same setup is used and a magnetic field stability of up to 5 mG is achieved [Zür12, Zür13]. In our experiment, the achievable magnetic field stability should be slightly worse since we only use 5 V of

the available 10 V from the ADWIN analog control to regulate the power supply⁷. Hence we could improve the dynamical range of our control using the whole 10 V range by putting a voltage divider before the Delta Electronika power supply. At worst, this should still give us a magnetic field stability better than 10 mG. In the experimental results chapter, we can confirm that our magnetic field stability is on the expected order, since we measure a drift smaller than 20 mG over the course of a week using an rf-tomographic measurement.

3.2. The Pancake Trap Setup

As explained in chapter 1, we want to prepare a three-component Fermi gas in an optical lattice. Since we want the gas to be quasi two-dimensional, we need a large ratio between the horizontal and vertical trapping frequencies. Hence we need a trap which tightly confines the atoms in the vertical axis.

We want to achieve this by loading the degenerate gas from the dipole trap into a stack of pancake shaped potentials which are created by the interference pattern of two vertically intersecting beams as explained in Section 2.5.1. To obtain a large aspect ratio in the pancake trap and thus allow to confine a large number of atoms in two dimensions, one needs a small vertical spacing between the pancakes which is done by increasing the intersection angle. In the experiment, we are limited by the viewports which allow for a crossing angle of $\sim 7^\circ$ relative to the horizontal plane which results in a pancake spacing of $d_{PC} \approx 4 \mu\text{m}$. Since we want the confining potential to be round in the horizontal plane, this requires the aspect ratio of the focal beam waists to be 1:8 and we planned them to be $\omega_{0,\text{vert}} = 75 \mu\text{m}$ and $\omega_{0,\text{hor}} = 600 \mu\text{m}$ which would lead to a pancake diameter of about $\varnothing = 1.2 \text{ mm}$. In total, this should allow us to load $\sim 48,000$ atoms per spin state into the optical lattice while still being quasi two-dimensional. This number is independent of the laser power since it only depends only on the ratio of the trap frequencies. To achieve at least a trap depth of $V_0 = 6.8 \mu\text{K}$, a power of 2 W is needed in each pancake beam. More information on the design criteria of the pancake trap can also be found in [Boh12].

In order to conduct experiments in a 2D optical lattice, we have to be able to reproducibly load the same pancake over long times. Therefore, the positional stability of the pancake traps has to be such that long time drifts are much smaller than half the pancake spacing d_{PC} and shot-to-shot fluctuations should be negligible. Apart from the positional stability, we also need to achieve very low temperatures to be able to observe interesting physics in the lattice. Therefore any strong heating occurring in the lattice due to intensity fluctuations of the laser would be fatal. Hence we need a low-noise laser source to produce the pancake and lattice beams.

To obtain a high passive stability of the interference fringes, we constructed a compact aluminium casing in which all the required optical elements are mounted and which can be itself fixed on the optical table (see Figure 3.6), thus dampening mechanical oscillations. The design of the casing is as follows: the beam enters the box under an angle of 45° and is split at a 50/50 non-polarizing beam splitter⁸. Each

⁷Its remote control input can only handle up to 5 V.

⁸The ratio between the two beams is not exactly 50:50 but 47:53.

3. Experimental Setup

beam is then reflected by a mirror and leaves the box under the above mentioned 7° angle. This symmetric setup avoids any negative effects which could be produced by shifts in the optical pathlengths due to a change in air pressure. The focusing of the beam into the experiment is done by inserting a $f = 900$ mm lens before the casing (see Figure 3.8). The stability has been tested with an external setup in

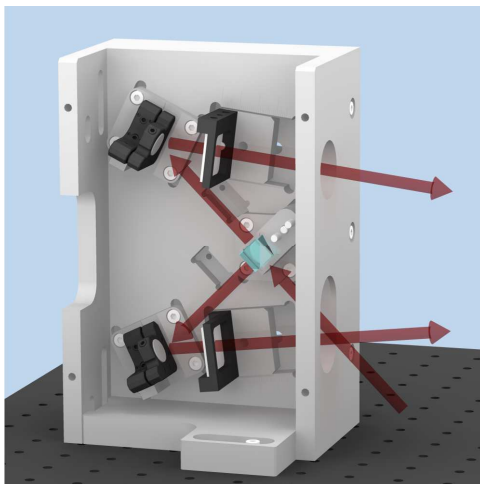


Figure 3.6.: **Illustration of the compact pancake trap setup.** The beam is split by a 50/50 non-polarizing beam splitter and directed by two mirrors into the experiment chamber. There the beams intersect to form the stack of pancake shaped traps. In the upper beam path a $\lambda/2$ -waveplate can be inserted to rotate the polarization and turn off the interference. The two cylindrical lenses in the beam paths are not included in the final setup and are replaced by a single spherical lens in front of the casing. The picture is taken from [Boh12].

a bachelor thesis [Sta12]. This was done by imaging the interference fringes onto a CCD camera and measuring the phase drifts over several weeks. Over a period of three weeks, the phase drifts were $\Delta\phi \leq 0.6\pi$, which indicates a good overall stability. Shot-to-shot fluctuations were much smaller at around $\Delta\phi \leq \pi/30$. Since then, the box has been further improved by connecting the front and back panel of the box better to the ground plate. This should further suppress oscillations and hence improve the positional stability.

3.2.1. Optical Setup

As our laser source we use a 50 W NUFERN fiber amplifier operating at $\lambda = 1064$ nm. It amplifies the seed light coming from a low-noise continuous-wave single-frequency 1064 nm solid-state laser (INNOLIGHT Mephisto-S 500 NE) with an output power of 500 mW. The Mephisto has an active intensity noise reduction (noise-eater) and a very narrow linewidth (≤ 1 kHz), thus we expect the NUFERN to have low-noise characteristics as well. To confirm this, we measured the relative intensity noise (RIN) of both lasers (see Section 3.2.2).

Apart from providing the beams to create the pancake potentials, we will also use the NUFERN laser for the beams which create the optical lattice. Therefore the output beam has to be split into three paths. For this purpose a breadboard has been set up above the NUFERN where the separation is done and the individual beams are then coupled into high-power fibers (OZ Optics) going to the experiment. Besides linking the breadboard to the experiment, putting the laser light through a fiber also helps to have a well defined laser mode in the experiment. A sketch of the setup is shown in Figure 3.7: the output beam has a slight angle coming out of the fiber and hence the collimator (two $f = 150$ mm lenses $\rightarrow f_{\text{eff}} = 75$ mm) is mounted with an angle relative to the fiber. The collimation is chosen such that one has a large beam diameter thereby reducing the effects of thermal lensing at high powers. After collimation, the beam has a Gaussian diameter⁹ of about 4.4 mm and passes a low-order $\lambda/2$ -waveplate before going through an optical isolator (Thorlabs IO-10-1064 VHP). The optical isolator prevents back reflections into the fiber and the waveplate is used to minimize losses in the isolator. The transmission of the isolator is $\sim 92\%$ and its clear aperture diameter is $\varnothing = 9$ mm, hence well above the beam diameter. Since the polarization is rotated by 45° after the optical isolator, an additional low-order $\lambda/2$ -waveplate directly after it is used to make sure that the polarization axis is aligned horizontally. Subsequently, the beam is split in three parts by the combination of several low-order $\lambda/2$ -waveplates and polarizing beam splitters (PBS). In addition, power can be taken out of the paths and be dumped with two additional $\lambda/2$ -waveplate and PBS combinations before the splitting which also leaves the option of implementing additional paths if ever needed.

In each arm, a telescope consisting of anti-reflection (AR) coated $f = 300$ mm and $f = -75$ mm spherical lenses is set up to reduce the beam size by a factor of 4. This is needed to match the beam size to the size of the AOM crystal and also to the in- and outcoupler of the high-power fibers, which in our case result in a Gaussian beam diameter of about 1.25 mm. This ensures a high coupling efficiency of about 80% which is essential since we want to couple in up to 8 W of laser power into these fibers. The $f = 300$ mm lens is mounted such that it can be tilted in both axes to account for astigmatism which occurs at high beam powers due to thermal lensing. Hence the whole setup was optimized at high powers as well. To regulate the laser power in each beam path, the first diffraction order after going through an acousto-optical modulator (AOM) is selected with an aperture¹⁰. By adjusting the radio-frequency (rf) power which drives the AOM, the diffraction efficiency can be controlled precisely and thus the power in each beam can be adjusted. The intensity stabilization is done by collecting a small fraction of the light after the fiber on a photodiode (see e.g. Figure 3.8 for the case of the pancake beam) and using a PID-feedback loop which is done digitally with the ADwin experimental control to regulate the rf-power of the AOM. The PID-feedback loop is done digitally with the ADWIN experimental control. Apart from regulating the power in the beams, the AOM's can also be used to switch the beam on and off during an experiment cycle by turning off the rf-power to the AOM's and thus dumping the non-diffracted beam.

⁹The Gaussian diameter is defined as the width where the intensity of the beam dropped to $1/e^2$.

¹⁰The aperture is inside a beam dump to cope with the high-powers.

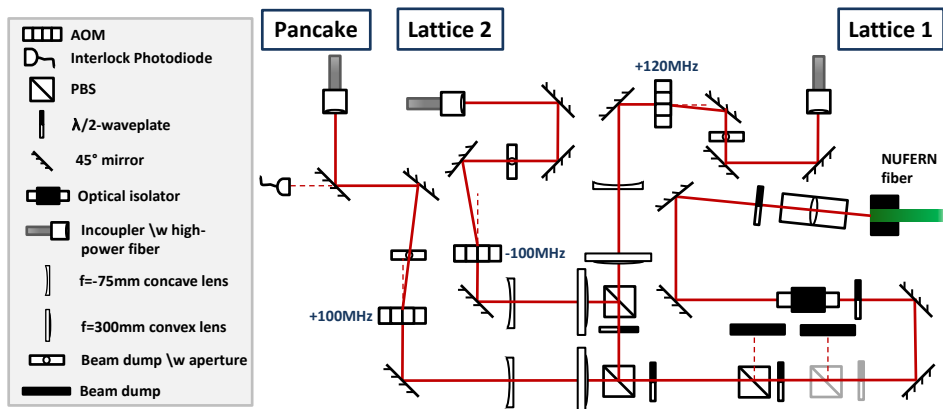


Figure 3.7.: **Sketch of the NUFERN breadboard.** The gray shaded polarizing beam splitter and $\lambda/2$ -waveplate can be rotated into the beam path in order to dump power when aligning the setup at high powers.

Because the three beam paths are overlapped in the experimental chamber, one wants to make sure that no frequency beating occurs in the critical range up to 100 kHz which could lead to heating of atoms and hence losses. Therefore the frequency of each arm is shifted differently with the AOM's. The pancake beam is shifted by +100 MHz, the first lattice beam is shifted by +120 MHz and the second lattice beam is shifted by -100 MHz. This ensures that the frequency beating is always far off from the critical range. In addition, the lattice beams have perpendicular polarizations relative to each other and thus there is no interference between them.

To protect the high-power fibers from damage which would occur if too much power is dumped in them, we set up an interlock system for each path to shut down the beam if the coupling efficiency of the fiber drops below a critical threshold. The interlock system measures the power before and after the fiber by collecting the transmitted light after a mirror on a photodiode (see e.g. Figure 3.7 and 3.8 for the pancake beam). Both signals are then processed by an ARDUINO micro-controller board which calculates the coupling efficiency and shuts down the rf-power in the AOM if the coupling efficiency drops below a certain threshold. The AOM then does not diffract anymore and the beam is just dumped before the fiber.

Preparing and aligning the pancake beams

In Figure 3.8 a sketch of all the optics on the experiment table is shown and one can see how we prepare the pancake beams. As mentioned earlier we need focal beam waists of $\omega_{0,\text{vert}} = 75 \mu\text{m}$ and $\omega_{0,\text{hor}} = 600 \mu\text{m}$ to create our pancake shaped potentials. Because the beam waist of a Gaussian beam transforms after a lens as $\omega'_0 \simeq \frac{\lambda \cdot f}{\pi \omega_0}$, this implies that we first have to expand the beam in the vertical direction in order to achieve the desired aspect ratio. The ellipticity of the beam is introduced using a cylindrical telescope consisting of a pair of $f = -75$ mm and $f = 500$ mm cylindrical lenses which lead to an aspect ratio of about 1:7 in vertical

direction which is slightly smaller than our initially planned aspect ratio of 1:8. To further clean the polarization of the beam, a thin film Brewster polarizer (Altechna: extinction ratio of $\sim 250 : 1$) has been inserted into the telescope as well. To create the two individual beams with our specially designed aluminium casing, we have to enter it under an angle of 45° relative to the table. Therefore we project the beam down from its initial height of about 10 cm to a height of about 2.5 cm using a periscope. When setting the periscope up, we took great care to ensure that no tilt of the beam is introduced, since this would distort our pancake potentials. The beam is then directed into the casing using a combination of mirrors which are mounted directly on the experiment table. The focusing of the beams is achieved by inserting a $f = 900$ mm spherical lens directly after the telescope and thus before the beam is split up. This should ensure that the focal point of both pancake beams is at the same position inside the chamber. After passing through the chamber, both beams are dumped behind a 2" dichroic¹¹ mirror.

To align the pancake trap, we relied on different methods. First of all, since there is an imaging along the pancake beam axis and a small part of the beams is reflected at the 2" dichroic mirror, we can directly image the pancake beams onto the camera. Thereby one can observe how the individual beams are moved with respect to each other. This method can also be used to adjust the focus of the $f = 900$ mm spherical lens to the position of the atoms. However, one has to keep in mind that the imaging setup is optimized for $\lambda = 671$ nm and thus the infrared pancake beams are not in focus on the camera.

After loading the pancake traps, one can overlap its position to that of the dipole trap by inserting a $\lambda/2$ -waveplate into one of the beam paths in the casing. This leads to perpendicular polarizations in the beams which turns off the interference fringes. The pancake traps then work simply as normal crossed beam dipole traps and one can overlap the pancake trap center easier to the center of the dipole trap. Thereby one ensures that one loads into the deepest fringes at the center when turning on the interference again.

3.2.2. Noise Characterization

Technical noise on the laser leads to intensity fluctuations of the laser output. If the frequency of these fluctuations coincides with the trap frequency, this can lead to heating of the atoms in the trap and thus a loss of atoms. Thus to estimate the effect of this noise induced heating, one has to characterize the noise spectrum of the laser. In this Section, we first summarize the theory of noise induced heating as derived in [Geh98]. Then our setup to measure the laser noise is described. At last, the results are presented and the effect of noise induced heating in our setup is estimated.

Noise induced heating

Technical noise leads to a fractional fluctuation $\epsilon(t) = \frac{I(t) - I_0}{I_0}$ of the laser intensity around a mean value I_0 . Since in a far-off resonant trap, the square of the trap

¹¹Reflective for 671 nm and transmissive for 1064 nm wavelength.

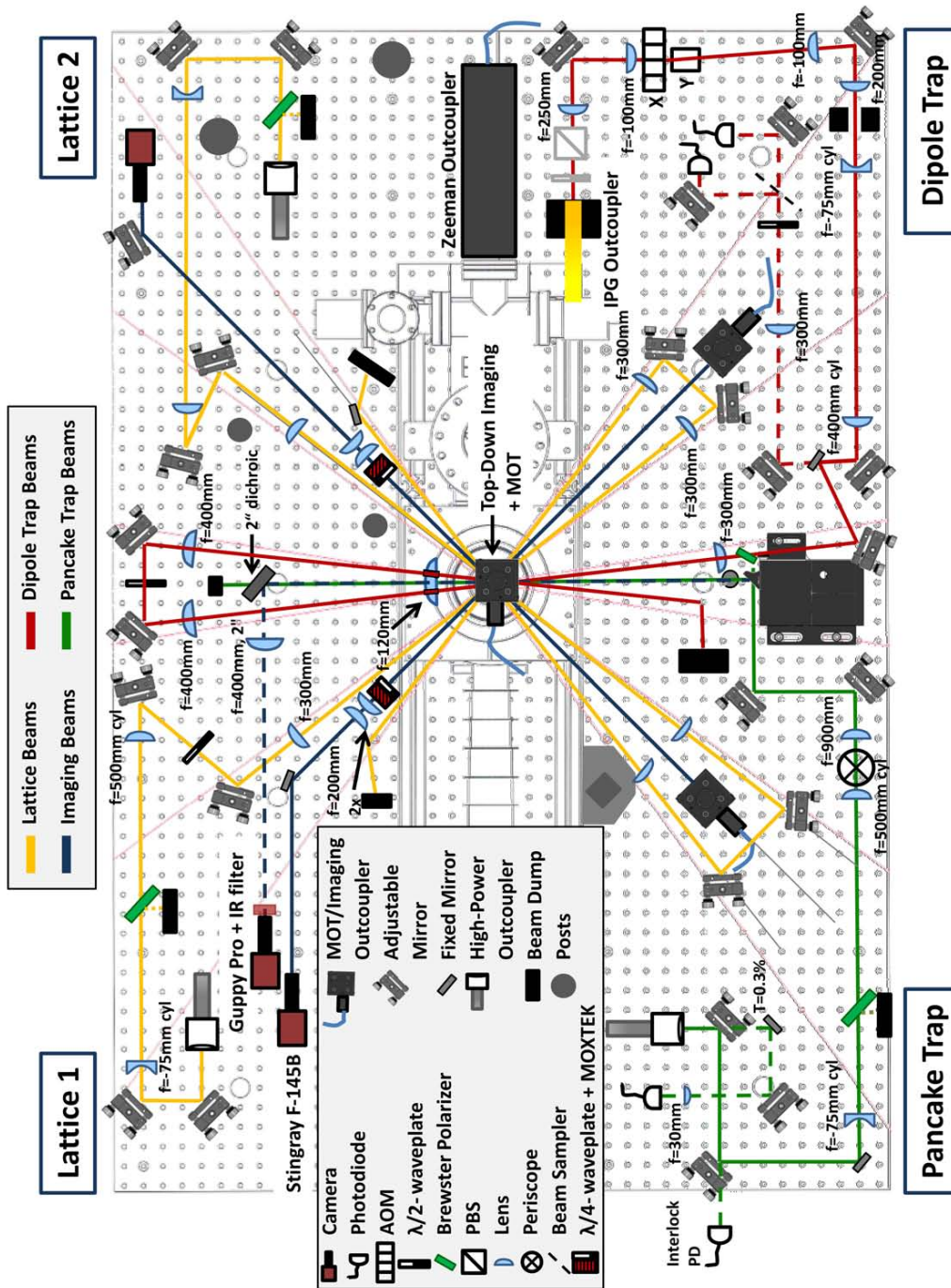


Figure 3.8.: Sketch of the experiment chamber including all optical beam paths. The MOT beams in horizontal direction go along the imaging paths emerging from the MOT/Imaging outcouplers. The optics in both lattice arms are identical and thus only the parts in lattice 1 are labeled. The gray shaded parts in the dipole trap path can be rotated into the beam path to dump power when aligning the beam. The posts are set up to support an additional breadboard for the optics of our new imaging objective [Ser11, Ber13] which will be inserted in the future.

frequencies ω_i^2 is proportional to the laser power and thus the intensity, intensity fluctuations lead to a fractional fluctuation of the spring constant of the harmonic trap. Thus the Hamiltonian for a trapped atom of mass m e.g. in the z -axis can be written as

$$H = \frac{p^2}{2m} + \frac{1}{2}m\omega_z^2 [1 + \epsilon(t)] z^2, \quad (3.4)$$

where ω_z is the mean trapping frequency and the time-dependent perturbation is given by

$$H'(t) = \frac{1}{2}\epsilon(t) m\omega_z^2 z^2. \quad (3.5)$$

Since the fractional fluctuation of the laser intensity is small, one can use first-order time-dependent perturbation theory to calculate the transition rate for an atom initially in state $|n\rangle$ of the trap to a state $|m \neq n\rangle$ within a time interval T . Because the perturbation is quadratic in its spatial coordinate, the perturbation does not change the parity of the states and thus in a harmonic oscillator these transitions can only occur in steps of $\pm 2\omega_z$. The transition rate $R_{n\pm 2 \leftarrow n}$ can then be calculated as

$$R_{n\pm 2 \leftarrow n} = \frac{\pi\omega_z^2}{16} S_k(2\omega_z) (n+1 \pm 1) (n \pm 1), \quad (3.6)$$

where S_k is the one-sided power spectrum defined below. Since the overlap of adjacent states with the same parity increases for larger trap levels n , the transition rates are not symmetric and the average energy increases over time. This also leads to the fact that the heating depends on the temperature since with increasing temperature, higher trap levels are occupied and hence the transition rates and therefore the heating increases.

In equation (3.6), $S_k(\omega)$ is the one-sided power spectrum of the fractional intensity fluctuation, defined for real-valued functions as

$$S_k(\omega) \equiv \frac{2}{\pi} \int_0^\infty d\tau \cos(\omega\tau) \langle \epsilon(t) \epsilon(t+\tau) \rangle, \quad (3.7)$$

where

$$\langle \epsilon(t) \epsilon(t+\tau) \rangle \equiv \frac{1}{T} \int_0^T dt \epsilon(t) \epsilon(t+\tau) \quad (3.8)$$

is the correlation function of the fractional fluctuation¹². The definition of the one-sided power spectrum also fulfills

$$\int_0^\infty d\omega S_k(\omega) = \langle \epsilon^2(t) \rangle \equiv \epsilon_0^2, \quad (3.9)$$

where ϵ_0 is the root-mean-square fractional intensity fluctuation.

From the transition rates in equation (3.6) it is then easy to calculate the time derivative $\langle \dot{E}_z(t) \rangle$ of the mean energy, assuming that initially the trapped atoms at

¹²In the derivation of the transition rates, it was assumed that the correlation time τ is much smaller than the time interval T , which allows one to extend the bounds of the integral over $d\tau$ to $\pm\infty$.

time t occupy the states $|n\rangle$ with probability $P(n, t)$

$$\begin{aligned}\langle \dot{E}_z(t) \rangle &= \sum_n P(n, t) 2\hbar\omega_z (R_{n+2\leftarrow n} - R_{n-2\leftarrow n}) \\ &= \frac{\pi}{2} \omega_z^2 S_k(2\omega) \langle E_z(t) \rangle \\ &= \Gamma_z \langle E_z(t) \rangle,\end{aligned}\tag{3.10}$$

where the mean energy is defined as $\langle E_z(t) \rangle = \sum_n P(n, t) (n + 1/2) \hbar\omega_z$.

Thus the energy increases exponentially with an energy e-folding time¹³ of $T_{e,z} = 1/\Gamma_z$.

Noise detection setup

To detect the one-sided power spectrum of the laser noise, we capture the laser light on a fast photodiode with a bandwidth of ~ 1 MHz. The light induces an electric current i_{laser} which is proportional¹⁴ to the detected optical power if the photodiode is operated in its linear regime. Therefore the fractional intensity fluctuation $\epsilon(t)$ translates into e.g. the measured fractional voltage fluctuation on an oscilloscope.

In our setup, we use a HAMAMATSU InGaAs G8370-81 SPL¹⁵ photodiode with an active area of 1 mm^2 . It has a linear response up to an incident power of $\sim 8 \text{ mW}$ and has a photo sensitivity of about 0.56 A/W at $1 \mu\text{m}$ wavelength. The circuit of the photodiode amplifier box is sketched in the Appendix B in Figure B.1. The signal is then read out using a TiePie HS3 Handyscope with a sample rate of up to 50 MHz .

To obtain the one-sided power spectrum, we record the y-t signal in AC and DC coupling with the maximal sample number of $N_s = 131067$ at a given sampling frequency f_s . By using AC coupling one increases the dynamic range to observe the fluctuations. The AC coupled signal corresponds to $I(t) - I_0$ whereas the mean of the DC coupled signal corresponds to I_0 and thus one obtains the fractional fluctuation $\epsilon(t) = V_{\text{AC}}/\bar{V}_{\text{DC}}$ from this measurement. Using the Wiener-Khinchin theorem [Wol] and the fact that $S_k(f) = 2\pi S_k(\omega)$, we can then calculate $S_k(f)$ from equation (3.7) using the Fourier transformation as

$$S_k(f) = 4 \int_0^\infty d\tau \cos(2\pi f\tau) \langle \epsilon(t) \epsilon(t + \tau) \rangle = 2 |\mathcal{F}\{\epsilon(t)\}|^2,\tag{3.11}$$

where $\mathcal{F}\{\epsilon(t)\} = \int_{-\infty}^\infty dt \epsilon(t) e^{-i2\pi ft}$ is defined as the Fourier transform and we replaced the angular frequency $\omega = 2\pi f$ with the frequency f .

Because we deal with a finite sample length, one has to use a discrete Fourier transformation (DFFT). The step size of the DFFT is $\Delta f = \frac{f_s}{N_s}$ and its unit is $\left[\frac{V^2}{\Delta f}\right]$. To normalize it, one has to divide by the sample number N_s^2 . Thus to obtain the correct power spectrum, one has to calculate

$$S_k(f) = \frac{\text{DFFT}(V_{\text{AC}}) \cdot \text{DFFT}^*(V_{\text{AC}})}{N_s \cdot f_s \cdot \bar{V}_{\text{DC}}^2}.\tag{3.12}$$

¹³Defined as the time which is needed to increase the energy by a factor of e.

¹⁴Given by the quantum efficiency $\eta(\lambda)$ of the photodiode.

¹⁵The cover glass is removed to avoid reflections.

From the one-sided power spectrum one can also directly infer the so-called relative intensity noise (RIN) of the laser which is simply given by

$$\text{RIN}_f = 10 \cdot \log_{10} S_k(f), \quad (3.13)$$

and is measured in units [dB/Hz]. The RIN is a widely used characterization of the laser noise and thus often provided in data sheets. Therefore by measuring the laser noise of the low-noise Mephisto seed laser and comparing our results to the manufacturer's data sheet, we could verify our detection method before measuring the noise of the NUFERN laser.

Test of the detection setup

To get any meaningful results, one has to ensure that one is not limited by other noise sources. Additional noise sources are dark currents in the photodiode box and the inherent quantized nature of light. Dark currents are caused by thermal excitations which lead to additional electron-hole pairs in the photodiode and thus add a dark current i_{th} . The photon flux varies with a poissonian distribution around a mean value [Sal07] and thus the detected power also fluctuates which leads to so-called shot-noise and limits the detectable RIN to [Dav97]

$$\text{RIN}_{\text{SNL}} = 10 \cdot \log_{10} \left(\frac{2 \cdot h\nu}{\eta \bar{P}} \right). \quad (3.14)$$

Thus in the measurement of the noise we make sure to have incident powers on the order of 1 mW on the photodiode where the photodiode is still linear and the output voltage on the oscilloscope is large without saturating it. This corresponds to a shot-noise limit of about -152 dB/Hz and a photodiode background noise on the same order which is sufficiently low to measure the expected laser noise. We measured both the relative intensity noise of the Mephisto seed with the active noise eater on and off, as well as the background noise of the photodiode when there was no light present. In Figure 3.9 a), our results for these measurements are shown. When comparing it to the specification of the manufacturer in b), one can see that the characteristic profiles are in good agreement, including the position, width and relative height of the relaxation peak when the noise eater is off and the crossing of the noise levels with noise eater on/off above 1 MHz. Above 1 MHz one can also see that we are limited in our detection by the background photodiode noise. However, the trap frequencies in the experiment are on the order of at most 400 kHz and thus this does not affect us since for the noise induced heating higher order excitations $|i\rangle \rightarrow |i + 2n\rangle$ with $n > 1$ are negligible due to the small overlap of the respective wave functions.

When comparing the absolute RIN of both measurements, one sees that our measured curves have a constant offset of ~ 10 dB/Hz compared to the specified curves. Thus either the performance of the laser is worse due to different conditions or parameters or there is a systematic difference in our definition of the noise or detection method. In the worst case, we overestimate the noise level and therefore we can take all results we obtain with these noise measurements as a lower bound of our laser

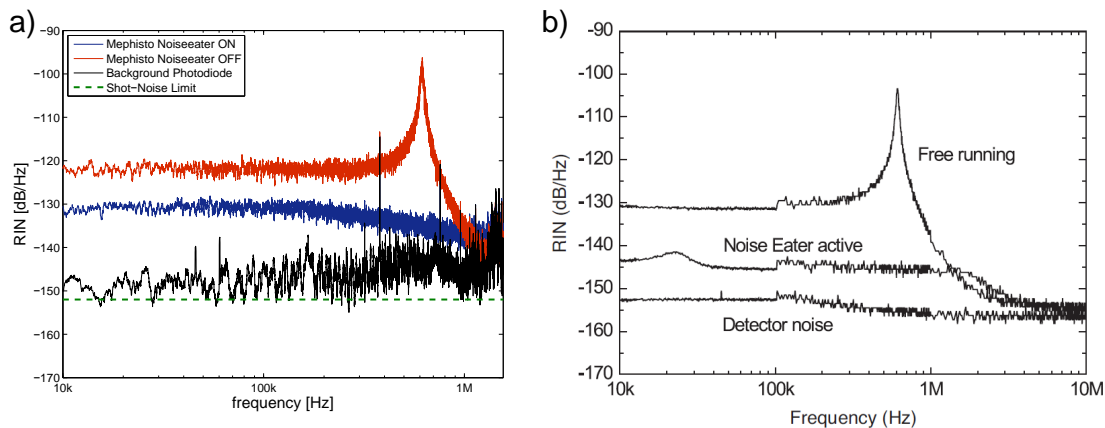


Figure 3.9.: **RIN measurement of the Mephisto noise.** a) Experimental data from our setup with the noise eater ON (blue) and OFF (red). The sampling frequency was $f_s = 3.125$ MHz and a moving average was taken over a span of 500 Hz to smooth the curves. The green-dotted line shows the shot-noise limited RIN and the black data is the background noise from the photodiode. b) Specifications from the Mephisto datasheet [Mep].

performance. In addition, conclusions about relative noise levels are still valid since the relative difference in our measurement agrees with the one of the data sheet.

With the active noise eater on, the Mephisto has an almost constant RIN of ~ -135 dB/Hz for frequencies up to several hundred kHz. In the vertical axis of the pancake traps we will have typical trap frequencies of about 10 kHz and in the 2D lattice we will have trap frequencies on the order of 300 kHz. Putting these numbers into the energy e-folding time T_e

$$T_e = \frac{1}{\pi^2 f^2 S_k(2f)} \quad (3.15)$$

derived from equation (3.10) results in times of $T_{e,\text{pancake}} \approx 32000$ s and $T_{e,\text{lattice}} \approx 36$ s respectively. Thus the laser noise of the Mephisto seed will not limit us when conducting experiments in the optical lattices which will be on the timescale of a few seconds.

Measurement of the NUFERN noise

To characterize the noise which the NUFERN amplifier creates additionally to the Mephisto operating with active noise eater on, we measured the laser noise of the amplified beam both on the breadboard side before the high-power fiber and on the experiment side (see Appendix B, Figure B.2). The first thing we looked at is how much noise the NUFERN adds in dependence of the pump current. In Figure 3.10 the measurement of the noise on the breadboard side is shown for two different pump currents $I_p = 0$ A, the lowest possible pump current¹⁶ corresponding to a laser

¹⁶Note that this is just the set value of the NUFERN control but there is already pumping present.

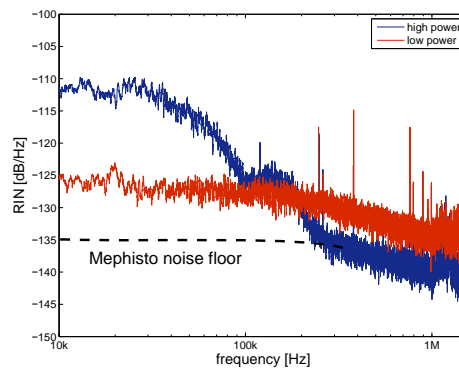


Figure 3.10.: **RIN measurement of the NUFERN noise at low and high pump power.** The sampling frequency was $f_s = 3.125$ MHz and a moving average was taken over a span of 500 Hz to smooth the curves. The NUFERN was free running at powers of $P = 1$ W (red) and $P = 25$ W (blue). The noise is increased by approximately 10 dB/Hz for low laser powers and by up to 25 dB/Hz for high laser powers. At high laser powers, the noise converges towards the Mephisto noise floor at frequencies above 200 kHz.

output of ≈ 1 W and $I_p = 30$ A, a pump current corresponding to a laser output of ≈ 25 W. Already at the lowest pump current, the noise is increased by ~ 10 dB/Hz throughout the spectrum. For larger pump currents, the noise in the region below 200 kHz is increased further by up to 25 dB/Hz compared to the Mephisto noise floor, whereas for higher frequencies the NUFERN noise converges towards the Mephisto noise floor.

The next thing we checked is if the coupling through the high-power fiber changes the noise characteristics. Therefore we measured the noise at high laser power of $P = 25$ W on both sides of the fiber. As one can see in Appendix B Figure B.3, the noise spectrum is not altered by the fiber, except for larger spikes emerging at frequencies above 200 kHz with a width on the order of 1 kHz. We confirmed that these spikes are due to the photodiode background noise and stem from a ground loop between the photodiode box - grounded on the optical table - and the TiePie which is grounded via the power supply of the laptop (see Appendix B Figure B.4). Thus to get rid of these in future measurements, one should not ground the TiePie Handyscope.

In the experiment, we stabilize the power in the pancake beam using a digital PID-feedback control implemented in the ADwin experiment control. It has a sampling rate of 100 kHz and the power is controlled via the intensity of the diffracted light of an AOM. Therefore we measured the noise of the NUFERN running at high power on the experiment side both with the power stabilization turned on and off (free running). The results can be seen in Figure 3.11. The most prominent feature is the emergence of the so-called servo bump [Wei11] at about 40 kHz. There the feedback loop has a negative feedback which leads to an increased sensitivity, effectively increasing the noise around these frequencies. The height of the servo bump depends on the settings of the PID parameters and thus also depends on

3. Experimental Setup

the incoming power. Above 100 kHz, additional peaks appear albeit at a lower noise level (see panel b)). Because the servo bump appears at frequencies close to the trap frequencies which we expect for the vertical direction of the pancakes, one can think about implementing a faster PID control in the future with a larger bandwidth, thus shifting the servo bump to higher frequencies. Ultimately, the limit for such PID control is given by the bandwidth of the AOM. With a beam diameter of $d = 1$ mm and the sound velocity of $v = 4.2$ mm/ μ m in the crystal, the response time of the AOM is $t_r = d/v = 250$ ns. This limits the bandwidth to about 1 MHz. Therefore the servo bump would be closer to the lattice trap frequencies at about 300 kHz which could impose problems since the e-folding time T_e scales as $1/f_{\text{trap}}^2$ and thus the noise becomes more important. Hence we decided to keep the current setup. In graph a) one can see that at frequencies below 20 kHz the power stabilization

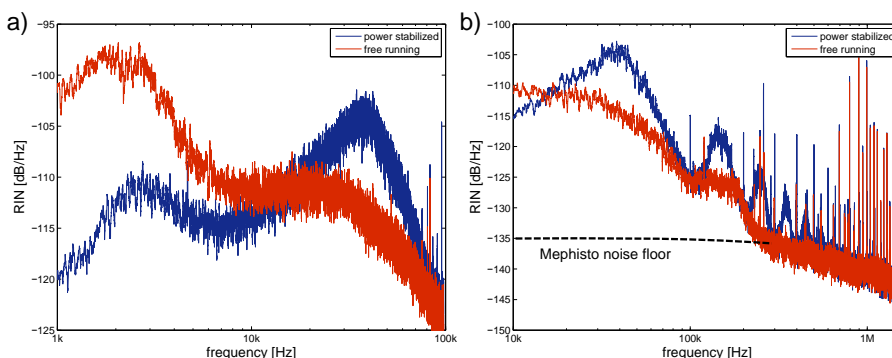


Figure 3.11.: **RIN measurement of the NUFERN noise with power stabilization turned on/off.** a) Sampling frequency $f_s = 196.315$ kHz and moving average over a span of 31 Hz. b) Sampling frequency $f_s = 3.125$ MHz and moving average over a span of 500 Hz. The red data points correspond to the free running case and the blue data points to the case when the power was stabilized using the digital PID-feedback. The NUFERN was running at $P = 25$ W.

suppresses the noise by up to ~ 18 dB/Hz and hence in this regime the power stabilized laser outperforms the free running laser. The calculation of the e-folding time T_e at a given trap frequency f_{trap} (see equation (3.15)) depends however on the one-sided power spectrum $S_k(2f_{\text{trap}})$ and thus the e-folding time T_e of the power stabilized laser is only improved up to ~ 10 kHz. In Figure 3.12 the derived e-folding times from the noise measurement are shown. At small frequencies on the order of a few kHz, T_e is larger than 100s and thus noise induced heating is not a problem on the timescales of our experiments which last usually not more than 10s. T_e has its minimum of about 10s at trapping frequencies of about 20 kHz. Above this critical range, T_e improves again due to the decreasing laser noise although T_e scales with the trapping frequency f_{trap} as $1/f_{\text{trap}}^2$. Therefore the most critical range for noise induced heating in the trap is in this regime below 20 kHz. Since we also expect the trap frequency of the vertical axis in the pancake trap to be on the order of 10kHz, the increased noise in this regime could limit the lifetime of the atoms in the pancakes. To estimate the effect of this exponential noise induced heating, one

has to compare it with the linear heating due to the photon scattering, as described by equation (2.52). The time Δt at which the noise induced heating dominates the photon scattering induced heating ΔT_{sc} can be calculated as $\Delta T_{\text{sc}} = T_0 (e^{\Delta t/T_e} - 1)$. Assuming an initial temperature of $T_0 = 300$ nK in the pancake trap and a total beam power of 4 W, we expect trap frequencies of about 10 kHz in vertical direction in the pancake trap. A lower bound for the e-folding time at these frequencies is about $T_{e,\text{min}} = 30$ s. Putting these parameters into the equation results in a time $\Delta t \approx 23$ s. Therefore on the timescales of our experiments noise induced heating should be negligible if the temperature of the atoms in the crossed beam dipole trap is on the order or below 300 nK before the transfer into the pancake trap. Thus we expect not to be limited by laser noise in the experiment.

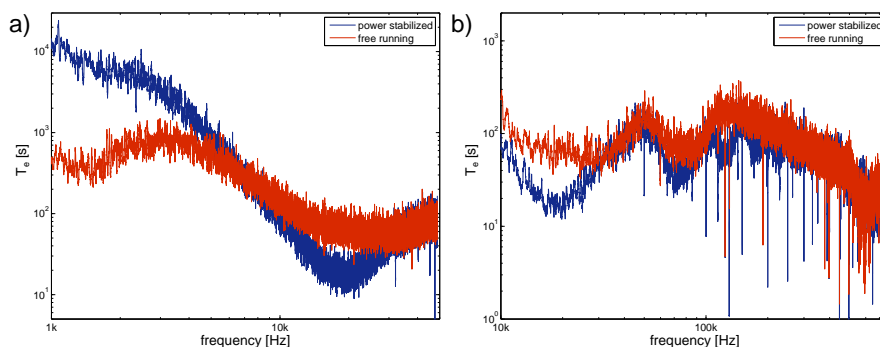


Figure 3.12.: **Energy e-folding time constant for the NUFERN.** a) Sampling frequency $f_s = 196.315$ kHz and moving average over a span of 31 Hz. b) Sampling frequency $f_s = 3.125$ MHz and moving average over a span of 500 Hz. The red data points correspond to the free running case and the blue data points to the case when the power was stabilized using the digital PID-feedback. The NUFERN was running at $P = 25$ W. The spikes in panel b) are due to background noise in the photodiode and thus do not contribute to the heating rate.

3.3. Radio-Frequency Setup

The starting point for our experiments is always a spin mixture of ${}^6\text{Li}$ atoms in the hyperfine states $|1\rangle$ and $|2\rangle$ in the dipole trap. Therefore to perform experiments with a three-component mixture, we need to transfer atoms into the initially unoccupied hyperfine state $|3\rangle$. This can be done by applying a radio-frequency (rf) pulse at the right transition frequency and pulse length which is described in detail in Section 4.5.1.

To create the rf-pulses, an rf-antenna has been installed directly into the vacuum chamber such that it is positioned close to the atoms. Thereby one obtains large Rabi-frequencies which allows us to do these transfers very fast. To prevent the coil from overheating in the vacuum chamber, an interlock system has been inserted.

More details on the optimization of the rf-antenna can be found in a recent Bachelor thesis [Heu11] and its application in the experiment can be found in [Boh12].

3.4. Imaging

To examine the atoms in our traps, we perform both absorption or fluorescence imaging along different axes. Fluorescence imaging is done by capturing the re-emitted photons from the MOT on a CCD camera with an appropriate optical imaging system. From the captured solid angle, the photon scattering rate and the camera properties one can then infer e.g. the atom number in the MOT.

To image the atoms inside optical traps, one relies on absorption imaging (see Figure 3.13) since the atoms do not scatter the far off-resonant trapping light¹⁷. The idea of absorption imaging is to apply a short pulse of resonant light to the atoms and capture the transmitted light on a camera. Since the atoms scatter the light, there will be a dark spot (shadow) on the CCD cameras at the location of the atoms. By taking a second picture without any atoms and taking the ratio of the intensities on the two images, one can infer the column density n_{2D} along the line of imaging. Because the ratio of two pictures is used, only static fringes on the imaging light do not have any effect on the SNR. To avoid that any vibrations add non-static fringes, we switch off our magnetic Feshbach coils only after the second picture has been taken. Since each scattering event gives a recoil to the atom, the applied pulse has to be short to not wash out any structure information. This is especially true for ${}^6\text{Li}$, since it has a small mass and therefore a high recoil velocity. Hence we limit the duration of our imaging pulses to $10\ \mu\text{s}$ or less.

More information on imaging techniques in ultracold gases can be found in [Ket99] or in [Lom08] for the special case of ${}^6\text{Li}$.

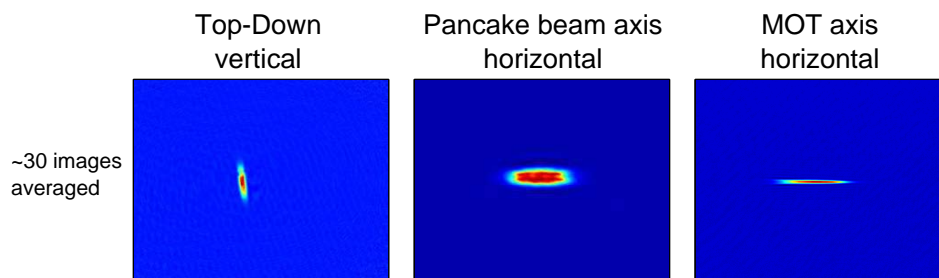


Figure 3.13.: **Absorption images of the dipole trap from all installed cameras.** The images represent averages over ~ 30 individual absorption images.

¹⁷In principle it is possible to flash the atoms with a short resonant light pulse and capture the scattered photons, however the signal-to-noise (SNR) ratio for dense clouds is worse than in absorption imaging.

Top-Down axis

To observe the atomic profile in the horizontal plane, we use an imaging axis setup parallel to the vertical MOT beam. The outcoupler for the imaging beam is mounted on top of the octagonal experiment chamber (see Figure 3.8) and uses the design as explained in Figure 3.5 to overlap the imaging beam with the MOT beam. After the beams pass the experiment chamber they are separated using a combination of a $\lambda/4$ -waveplate and a MOXTEK reflective polarizer. The imaging light is then directed onto an AVT Stingray F-125B camera with a 2" mirror below the experiment chamber. The camera has a pixel size of $3.75 \mu\text{m} \times 3.75 \mu\text{m}$ and the imaging system consists of two $f = 80 \text{ mm}$ achromatic lenses resulting in a magnification of $M \approx 1$ with an uncertainty on the order of a few %. The lens has a numerical aperture $\text{NA} \approx 0.14$ limiting the maximal achievable resolution to $d_{\text{min}} = 2.9 \mu\text{m}$.

In the near future, we will change this imaging to implement a new objective with a high numerical aperture ($\text{NA} \approx 0.6$). A copy of this objective is has been installed and is currently tested in the other experiment in our group [Ber13]. The achievable resolution for this new objective at a wavelength of $\lambda = 671 \text{ nm}$ has been measured to be at least better than $d_{\text{min}}^{\text{exp}} \leq 1.01 \mu\text{m}$ in comparison to the planned resolution of $d_{\text{min}}^{\text{theo}} = 682 \text{ nm}$. However the estimate of the resolution was done measuring the point-spread function of a pinhole with a diameter of 650 nm and thus the achievable resolution is probably even smaller. This improved resolution will be an important factor when investigating the 2D optical lattice.

Pancake beam axis horizontal

To image the atoms along the long axis of the optical dipole trap, we inserted an imaging axis parallel to the pancake beams. The outcoupler is mounted vertically on the outer wall of the aluminium casing for the pancake trap. A mirror which is mounted on the casing as well then directs the imaging beam into the experiment chamber. To obtain a high numerical aperture, the objective ($f = 120 \text{ mm}$) is directly mounted on the viewport (see Figure 3.8). Because the dipole trap beams pass through this viewport as well, we cut two elliptical holes into the lens to let them pass unaffected. In vertical direction, the objective has a numerical aperture of $N_{\text{vert}} \approx 0.15$ and hence a theoretical maximal achievable resolution of $d_{\text{min}}^{\text{vert}} = 2.8 \mu\text{m}$. The achievable resolution in horizontal direction is slightly lower since the holes in the lens introduce perturbations and thus limit the usable lens size. We tested the objective in an external test setup and confirmed a resolution of at least $d_{\text{min}}^{\text{vert,exp}} = 3.5 \mu\text{m}$ by using both a 1951 USAF test target and a pinhole. In theory this should barely enable us to directly resolve the individual pancakes, since they have a spacing of about $4 \mu\text{m}$. But this is only true for very low atom numbers because the depth of focus puts a serious limitation on the resolution. When comparing the depth of focus of about $z_{\text{DOF}} = \frac{4\lambda}{\text{NA}^2} \approx 93 \mu\text{m}$ to the size of the atom cloud in the pancakes of about $300 \mu\text{m}$, one can see that blurring will decrease the achievable resolution. Thus this limitation can only be overcome for very low atom numbers where the cloud size becomes smaller than z_{DOF} . But for such low number of atoms the signal-to-noise ratio (SNR) is very bad and therefore we have not been able to directly

resolve the pancakes.

After passing through the experiment chamber, the beam is reflected by a 2" dichroic mirror and focused onto the camera with a $f = 400$ mm, 2" lens. The dichroic mirror is used to suppress any reflections from the IR pancake beams. Since there is quite a lot power to begin with in these beams, an additional IR filter is also placed directly in front of the camera. The camera itself is a AVT Guppy Pro F-125B with a pixel size of $3.75 \mu\text{m} \times 3.75 \mu\text{m}$ and the imaging system has a magnification of $M \approx 3.3$. Since the objective for this setup is directly mounted on the viewport of the experimental chamber and its relative distance to the atoms cannot be tuned easily, we estimate an error on the order of 10% for the magnification.

MOT axis horizontal

When looking along the dipole trap axis, one is not able to observe how well the incoming and reflected dipole trap beam are overlapped in vertical direction. Therefore, we set up another imaging along one of the MOT axis (see Figure 3.8). The splitting of the MOT and imaging beam is done as described in Figure 3.5. The imaging system uses two $f = 200$ mm lenses resulting in a magnification of $M \approx 2$ with an uncertainty on the order of a few %. The camera is an AVT Stingray F-145B with a pixel size of $6.45 \mu\text{m} \times 6.45 \mu\text{m}$. So far we implemented this imaging only in one of the MOT arms, but we are planning to implement one in the other MOT axis soon as well.

4. Characterization of the Pancake Trap

In this chapter the different measurements we performed to characterize the pancake trap are described in detail. Some of these measurements were done before and some after we moved the experiment from the MPIK to the PI in December of 2012. Because we had to realign the trap again after the move, some properties of the pancake trap may have changed slightly.

First in Section 4.1 we describe the transfer of the atoms into the pancake trap after evaporatively cooling them in the dipole trap. Then in Section 4.2 the measurement of the pancake trap frequencies which characterize the strength of the confinement in the different axes is described. Subsequently in Section 4.3 the measurement of the lifetime of the atoms in the pancake trap is shown. Atom losses lead to so-called hole heating and hence a long lifetime is crucial for the experiments we want to perform. These measurements were all performed after we moved the experiment to our new labs.

Already before the move, we investigated the diffraction of a molecular BEC on the pulsed pancake trap to get an estimate of the pancake depth. Therefore in Section 4.4, we first describe the basics of this so-called Kapitza-Dirac diffraction before explaining the experimental sequence and showing our results. To investigate the atom population in each pancake and obtain a method to count how many of the pancakes we load, we used a radio-frequency (rf) tomographic measurement. In Section 4.5 we first give a short summary on the basics of rf-transitions and the calibration of our rf-system. Then the measurement is explained and the results are presented in detail. From this measurement also the short and long term positional stability of the pancake trap is estimated. Finally in Section 4.6 our so far achieved progress towards loading a single pancake is summarized shortly.

4.1. Transfer into the Pancake Trap

To transfer the atoms into the stack of pancake traps, one slowly ramps down the power in the dipole trap while simultaneously ramping up the power in the pancake trap to the desired trap depth. Depending on the initial vertical extension of the cloud in the dipole trap, the atoms are then transferred into several layers of the pancake trap. Since the separation between these layers is on the order of $4\ \mu\text{m}$, the atoms do not tunnel between these layers at normal trap depths. In Figure 4.1 such a transfer is shown for a mBEC at a magnetic field of $B = 795\ \text{G}$. One can clearly see the difference between the surfboard shaped potential of the dipole trap and the pancake shaped potential of the pancake trap. From the size of the

cloud in vertical direction we can see that we do not load the atoms into a single pancake but into several. However this cannot be directly resolved by our absorption imaging and thus we do not see this structure in the absorption image of the cloud. Therefore we used other techniques to make the distribution of the atoms in the individuals layers visible (see Section 4.5). In the top-down imaging one can see

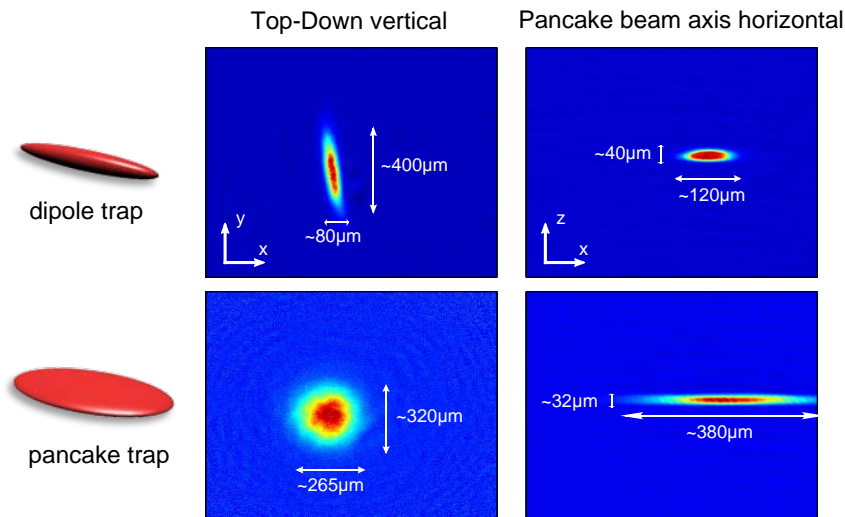


Figure 4.1.: **Transfer from the dipole trap into a stack of pancakes.** The images represent averages over ~ 30 individual absorption images. The widths d are estimated from Gaussian fits as $d = 4\sigma$. In the upper row one can see nicely the characteristic surfboard shape of the crossed beam trap due to the elliptical beam. In the lower row the pancake trap is shown and one can see from the top-down imaging that the trap is almost round with an aspect ratio of 1:1.2. The aspect ratio from the front cannot be that easily estimated since the vertical size of the cloud is much larger than a single pancake. The different widths in the x-axis between the two cameras stem from uncertainties in the magnification calibration and imaging angles.

that our pancakes are not perfectly round but are slightly elliptical with an aspect ratio of about 1:1.2 which should manifest itself in the trap frequencies as well. The size of the cloud differs for the two cameras, which is due to uncertainties in the magnification calibration of the imaging systems and also because of imaging angles.

4.2. Trap Frequencies in the Pancake Trap

Optical traps can be described in a good approximation by a harmonic potential in three dimensions with distinctive trap frequencies $\omega_i = 2\pi f_i$ which scale with the square-root of the beam power (see equation (2.42)). To measure these trap frequencies, one can do the following: after the transfer of a two-component mixture of atoms into the pancakes, the pancake potential is suddenly ramped up to twice

its value¹. This excites a breathing mode - a collective motion of the atoms inside the trap - where the width of the cloud oscillates at twice the trap frequency. Thus by imaging the cloud after different hold times, one can make these oscillations visible and obtain the trap frequencies by looking at the width of the cloud from different axes. Since interaction effects would lead to a damping of the oscillation, the magnetic field is ramped close to the zero-crossing of the scattering length at $B \approx 527$ G immediately before the potential jump. However a damping of the oscillations can still be observed since inhomogeneous magnetic field gradients and curvatures lead to a dephasing of the atoms.

In Figure 4.2 such a measurement is shown for each of the pancake trap axes at a pancake trap depth of $3.5 V_{\text{contr}}$ which corresponds to a total beam power of 2.35 W. In the horizontal plane, the x-axis is defined along the Zeeman slower whereas the y-axis is defined along the pancake beams. One can see that the horizontal trap frequencies are almost identical and much smaller than the vertical trap frequency, hence the trap has a large aspect ratio as planned. Since the confinement in the vertical axis is much stronger, the images for the evolution of the cloud in the z-axis were taken after a short time-of-flight, to make the fitting easier. We did this

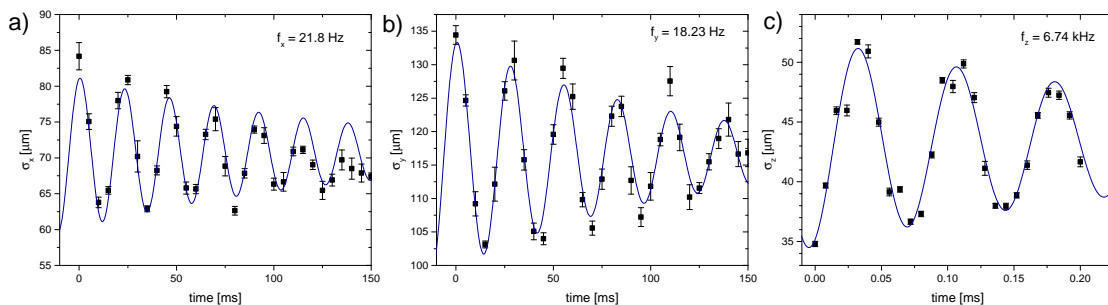


Figure 4.2.: **Measurement of the trap frequencies for a given trap depth.**

The Gaussian width σ is plotted versus the time the atoms oscillated in the trap. a) Horizontal trap frequency along the Zeeman slower axis. b) Horizontal trap frequency along the pancake beam axis. c) Vertical trap frequency. The fits are damped sine functions and the trap frequencies correspond to half the oscillation frequencies. The trap depth was set to $3.5 V_{\text{contr}}$, corresponding to a total beam power of 2.35 W.

measurement at different trap depths and thus we can plot the evolution of the trap frequencies as a function of the trap depth (see Figure 4.3). The fits are square-root laws of the form $f_{\text{trap}} = \sqrt{\text{const}^2 P^2 \pm f_{\text{mag}}^2(B)}$, where the additional term describes the confinement due to the magnetic field saddle produced by the Feshbach coils. The magnetic field saddle leads to a weak magnetic confinement in the horizontal plane and a weak anti-confinement in the vertical axis on the order of a few Hz. Since the vertical optical confinement is much stronger, the anti-confinement in the vertical direction can be neglected. At a field of $B = 527$ G, the magnetic confinement in the horizontal plane has a trap frequency of about $f_{\text{mag}} = 4$ Hz.

¹When the potential jump is too large, the atoms probe the potential further from the center where the harmonic approximation is not good anymore.

From these measurements one can also calculate the aspect ratio of our trap. In the horizontal plane we have an aspect ratio $f_x/f_y \approx 1.2$ and thus the pancakes are almost round as planned. Overall the measured aspect ratio is $\omega_x : \omega_y : \omega_z \approx 1.2 : 1 : 357$. The pancake traps have a planned vertical waist on the order of $2 \mu\text{m}$ and a horizontal waist of $600 \mu\text{m}$. Since the trap frequencies ω_i scale inversely to the beam waists w_i (see equation (2.42)), this results in a planned aspect ratio of $\omega_y : \omega_x : \omega_z \approx 1 : 1 : 300$ which is in good agreement to our measurement. Although the aspect ratio is as expected, our measured trap frequencies are systematically a factor 1.8 smaller than we would expect from a calculation, which indicates that the trap depth is not as deep as planned. It has not been thoroughly investigated so far if this deviation stems from an error in the calculation or some variation from the planned beam geometries, however the achievable trap depths should be sufficient to reach the regimes we planned for.

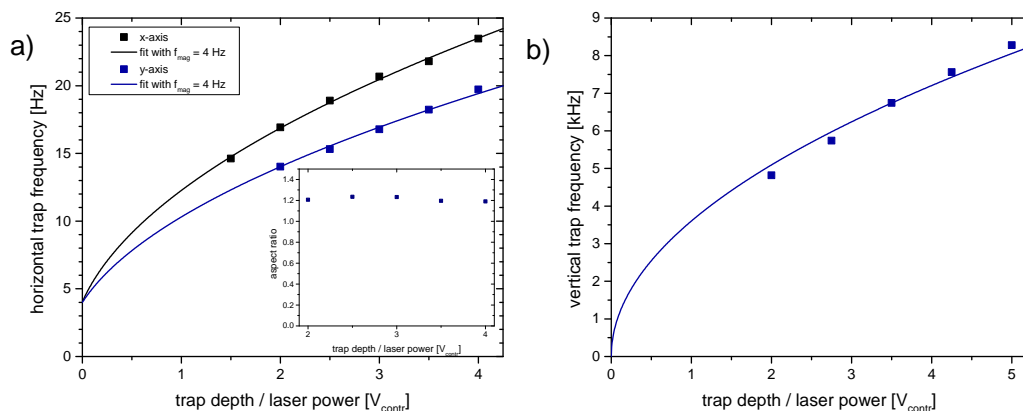


Figure 4.3.: **Pancake trap frequencies in dependence of the trap depth.**

The trap frequencies are plotted versus the trap depth. a) Horizontal trap frequencies. The inlay shows the aspect ratio f_x/f_y . b) Vertical trap frequency. The fits in a) are given by square-root laws $f_{\text{trap}} = \sqrt{\text{const}^2 P^2 + f_{\text{mag}}^2 (B = 527 \text{ G})}$ whereas in b) the magnetic anti-confinement is neglected and the fit is simply $f_{\text{trap}} = \sqrt{\text{const}^2 P^2}$.

4.3. Lifetime in the Pancake Trap

To measure the lifetime of the atoms in the pancake trap, we did a low-field evaporation in the dipole trap to produce a degenerate Fermi gas with about 100,000 atoms in each spin state at a temperature of $T \approx 240 \text{ nK}$, corresponding to $T/T_F \approx 0.44$. As explained in Section 3.2.2, we expect the lifetime not to be limited by noise induced heating in the trap at these low temperatures.

Before transferring the atoms into the pancakes, we switched off the interaction between the spin states by ramping to a magnetic field $B \approx 527 \text{ G}$ where the scattering length has its zero-crossing. Therefore one has a non-interacting Fermi gas and no further evaporation or thermalization should affect the lifetime measurement.

After the transfer, we held the atoms inside the pancake traps for varying hold times between 0.1 s and 20.1 s and measured the atom number in one spin state using absorption imaging. To check the influence of the pancake depth onto the lifetime, we did this measurement for varying trap depths between $1.5 V_{\text{contr}}$ and $5.5 V_{\text{contr}}$. As one can see in Figure 4.4 a), the decay can be fitted well using an exponential decay $N(t) = N_0 \cdot e^{-\frac{t}{\tau}}$ where τ is the lifetime and N_0 is the initial number of atoms and thus the decay is dominated by one-body loss processes. These are either scattering of the atoms with the background gas or with the photons from the far off-resonant optical trap. In Figure 4.4 b) the lifetime is plotted versus the trap depth which is

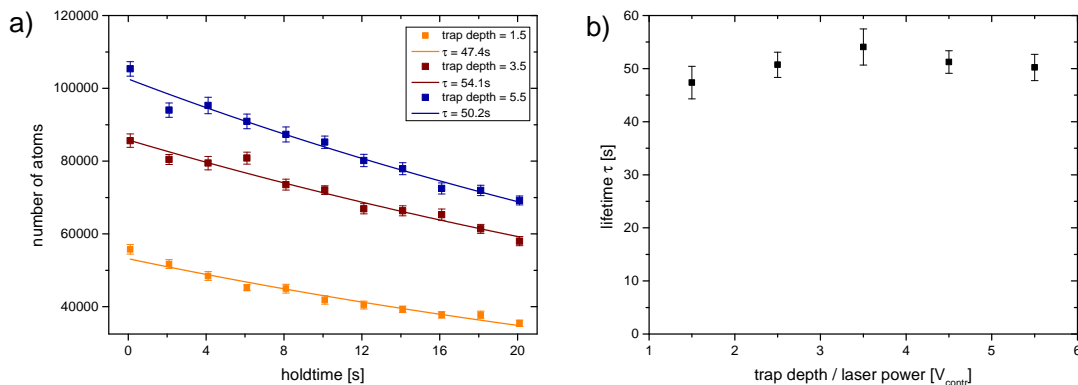


Figure 4.4.: **Lifetime measurement for the pancake trap.** a) Atom number versus hold time for varying trap depths. The lines are exponential decays fitted to the data. b) Lifetime τ in dependence of the trap depth which is proportional to the laser power. The lifetime is ~ 50 s and there seems to be no strong dependence of the lifetime on the trap depth.

proportional to the laser power. The lifetime seems to have no strong dependence on the laser power and thus already at small trap depths of $V_0 = 1.5 V_{\text{contr}}$ corresponding to a total pancake beam power of 1 W, the lifetime is $\tau \approx 47$ s and hence much larger than the time scale of our experiments (~ 1 s). The lifetime then reaches its maximum of $\tau \approx 54$ s at a trap depth of $V_0 \approx 3.5 V_{\text{contr}}$ before slightly decreasing again. However the deviations in lifetime are small and are within the error of the fit.

For a degenerate Fermi gas with $T/T_F < 1$, one also has to consider the effect of hole heating. Each loss process kicks out an atom and thus leaves a hole in the Fermi distribution. In subsequent collisions, a fermion can then relax into this unoccupied state which leads to an excitation of another fermion into a higher trap level and thus increases the temperature. This is a severe problem since the only cooling mechanism, evaporative cooling, is highly suppressed at these temperatures due to Pauli blocking [Hol00, DeM01]. The effect of hole heating in a homogeneous Fermi mixture was calculated by E. Timmermans [Tim01] to be

$$\frac{T}{T_F} = \left(\frac{T_0}{T_{F,0}} \right) \left(\frac{N}{N_0} \right)^{-1/3} \times \sqrt{1 + \frac{12}{5\pi^2} \left[\frac{T_{F,0}}{T_0} \right]^2 \left[1 - \left(\frac{N}{N_0} \right)^{2/3} \right]}, \quad (4.1)$$

where $T_0/T_{F,0}$ is the initial temperature in units of the Fermi temperature and the fraction of remaining particles N/N_0 can be substituted by $\exp(-t/\tau)$ if the loss is predominantly caused by background and photon scattering. For short time scales equation (4.1) can be approximated by

$$\frac{T}{T_F} = \frac{T_0}{T_{F,0}} \sqrt{1 + \frac{3t}{\tau_2}} \quad \text{with} \quad \tau_2 = \left(\frac{15\pi^2}{8} \right) \left[\frac{T_0}{T_{F,0}} \right]^2 \tau \quad (4.2)$$

being the temperature doubling time which gives the time scale after which the initial temperature in the trap has doubled. Thus hole heating gets more severe with decreasing temperature but can be suppressed by having long lifetimes τ in the trap.

Therefore, even if one would be able to load a Fermi gas with $T/T_F \ll 1$ into the lattice, in our setup with an average lifetime $\tau \approx 50$ s the temperature would already reach $0.1T_F$ after a time scale $\Delta t \sim 0.07\tau \approx 3$ s and $0.2T_F$ after a time scale $\Delta t \sim 0.2\tau \approx 10$ s respectively.

In the Fermi-Hubbard model for an optical lattice, the timescales are given by the tunneling strength J between adjacent lattice sites and the on-site interaction energy U . For our planned values these timescales are well above 100 Hz and thus we should be able to investigate the physics in the lattice before the heating becomes too severe.

However, cooling atomic clouds down to initial temperatures below even $0.05T_F$ is very challenging and thus these time scales represent only upper bounds. Furthermore, ramping the lattice up is not a perfectly adiabatic process which can lead to further heating. Thus one has to find a trade-off between a lattice ramp time which is slow enough to not introduce too much heating but fast enough in order not to be limited by hole heating.

This makes it experimentally very challenging to observe effects which only form below a certain temperature threshold like e.g. the emergence of an antiferromagnetic (AFM) ground state or the formation of superfluid Cooper pairs. To realize e.g. the AFM phase in an optical lattice experiment, one expects that the required temperatures are below $T/T_F < 0.04$ [McK11], which is a reason it has not been observed so far experimentally.

4.4. Making the Pancakes visible: Kapitza-Dirac Diffraction

Imaging the individual pancakes from the side is made difficult due to their high anisotropy. Resolving individual pancakes requires a resolution which is much better than the pancake spacing $d_{PC} \approx 4 \mu\text{m}$, however an imaging system satisfying this condition would have a depth of focus on the order of $90 \mu\text{m}$ which is with feasible atom numbers much smaller than the horizontal extension of the atoms in the pancake potentials of about $300 \mu\text{m}$. Hence blurring would occur which would smear out the structure. Thus only at very low atom numbers when the atoms are confined close to the pancake center, a direct observation of the pancake structure would be

possible. But at these low atom numbers the signal-to-noise ratio (SNR) is quite bad and thus a direct detection of the pancake structure is challenging. In our setup we are also limited in the achievable vertical resolution by the side window and thus our resolution is just barely below the pancake spacing, increasing the difficulty of a direct observation even more.

To still be able to monitor and evaluate the pancake trap we had to find another way to make the pancake potentials visible. An established method for this is to switch on the periodic potential for a short time, thus diffracting the atomic cloud on this standing wave. This leads to a discrete momentum transfer on the cloud which is made visible in time-of-flight (TOF) imaging by several separated clouds. From the relative atom numbers of these separated clouds and the distance between them, one can then infer the lattice spacing d_l and the trap depth V_0 .

In the following, the theory of diffraction on a pulsed potential is summarized and subsequently our application of this method to characterize our pancake traps is presented.

4.4.1. Basics of Kapitza-Dirac Diffraction

The diffraction of matter on a pulsed standing light wave can be seen as an analogon to the classical case of light diffraction on a grating but with reversed roles. The idea was originally proposed in 1933 by P. Kapitza and P. Dirac [Kap33], who suggested that one can diffract electrons on a standing light wave. However, since the interaction between the electrons and the light-wave is very weak, it required the availability of high-power lasers to verify the effect experimentally in 2001 [Fre01, Fre02]. The generalization of Kapitza-Dirac diffraction to neutral atoms was proposed in 1966 [Alt66] and verified experimentally in 1986 [Gou86].

Kapitza-Dirac diffraction relies on a stimulated scattering process between the lattice photons and the atoms. In a simplified picture, this can be seen as a two-step process: The atom first 'absorbs' one photon from one of the lattice beams and then undergoes a stimulated 'emission' into the mode of the other lattice beam. Thus in total, although no energy is transferred, the atom experiences a net recoil of $p_{\text{rec}} = 2 \cdot \hbar \cdot k_l$, where $k_l = 2\pi/\lambda_l$ is the lattice vector of the standing wave. Depending on the interaction time with the light field, also higher order processes can occur and multiples of p_{rec} can be transferred.

Theoretically, the effect can be described as follows [Gad09, Fre02]: the standing wave changes the Hamiltonian \hat{H} which governs the evolution of the atomic wave function ψ to

$$\hat{H} = -(\hbar/2m) \partial_z^2 + V_0 \cos^2(k_l z), \quad (4.3)$$

where m is the atomic mass. Expanding the corresponding atomic wave function ψ in a basis consisting of plane waves populating the diffraction orders and taking into account that at $t = 0$ all atoms are in the zeroth diffraction order, one obtains

$$\psi(t) = \sum_n c_n(t) e^{i2nk_l z}, \quad (4.4)$$

where $n = 0, \pm 1, \pm 2, \dots$ and $c_n(t = 0) = \delta_{n,0}$. The probability that a certain diffraction order is populated after applying a pulse of length τ is then given by

$$P_n = |c_n(\tau)|^2.$$

To obtain the coefficients $c_n(t)$ one has to solve the time-dependent Schrödinger equation for the Hamiltonian (4.3) which leads to a set of coupled differential equations

$$i \frac{dc_n}{dt} = \frac{\alpha n^2}{\tau} c_n + \frac{\beta}{4\tau} (c_{n-1} + 2c_n + c_{n+1}). \quad (4.5)$$

Here the dimensionless parameter $\alpha = \tau/\tau^{(2)}$ describes the pulse duration in terms of the 2-photon recoil time $\tau^{(2)} = \hbar/E_{\text{rec}}^{(2)}$ where $E_{\text{rec}}^{(n)} = (n\hbar k)^2/2m$ is the n -photon recoil energy and $E_{\text{rec}}^{(1)} \equiv E_{\text{rec}}$. The dimensionless parameter $\beta = (V_0/\hbar)\tau$ describes the area of the pulse, namely the product of the lattice depth V_0 and the pulse duration τ . Due to the symmetry of the diffraction, one has to solve in general $N + 1$ coupled differential equations if there are N diffraction orders present. The highest transferable momentum is given by

$$\bar{n} = \sqrt{\beta/\alpha}, \quad (4.6)$$

and refers to the case when the potential energy V_0 is completely transferred into kinetic energy $E_{\text{kin}} = (2\bar{n}\hbar k)^2/2m$.

The evolution of the population probabilities can be understood when one compares the pulse length τ with the oscillation period $t_{\text{ho}} = 1/\omega_{\text{ho}} = \hbar/\sqrt{2V_0 E_{\text{rec}}}$ in the approximated harmonic potential of each lattice site.

- For $\tau \ll t_{\text{ho}}$, the Raman-Nath approximation is used which neglects the kinetic-energy term in the single-particle Hamiltonian (4.3) during the pulse application. This is justified because the atom's displacement due to the pulse is small compared to the lattice spacing d_l and thus the pulsed lattice can be interpreted as a thin phase grating, modifying the atomic wave function by a phase $\Phi = V_0 \cos^2(k_l z) \tau/\hbar$ [Ovc99] without affecting its spatial distribution. This leads to population probabilities

$$P_n = J_n^2 \left(\frac{V_0 \tau}{2\hbar} \right), \quad (4.7)$$

where J_n are Bessel functions of the first kind. Thus the pulse length can be seen as playing the role of the thickness in normal Bragg diffraction.

- For $\tau \gtrsim t_{\text{ho}}$ the atoms oscillate in the harmonic potential of the lattice sites. This leads to a periodically focusing and defocusing of the diffraction orders. Therefore the thin phase grating approximation is not valid anymore and the kinetic energy has to be considered. To obtain the populations in the different orders, one now has to solve the coupled differential equations (4.5) numerically [Gad09, Huc09, Ovc99].

In our measurements, we operated in the regime $0.16 \leq \tau/t_{\text{ho}} \leq 1.5$ corresponding to a maximal transferred momentum of $\bar{n} = 4$. Thus to account for the relative population probabilities correctly, one would have to solve the coupled differential equations numerically. However for the sake of simplicity, we use the much simpler Raman-Nath approximation (4.7) to fit our data. Thus the absolute value of our determined lattice depth is not very precise but has a large error.

This approximation is nevertheless useful for us since we used it as an alignment tool to check how the lattice depth V_0 improved in each iteration of our alignment procedure. Apart from that, we could also infer the spacing between pancakes from this measurement, since the transferred momentum and thus the position of the peaks is independent of the approximation.

4.4.2. Experimental Results

We use this rough estimate of the pancake depth V_0 to improve the alignment of the trap by comparing the result to a projected value using a Mathematica calculation. In our first iteration our measured value for the trap depth V_0^{exp} was about a factor of ten smaller than the projected value V_0^{calc} , indicating that we had aligned the outer pancakes of the intersection which are not as deep as the center ones, with the center of the dipole trap. Readjusting for that, we improved the deviation to a factor of three and by fine-tuning the overlap of the two traps our last iteration yielded $V_0^{\text{calc}} \approx 2V_0^{\text{exp}}$. In the following we present the general measurement procedure as well as the results of this last iteration in detail.

In order to be able to see the imparted discrete momentum on the atoms, it has to be larger than the initial momentum distribution of the cloud. Since our pancake spacing is on the order of $4 \mu\text{m}$, the imparted momentum is on the same order as the Fermi momentum of a degenerate Fermi gas and thus it is not possible to observe this effect with such a cloud. Thus we produce a Bose-Einstein condensate of molecules, which has a much narrower momentum distribution and is therefore better suited. Then by doing a time-of-flight (TOF) image of the cloud, it is possible to separate the momentum peaks and thus evaluate the relative populations.

To produce the mBEC, the evaporation is done in the dipole trap down to a trap depth of about $V_0 \approx 120 \text{ nK}$ at a magnetic offset field close to the resonance ($B = 795 \text{ G}$) where the scattering length is large and positive, and we end up with a mBEC of ~ 8000 molecules.

To let the molecules expand slowly, we lower the trap depth within 25 ms further down to $V_0 \approx 30 \text{ nK}$ to decrease the chemical potential μ before switching off the trap. Simultaneously, we ramp down the magnetic offset field to $B = 650 \text{ G}$ where the molecules are still stable but the scattering length is smaller to decrease the mean-field interaction of the mBEC during the expansion.

Then immediately after the dipole trap is switched off, the pulse is applied with the pancake beams. Its length is controlled to be between $11 \mu\text{s}$ and $101 \mu\text{s}$ via the AOM switch which can be set in $1 \mu\text{s}$ steps. After a TOF of 10 ms relative to off-switching the dipole trap, an absorption image is taken along the pancake beam axis. To image the molecules, 3 ms before taking the absorption image we ramp the magnetic field back up to $B = 770 \text{ G}$. In Figure 4.5 one can see (averaged) absorption images of our last iteration of the measurement. In the case when there is no pulsed standing light wave applied, the cloud just expands isotropically with a mean momentum p_{rms} . When applying the pulsed standing light wave however, symmetric diffraction peaks emerge with momentum $\pm 2n\hbar k_{\text{PC}}$. From the spacing between the peaks, the relative height of the diffraction orders and the applied pulse durations we can then obtain an estimate of the pancake depth and the spacing as

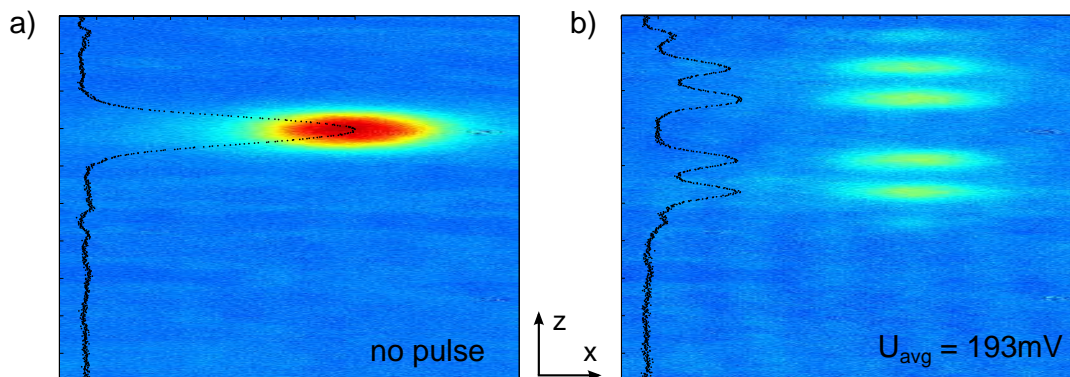


Figure 4.5.: **Emergence of Kapitza-Dirac diffraction when turning on the pulsed standing wave.** a) TOF picture when no pulse is applied. The black data inlay is an integration along the vertical axis. b) TOF picture when a pulse is applied. The emergence of symmetric, equally spaced diffraction peaks can be observed. Both pictures represent an average over ~ 75 shots.

explained in Section 4.4.1.

Because we use the AOM in front of the fiber as our pulse shutter but the PID-feedback gets its signal from the photodiode after the fiber, we are not able to stabilize the power in the pancake beams during the pulse. That means that the total power in the pancake beam varies from shot to shot by up to 20 % but as the power fluctuations within each pulse are small we assume a constant pancake depth V_0 within each pulse. Thus we also record the averaged integrated voltage U_{avg} within a time of $200 \mu\text{s}$ on the photodiode for each shot. We make sure that each pulse duration is completely captured within this $200 \mu\text{s}$ time window and thus U_{avg} is then a decent approximation of the pulse area β . Therefore by binning the data according to this averaged integrated voltage U_{avg} using a bin size of 20 mV with a MATLAB script and taking the average for each bin, we are able to increase the SNR of the data and look at the evolution of the diffraction pattern for increasing pulse areas β .

For each bin, the integrated line profiles along the vertical axis are fitted using a model which describes the population of the diffraction peaks according to the simple approximation of equation (4.7)

$$f(z) = bg + A \cdot \sum_{n=0, \pm 1, \dots}^{\pm 4} J_n^2(\beta/2) \cdot \exp\left[-\frac{(z - (z_0 + n\Delta z))^2}{2\sigma^2}\right], \quad (4.8)$$

where the fit parameters are defined as follows: bg is the background, A is the amplitude, $\Delta z = t_{\text{TOF}} \cdot p_{\text{rec}}/m_{\text{Li}_2}$ is the distance between adjacent peaks, β is the total pulse area in units of \hbar , z_0 is the position of the center peak and σ is the width of each Gaussian peak. For the last iteration of the measurement, the pulse duration was scanned between 11 and $101 \mu\text{s}$ in steps of $10 \mu\text{s}$ and the average power in the pancake beams was about $P \approx 355 \text{ mW}$. This lead to values between 33 mV and 292 mV for the averaged photodiode voltage U_{avg} . In Figure 4.6 the result of

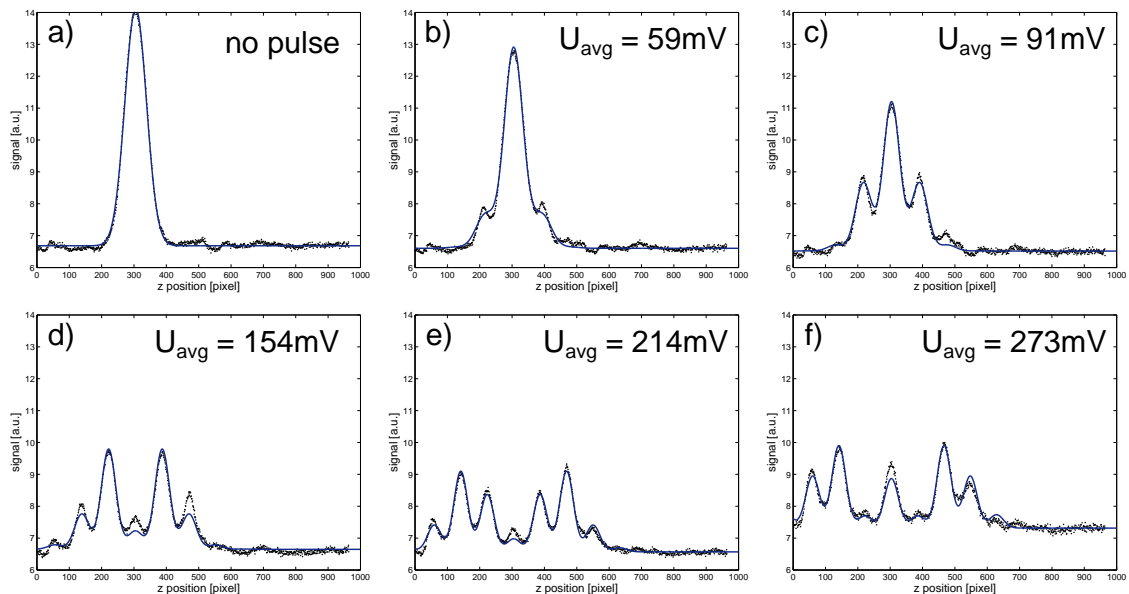


Figure 4.6.: **Evolution of the diffraction pattern for different pulse areas.** In a) no pulse was applied. In b)-f) the pulse area β which is connected to U_{avg} was varied. This was done by scanning the pulse duration between 11 and 101 μs and having a varying power in the pancake trap beam, fluctuating around a mean value of $P \approx 355 \text{ mW}$.

this fit for a selection of values of U_{avg} is shown. One can see that the height of the zeroth diffraction order shrinks for increasing pulse areas and that higher diffraction orders begin to emerge symmetrically. In panel f), one can see that there is even a revival of the zeroth order momentum peak for large pulse areas. Although the position of the peaks is reproduced well by the fit, the relative heights of the diffraction peaks differ from our simplified model. Hence a numerical approach would be needed to reproduce the heights correctly. Nevertheless, we used these fits to obtain information about the pancake spacing d_{PC} and the trap depth V_0 of the pancakes. First, we inferred the lattice wavelength λ_{PC} and thus the pancake spacing $d_{\text{PC}} = \lambda_{\text{PC}}/2$ using the fit parameter Δz which corresponds to the distance between adjacent peaks. One can calculate the lattice wavelength to be

$$\lambda_{\text{PC}} = \frac{4\pi \cdot \hbar \cdot t_{\text{TOF}}}{m_{\text{Li}_2} \Delta z}, \quad (4.9)$$

using the definition of the lattice vector $k_{\text{PC}} = 2\pi/\lambda_{\text{PC}}$ and converting Δz from pixel to micrometer using the known magnification of the imaging setup (see Section 3.4). Therefore, λ_{PC} is linear in the magnification resulting in an error $\Delta\lambda_{\text{PC}}$ on the order of 10% due to the uncertainty of the magnification in this imaging axis. In Figure 4.7 a) the result of the wavelength calculation is shown. One can see from the saturation of the curve that this method is more reliable for longer pulses when more peaks are present. Hence we only used the values above $U_{\text{avg}} = 170 \text{ mV}$ to fit a constant value. This results in a pancake spacing $d_{\text{PC}} = \lambda_{\text{PC}}/2 = (3.6 \pm 0.36) \mu\text{m}$, where the error is dominated by our estimated magnification uncertainty of 10%.

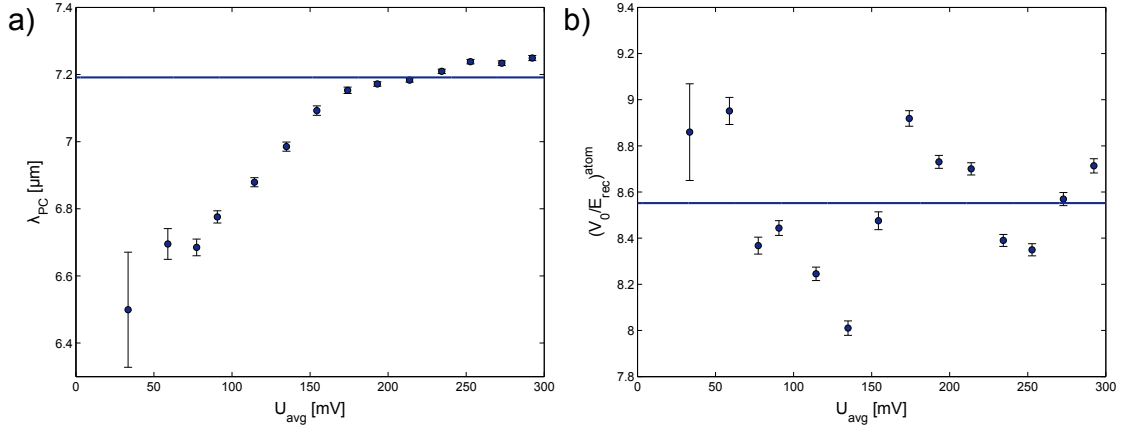


Figure 4.7.: **Estimation of the lattice wavelength λ_{PC} and the trap depth V_0 .**
 a) Lattice wavelength λ_{PC} versus the averaged photodiode signal U_{avg} . The blue line is a fitted constant to the values above $U_{\text{avg}} = 170$ mV. b) Atomic trap depth V_0 in units of the atomic recoil energy E_{rec} versus the averaged photodiode signal U_{avg} . The blue line represents a constant fit to the data.

Within our magnification uncertainty this is in good agreement to our Mathematica calculation of $d_{PC}^{\text{theo}} = 3.9 \mu\text{m}$ and thus we can conclude that our alignment of the intersection angle is very close to what we planned for since the pancake spacing depends only on this angle (see equation (2.50)).

In addition to the pancake spacing, we can also roughly estimate the depth of the pancake potentials V_0 and compare it to our projected depth at the given beam power. The trap depth V_0 can be calculated from the fit parameter β as

$$V_0 = \frac{\beta \hbar}{\tau}. \quad (4.10)$$

Because we want to calculate V_0 in units of the atomic recoil energy $E_{\text{rec}}^{\text{atom}} = \frac{\hbar^2 k_{PC}^2}{2m_{Li}}$, we have to take into account that the potential the molecules experience is twice as deep as the atomic trap depth, hence $V_0^{\text{mol}} = 2V_0^{\text{atom}}$. To calculate $E_{\text{rec}}^{\text{atom}}$ we took the value of k_{PC} we obtained from the inferred lattice wavelength λ_{PC} and τ was taken as the averaged pulse duration at each U_{avg} . The result of this estimated atomic trap depth V_0 for the different pulse areas U_{avg} can be seen in Figure 4.7 b). The oscillation of the estimated trap depth V_0 is due to the shot-to-shot variations of the applied pulse power. Its mean value is $(V_0/E_{\text{rec}})^{\text{atom}}_{\text{exp}} = 8.55 \pm 1.71$ at a mean power of $P \approx 355$ mW where the error - which is larger than the fluctuation of the data around the mean - is again given by the magnification uncertainty of the imaging setup. This is of course only a crude approximation since additional systematic errors due to our simplified approach are neglected. A calculation of the trap depth with Mathematica at this beam power however yields $(V_0/E_{\text{rec}})^{\text{atom}}_{\text{theo}} = 19.38$. Therefore in the experiment we are about a factor of 2.27 ± 0.46 smaller than expected. This would lead e.g. to a factor of 1.5 smaller trap frequencies. This is in good agreement with the factor of 1.8 we got from our trap frequency measurement. However we

have not investigated so far where this deviation comes from since it should not limit us to reach the regimes we planned for in the experiment.

In summary, we concluded with this measurement that we have aligned the pancakes as best as possible with the dipole trap and thus we proceeded to investigate how we can load a single pancake.

4.5. Counting the Filled Pancakes: Radio-Frequency Tomography

After successfully loading atoms into our pancake trap and improving the alignment via the measurement explained in Section 4.4, we wanted to investigate how the atoms are distributed over the individual pancakes when we do the transfer. Thereby we obtain a tool to count how many of the pancakes we have to deplete in order to prepare a single pancake. This will set a limit on the efficiency and time it takes to prepare a single pancake.

The idea of this measurement is to impose a magnetic field gradient in vertical direction² and hence spatially change the resonance frequency for radio-frequency (rf) transitions between the three lowest hyperfine states. If the difference in resonance frequency between adjacent pancakes is larger than the width of the rf-transition, it is then possible to selectively address each pancake by applying an rf-pulse at its resonance frequency. By preparing all the atoms in state $|2\rangle$ and driving the transition to the unoccupied state $|3\rangle$, one can then measure the atom number in each pancake by scanning over the applied rf-frequency.

In the following, the basics of rf-transitions are briefly summarized first and the calibration of our rf-setup is discussed. Subsequently, the experimental sequence and our evaluation method is explained in more detail. At last the results are presented and their implications for the short and long term stability for the pancake trap is discussed.

4.5.1. Basics on Radio-Frequency Transitions

In the experiment, we operate at magnetic fields $B > 100$ G where in ${}^6\text{Li}$ the three lowest hyperfine states $|1\rangle$, $|2\rangle$ and $|3\rangle$ only differ by their nuclear spin which is decoupled from the electron spin. Driving transitions between these states hence corresponds to flipping the nuclear spin and can be described by a magnetic dipole transition, making it effectively a two-level system³. The oscillatory electro-magnetic field is provided by an rf-antenna inside the experiment chamber. When applying a frequency which is resonant to the energy difference between two states, the atoms will start to oscillate between these states which can be described by Rabi oscillations.

²This direction is in the following referred to as the z-direction.

³The splitting between the states is on the order of 80 MHz and thus far bigger than the width of the transitions.

Theory of Rabi Oscillations

Rabi oscillations can be described in the framework of a two-level system with a harmonic perturbation $V(t) \propto \sin(\omega t)$ [Bra03]. If the atom was initially in the ground state $|g\rangle$, the coupling with the oscillatory field leads to a superposition $|\psi(t)\rangle = a(t)|g\rangle + b(t)|e\rangle$. The probability for the atom to be in the excited state $|e\rangle$ after application of the resonance frequency ν_{res} for a time t is then given by

$$P_{|e\rangle} = |b(t)|^2 = \sin^2\left(\frac{\Omega t}{2}\right), \quad (4.11)$$

where Ω is the so called Rabi frequency. The Rabi frequency Ω depends in essence on the strength of the coupling and thus scales linearly with the amplitude of the applied oscillatory magnetic field B . Since B scales with the applied rf-power P as $B \propto \sqrt{P}$, we can achieve large Rabi frequencies by applying strong rf-pulses. The time required to completely invert the population is called a π -pulse and its time is given by $t_\pi = 2\pi/\Omega$. Therefore one is only limited by the applicable rf-power and hence we took great care to optimize our rf-setup [Heu11].

Detuning the driving field from resonance by Δ leads to a decreased transfer efficiency and faster oscillations, modifying equation (4.11) to [Met99]

$$P_{|e\rangle} = \left(\frac{\Omega}{\Omega_{\text{eff}}}\right)^2 \sin^2\left(\frac{\Omega_{\text{eff}} t}{2}\right), \quad (4.12)$$

where $\Omega_{\text{eff}} = \sqrt{\Omega^2 + \Delta^2}$ is the effective Rabi frequency.

Application to the RF-Tomography

In our rf-tomographic measurement, instead of having a mixture of atoms in $|1\rangle$ and $|2\rangle$, we start with atoms only in state $|2\rangle$ and transfer them into the unoccupied state $|3\rangle$.

To determine the resonance frequency of the $|2\rangle - |3\rangle$ transition, an ultracold mixture of atoms in $|1\rangle$ and $|2\rangle$ is loaded into the pancake trap. Interactions between the states can lead to a loss of atoms and coherence⁴ as well as a shift of the resonance frequency⁵. Therefore we remove the atoms in state $|1\rangle$ by shining in a resonant pulse with the imaging beam⁶ which leaves the atoms in state $|2\rangle$ unaffected. Subsequently, a 25 ms long rf-pulse - corresponding to a Fourier limited width of ~ 40 Hz - is applied which transfers atoms into the previously unoccupied state $|3\rangle$. On resonance this leads to a loss of atoms in state $|2\rangle$ when scanning the rf-frequency. The resonance frequency of the transition is then determined using a Lorentzian fit and the exact magnetic field can be inferred using the Breit-Rabi formula [Her08]. Note that this formula is only for the homogeneous case and does not include effects like the

⁴Collisions between atoms project the superposition state ψ back into the states $|1\rangle$ and $|2\rangle$.

⁵Also known as clock shifts [Ket08]. They can be used as a sensible measurement method to detect interaction energies in rf-spectroscopy e.g. [Zür13].

⁶The momentum transfer from the scattering gives enough kinetic energy to kick the atoms out of the trap.

trapping potential or inhomogeneities in the magnetic field. This leads to systematic errors which would have to be included if one was interested in an absolute magnetic field. However, in our case we are only interested in the relative frequency differences at a fixed magnetic field and thus we did not investigate these systematic errors. A typical measurement of the resonance frequency at a given magnetic field can be seen in Figure 4.8 a). Here the resonance frequency was $\nu_{\text{res}} = 84.614732$ MHz with an error of 11 Hz and the magnetic offset field was calculated using the Breit-Rabi formula to be $B = 526.692$ G. The applied rf-power was set to -29 dBm at the source⁷, corresponding to a Rabi frequency of about $\Omega \approx 2\pi \cdot 31$ Hz. The lifetime of

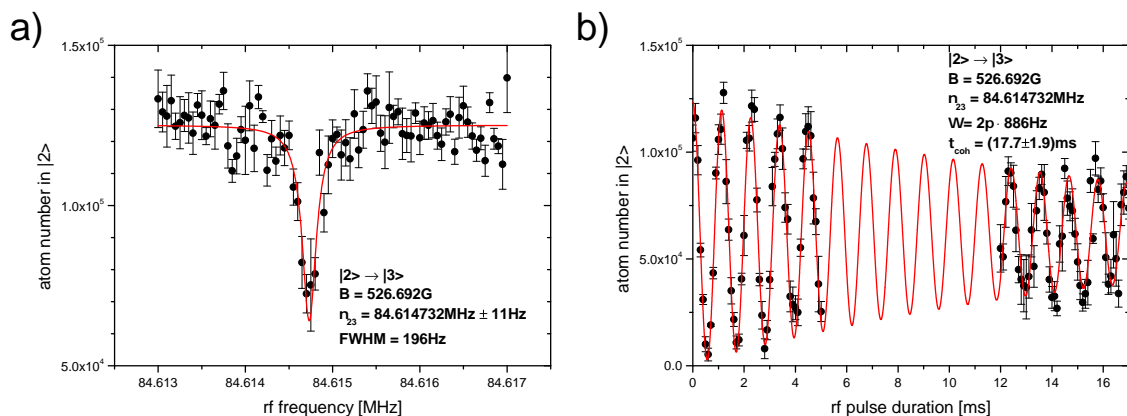


Figure 4.8.: **Calibration of the resonance frequency and decoherence time.**

a) Frequency sweep across the resonance for the $|2\rangle$ - $|3\rangle$ transition. The resonance frequency was determined via a Lorentzian fit and was used to infer the magnetic field via the Breit-Rabi equation [Her08]. b) Rabi oscillations of the $|2\rangle$ - $|3\rangle$ transition at the resonance frequency. A damped sine function was used to fit the data points and determine the Rabi frequency Ω and coherence time τ_{coh} . Note that the applied rf-power in a) is about a factor 1000 smaller than in b) and thus the Rabi frequency in a) is only $\Omega \approx 2\pi \cdot 31$ Hz.

the hyperfine states is much larger than any timescales in the experiment, and thus the natural linewidth of the transition is negligible. Because the Fourier limited width of the applied pulse is much smaller than the $\text{FWHM} = 196$ Hz of the rf-transition, the rf-width is solely limited by magnetic field inhomogeneities in the experiment and the difference in magnetic moment $\Delta\mu_{\text{mag}}^{(2)-|3\rangle}$. In our case of the three lowest hyperfine levels of ${}^6\text{Li}$, in a good approximation only the nuclear spin gets flipped. Thus the magnetic field sensitivity is very small because the coupling of the nuclear spin to the magnetic field is much weaker than e.g. the coupling of the electron spin. In combination with our magnetic field stability on the order of 10 mG, this enables us to achieve these small rf-transition widths. Note that the transition can also be broadened due to saturation effects if the driving force is too strong.

⁷This is not the final power that reaches the rf-antenna since the signal is then also amplified and impedance matched to the antenna.

Apart from the pulse duration and the detuning, the transfer efficiency is also affected by decoherence effects. Due to inhomogeneities in the magnetic field, the atoms accumulate different phases and thus the signal dephases. In a completely dephased sample, the atoms will then be in a 50/50 mixture between the states. In addition, decoherence is also introduced due to collisions between atoms which speeds up this process. To determine the coherence time τ_{coh} in our setup, we prepare atoms in state $|2\rangle$ as before and apply a varying pulse duration τ to see how the population in state $|2\rangle$ oscillates. This measurement was done at the same magnetic field we used to determine the resonance frequency ν_{res} . Because the coherence time is on the order of ms, we had to increase the power in the rf-pulse considerably by 29 dBm (factor ~ 1000) in order to have a large enough Rabi frequency to achieve a t_π which is small compared to τ_{coh} . The result of this measurement can be seen in Figure 4.8 b). The oscillations were fitted using a damped sine function and resulted in a Rabi frequency $\Omega_{\text{eff}} = 2\pi \cdot 886$ Hz and a coherence time $\tau_{\text{coh}} = (17.7 \pm 1.9)$ ms. Hence if we want to do coherent transfers later on, we should limit our pulse lengths to be shorter than the coherence time τ_{coh} .

One should note that decoherence effects are actually important in the experiment because when driving a coherent pulse to an ultracold Fermi gas, there will be no s-wave interaction between the atoms since they will all be in the same superposition state [Ket08]. Therefore a decoherence mechanism is needed to develop a true mixture of states and thus have interactions. Being no longer identical, the atoms can then interact via s-wave collisions which will further reduce the coherence.

4.5.2. Experimental Results

To perform the rf-tomography, we prepare a degenerate Fermi mixture in states $|1\rangle$ and $|2\rangle$ in the dipole trap. The evaporation is done down to a trap depth of $0.12 \mu\text{K}$. Thus we have a very cold sample of only about $\sim 20,000$ atoms. This ensures that the atoms in the pancakes are close to the center in each pancake and thus well separated. The rf-resonance frequency can then be seen as constant for each pancake which is important to achieve a sufficient rf-resolution although it results in low atom numbers and thus a bad signal-to-noise ratio (SNR) for the imaging.

Then the rf-tomography is performed which is illustrated in Figure 4.9. Immediately before the transfer into the pancake trap, the dipole trap depth is ramped up within 200 ms to a trap depth of $3 \mu\text{K}$. This compresses the atomic cloud in all three dimensions and hence reduces its vertical extension, thus ensuring that we load as few pancakes as possible, but also leads to heating which we hope does not affect the measurement too strongly. After this ramp, the power in the pancake beams is ramped up to $P_{\text{total}} \approx 3.36$ W and the dipole trap is turned off slowly.

Before shooting out the atoms in state $|1\rangle$ by applying the resonant imaging pulse, the magnetic offset field is set to $B \approx 527$ G where the scattering length a_{12} has its zero-crossing. Then the imaging light is applied for $10 \mu\text{s}$ which is sufficient to kick out all atoms in $|1\rangle$. Subsequently, a magnetic field gradient dB/dz is applied with the MOT coils to shift the resonance frequency across the pancakes. Since the center of the MOT does not coincide with the center of the dipole trap, the gradient also

shifts the overall resonance frequency compared to the calibration in Figure 4.8. In our current setup, when driving the MOT power supply at a maximal current of about 30 A, we are able to apply a magnetic field gradient in z -axis in the range of $dB/dz = 40 - 50$ G/cm. With our pancake spacing of $d_{PC} \approx 4 \mu\text{m}$ this leads to a separation between adjacent pancakes in frequency space of about 250 – 350 Hz. This is just slightly more than the width of our rf-transition (FWHM = 196 Hz) and thus limits our achievable resolution. In addition to shifting the frequency, the magnetic field gradient also exerts a force $F \propto dB/dz$ on the atoms, thus removing weakly trapped atoms. To be sure that the gradient reaches a constant

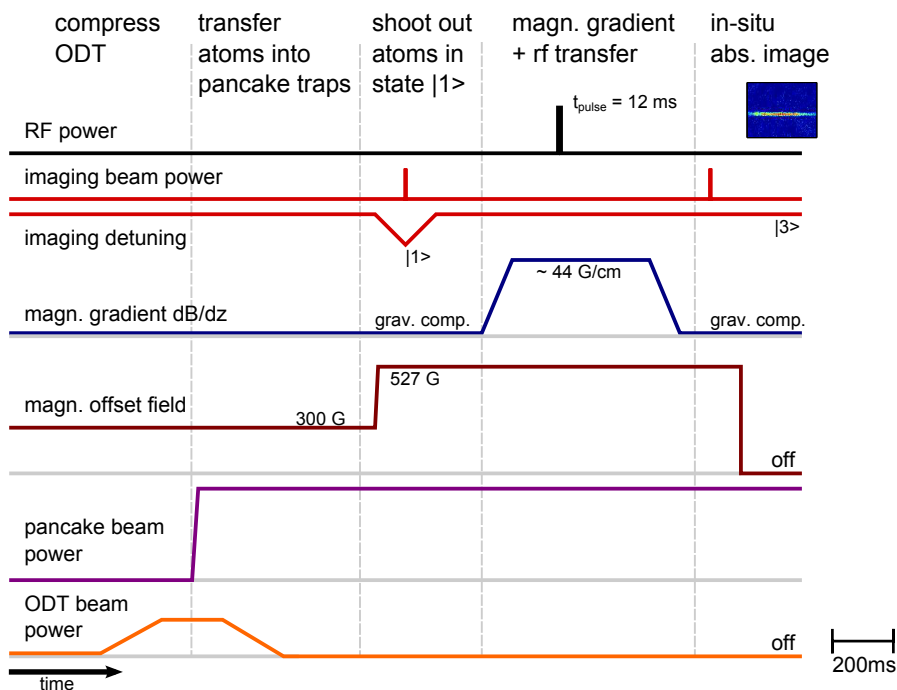


Figure 4.9.: **Illustration of the timing graph for the rf-tomography.** The starting point for the sequence is a degenerate Fermi gas as prepared in Figure 3.1. The horizontal time axis has a scaling as shown in the bottom right corner. The vertical axes do not scale properly and just show the qualitative behavior. The gray horizontal lines indicate the zero values. Note that only the relevant channels to understand the rf-tomography are shown.

value after the ramp and the atom number is constant, we wait another ~ 300 ms before applying the rf-pulse. The rf-power is set to -28.5 dBm to avoid power broadening of the transition, which corresponds to a Rabi frequency of $2\pi \cdot 33$ Hz and thus a π -pulse duration of $t_{\pi} \approx 30$ ms. The rf-pulse duration is chosen to be $t_{\text{pulse}} = 12$ ms - corresponding to a Fourier limited width of ~ 100 Hz - as a trade-off between transferring a large percentage of the atoms while still being mostly coherent. After the rf-transfer, the voltage in the MOT coils is ramped down again to the value of the gravitation compensation and the atoms in state $|3\rangle$ are imaged

in-situ along the horizontal MOT axis. The imaging itself imposes two challenges:

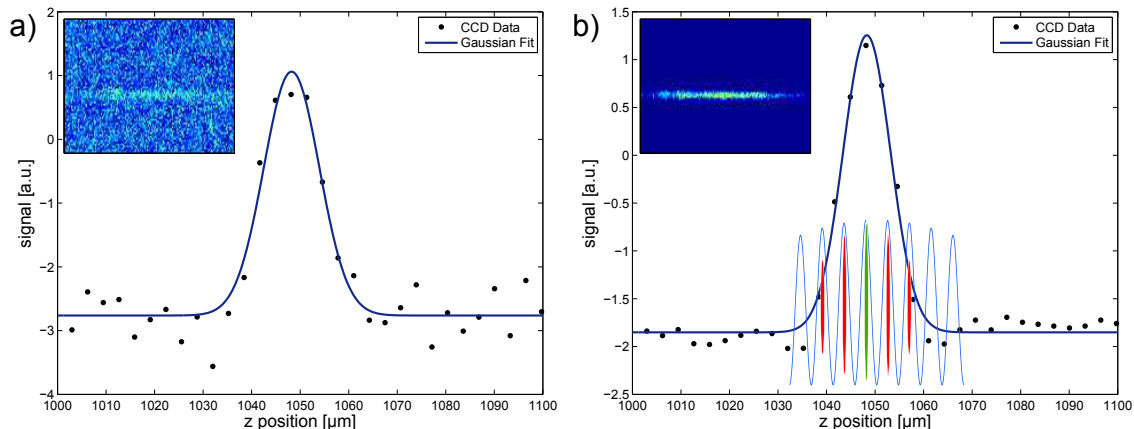


Figure 4.10.: **Comparison between a single shot and an average of 50 shots.**

a) The profile is an integration along the vertical axis for a single shot. The inlay is a picture from the CCD camera. b) Average taken of ~ 50 shots. The inlay in the profile highlights that the individual pancake structure cannot be resolved and the separation between pancakes is only slightly more than 1 pixel. The shots were taken at the center pancake where the atom number is largest. For the outer pancakes, the decreased SNR makes the averaging process even more important.

first of all, the atom numbers in each pancake is very small with at most 3000 atoms per pancake. As a result, the SNR is quite low and it is challenging to have good fits for a single shot. Furthermore, as the pixel size of the camera is $6.45 \mu\text{m}$ and the magnification of the imaging is $M = 2$, adjacent pancakes are only separated by one pixel. But using a larger magnification would not help since we are not able to resolve the pancake structure due to our limited resolution in horizontal direction and thus this would only decrease the SNR further.

To still be able to obtain good results, we post-process all our data using MATLAB. At first, we average all the data taken at each frequency and fit the resulting atomic clouds along the z-axis using a Gaussian distribution. From this fit we can infer the atom number, vertical position of the center and the width of the cloud. Although the fitted width does not represent the actual pancake width as we cannot resolve it, we can still differentiate the different center positions for two adjacent pancakes. To make sure that the atom number is calculated correctly, we cross checked the method with our standard LABVIEW procedure. After that we use the information of the averaged fits to provide better starting parameters to fit each individual shot. In Figure 4.10 a comparison between a single shot and an average of 50 shots can be seen. In the following the results are shown for a measurement where we repeated the frequency scan approximately 200 times. First we averaged the images at each frequency over all runs and then obtained the number of atoms, center position and width of the cloud by fitting the overall data with a Gaussian distribution like in Figure 4.10. The results of this process are shown in Figure 4.11.

In graph a) the center position of the Gaussian fit is plotted versus the applied

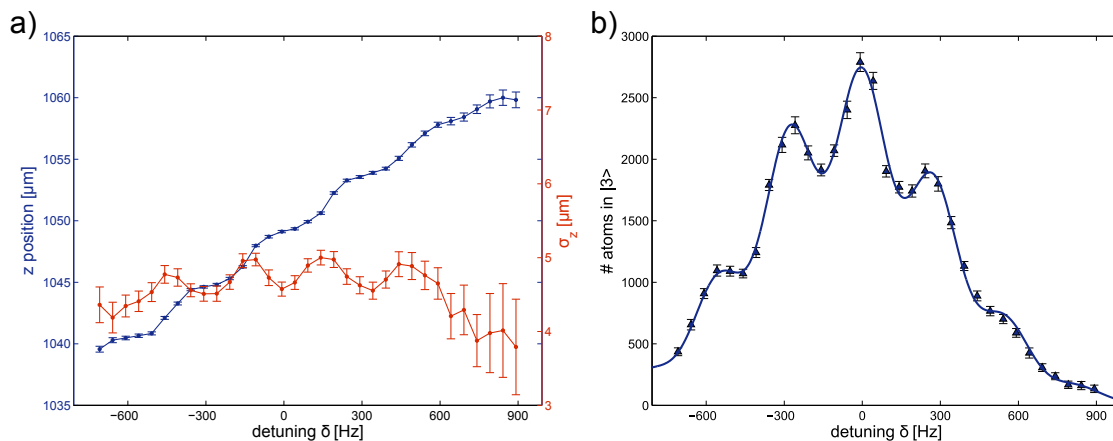


Figure 4.11.: **Results from averaging over all runs.** a) Left axis: z position (center of the Gaussian fit) versus applied rf-frequency. Right axis: width σ_z of the Gaussian fit versus applied rf-frequency. The lines are just guide to the eyes and the detuning is relative to the center pancake position obtained from the fit in b). b) Number of atoms in state $|3\rangle$ versus applied rf-frequency. The blue line is a fit to the data as explained in the text and the detuning is relative to the center pancake position obtained from the fit.

frequency - where the detuning δ is given in respect to the resonance frequency of the center pancake. This results in a step-function with each step corresponding to an individual pancakes. As one can see, the steps are not sharp but are of course smoothed by our limited rf-resolution. In the same graph, also the width σ_z of each Gaussian fit is plotted. It is evident that the width increases if one is on the slope between steps. Note that this width does not represent the actual density distribution inside a single pancake since the imaging resolution is not good enough to resolve it. However it still gets larger if one transfers atoms from two pancakes, which explains the increase between two steps. The distance between each step can be roughly estimated to be $(4.3 \pm 0.3) \mu\text{m}$ which is almost within 1σ of the calculated pancake spacing of $3.9 \mu\text{m}$ which was already verified in the Kapitza-Dirac diffraction measurement. Thus the measured pancake spacing is in reasonable agreement with these measurements and confirms our projected spacing. At larger frequencies above a detuning of 600 Hz, the errors increase due to the low number of atoms and the trend of the step-function cannot be trusted.

In graph b), the number of transferred atoms into state $|3\rangle$ is shown as a function of the applied frequency - where the detuning δ is again given in respect to the resonance frequency of the center pancake. Qualitatively, one can see five distinctive peaks in atom number, which corresponds to the case when the applied rf-frequency is resonant with the atoms in one of the pancakes. However as the peak separation of ~ 300 Hz is on the same order as the FWHM of the rf-transition, the atom number does not drop to zero between peaks as one transfers atoms from both pancakes. From the relative height of the peaks, we can conclude that about 80 % of the atoms

occupy the three center pancakes.

To get more quantitative information, we fit the data making the following assumptions. The distribution of atoms in the dipole trap can be modeled by a Gaussian distribution with center ν_{ENV} , width σ_{ENV} and amplitude A . Because we directly transfer the atoms from the dipole trap into the pancake traps by ramping up the power in the pancake beams, this gives us the envelope of the fit. The number of transferred atoms from each pancake follow a Gaussian distribution as well where the width σ_{PC} is given by the rf transition width. We fix the position of one of the pancakes at ν_{PC} and set a fixed spacing $\Delta\nu_{\text{PC}}$ between adjacent pancakes. The height of each peak is only given by the envelope function. At last we also allow for a small background bg in atom number. Combining these assumptions then leads to the fitting function

$$N_{|3\rangle}(\nu) = bg + A \cdot e^{-\frac{(\nu-\nu_{\text{ENV}})^2}{2\sigma_{\text{ENV}}^2}} \cdot \left\{ e^{-\frac{(\nu-\nu_{\text{PC}})^2}{2\sigma_{\text{PC}}^2}} + \sum_{n=1}^3 e^{-\frac{(\nu-(\nu_{\text{PC}}\pm\Delta\nu_{\text{PC}}))^2}{2\sigma_{\text{PC}}^2}} \right\}, \quad (4.13)$$

where \pm indicates a summation over both the negative and positive exponential term and we include up to 7 possible pancakes. As is evident from the graph, our assumptions are justified and the fit is in good agreement with the data. The fit results for the parameters can be seen in Table 4.1. Using the Breit-Rabi formula one can

fit parameter	value
ν_{ENV}	(84.635059 ± 0.000003) MHz
σ_{ENV}	(373 ± 8) Hz
ν_{PC}	(84.635108 ± 0.000002) MHz
σ_{PC}	(103 ± 2) Hz
$\Delta\nu_{\text{PC}}$	(294 ± 3) Hz

Table 4.1.: **Fit results from the fit in Figure 4.11 a).** The errors given are the 1σ errors of the fit.

transfer the results from frequency space into magnetic field differences. Knowing our magnetic field gradient, we can then translate this further into spatial information. The distance between the pancakes is $\Delta\nu_{\text{PC}} \approx 294$ Hz which corresponds to a magnetic field difference of $\Delta B \approx 18.8$ mG. With the estimated pancake spacing of $4.3 \mu\text{m}$ from graph a), we can infer that our applied magnetic field gradient must be on the order of $\text{dB}/\text{dz} = \Delta B/\text{d}_{\text{PC}} = 44$ G/cm which is in good agreement with a projected value of $\text{db}/\text{dz} = 43$ G/cm using a Mathematica calculation.

Taking the difference between ν_{ENV} and ν_{PC} as the distance between the center pancake and the dipole trap center, one can estimate the deviation of the two centers to be less than $0.7 \mu\text{m}$. The initial cloud size in the dipole trap can be estimated using σ_{ENV} to be $h_{\text{ODT}} \approx 21 \mu\text{m}$. This explains the occurrence of five peaks very well since the spacing between peaks is expected to be on the order of $4 \mu\text{m}$. When comparing $2 \cdot \sigma_{\text{PC}}$ to the $\text{FWHM} = 196$ Hz of the rf-transition, one can see that the width of the peaks is slightly higher than one would expect⁸. This can be explained

⁸Per definition, $\text{FWHM} > 2 \cdot \sigma$.

by positional fluctuations of the pancakes or magnetic field instabilities which smear out the width when averaging over many runs. Further information on these effects is given later when we investigate the short term stability of the trap during runs. But from these results we can already conclude that the positional stability of the pancake traps must be quite good since any large shifts during the measurement which lasted over a day would have washed out these features. In addition to looking

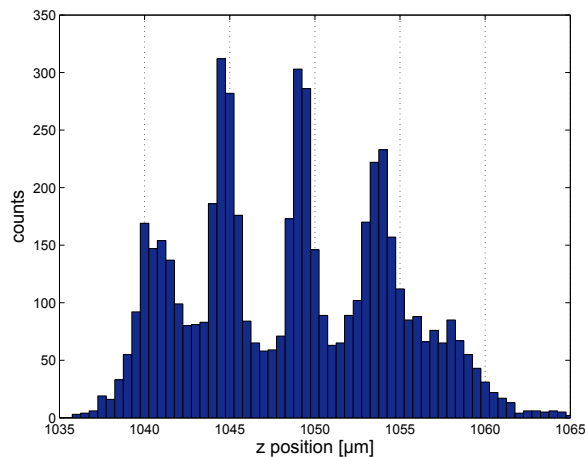


Figure 4.12.: **Histogram of all individual shots.** The z position is obtained as the center position from a Gaussian fit. The bin size is $0.5 \mu\text{m}$. All fits which did not converge have been excluded from the histogram.

at the results from averaging over all runs, we also fit each shot individually using the results obtained from the averaging as initial fit parameters. Since the SNR is very low, a lot of fits do not converge especially for low atom numbers. Hence we do a post-selection and neglect all fits which do not converge⁹. The histogram for the center position can be seen in Figure 4.12. One can clearly distinguish at least four pancakes with a spacing of about $4 - 4.5 \mu\text{m}$. The pancakes at the edge are not as pronounced as the ones in the center because there were less atoms and hence the SNR was worse. That the count rate does not go to zero between pancakes can again be attributed to the limited rf-resolution and hence the transfer of atoms from more than one pancake when applying an rf-frequency between adjacent pancakes.

Short Term Stability

During an experiment, the position of the dipole trap as well as the position of the pancake traps can drift or fluctuate. Since the magnetic field is spatially dependent, this leads to fluctuations in the resonance frequencies of the pancakes as well. Apart from that, also the magnetic field itself can vary due to the limited magnetic field stabilization. To determine the extent of these fluctuations during an experimental run, we bin together 11 consecutive runs, average them and evaluate the atom number in the same way as we do when averaging over all runs. Thereby we obtain

⁹Either a fit parameter hit a restraining bound or $\sigma_z < 3$ or $\sigma_z > 6$.

a temporal evolution of the fit parameters and can estimate the fluctuations in frequency space. Since every run has 33 frequency steps and each experimental cycle has a duration of about 12.9 s, this corresponds to averaging over a time interval of 78 min. For the aforementioned measurement, we measured the evolution of the fit parameters over ~ 26 h and the results can be seen in Figure 4.13. If we neglect the magnetic field instabilities during the run, we can associate the fluctuations of the fit parameters solely to positional instabilities of the dipole and pancake trap and thus obtain a lower bound for their short term stability.

From graphs c) & e), one can infer the drifts of the vertical dipole trap center position. The maximal fluctuation in the dipole trap center position is $|\delta\nu_{\text{ENV}}|^{\text{max}} = 65$ Hz. If one assumes that the magnetic field gradient was constant during all runs, this corresponds to a fluctuation in the dipole trap center position of at most $1 \mu\text{m}$ in vertical direction. This is consistent with direct measurements of the dipole trap center which indicate a similar level of stability. The vertical size of the dipole trap fluctuates by at most $2.6 \mu\text{m}$ which is on the order of 10 %. This might be caused by a breathing introduced by ramping up the dipole trap before the transfer or just by instabilities in the fits.

From graph b) which shows the fluctuation of the center pancake position, its positional stability can be estimated. This is very important for the deterministic loading of a single pancake, since any phase shift by more than $\Delta\phi = \pi/2$ between the beams would lead to sitting between two pancakes instead of filling one. If one takes again $|\delta\nu_{\text{PC}}|^{\text{max}} = 51$ Hz as an upper bound, this would correspond to a phase fluctuation of $\Delta\phi \leq \pi/5$. Using the rms value $\delta\nu_{\text{PC}}^{\text{rms}} = 24$ Hz of the data points, one obtains a phase fluctuation of about $\Delta\phi \leq \pi/12$. These small fluctuations over an extended period of measuring time lead us to believe that we can achieve a good fidelity in the future for preparing a single pancake. In addition, former measurements with an external test-setup have shown that shot-to-shot phase fluctuations of the interference fringes were even smaller at $\Delta\phi \leq \pi/30$ [Sta12].

From graph d) which shows the width of each pancake, we see that we overestimate the width when averaging over all runs. This can be explained by fluctuations of the pancake positions as well as magnetic field fluctuations which shifts the resonance frequencies in the pancakes. Averaging over all runs, this broadens the distribution around each peak and hence leads to an overestimation of σ_{PC} . Hence most data points have a smaller σ_{PC} than the value obtained from averaging over all runs (blue line). If one takes this into account and takes $\sigma_{\text{PC}} = 98$ Hz as a crude estimate for the average of the individual fits, then $2 \cdot \sigma_{\text{PC}}$ which is roughly equivalent to the FWHM coincides very nicely with the FWHM of 196 Hz of the calibrated rf-transition. Thus the width of each pancake in frequency space is basically given by the rf-transition width. This further confirms that almost all atoms in each pancake are tightly packed around the center.

At last, from graph f) we see that the fluctuations of the pancake spacing are very small on the order of 10 Hz which corresponds to changes less $0.1 \mu\text{m}$. This can largely be attributed to the accuracy of the fits, indicated by the large error bars.

In conclusion, the fluctuations while running the experiment seem to be sufficiently small to prepare a single pancake with good fidelity. Furthermore, no apparent drifts could be recognized while running the experiment.

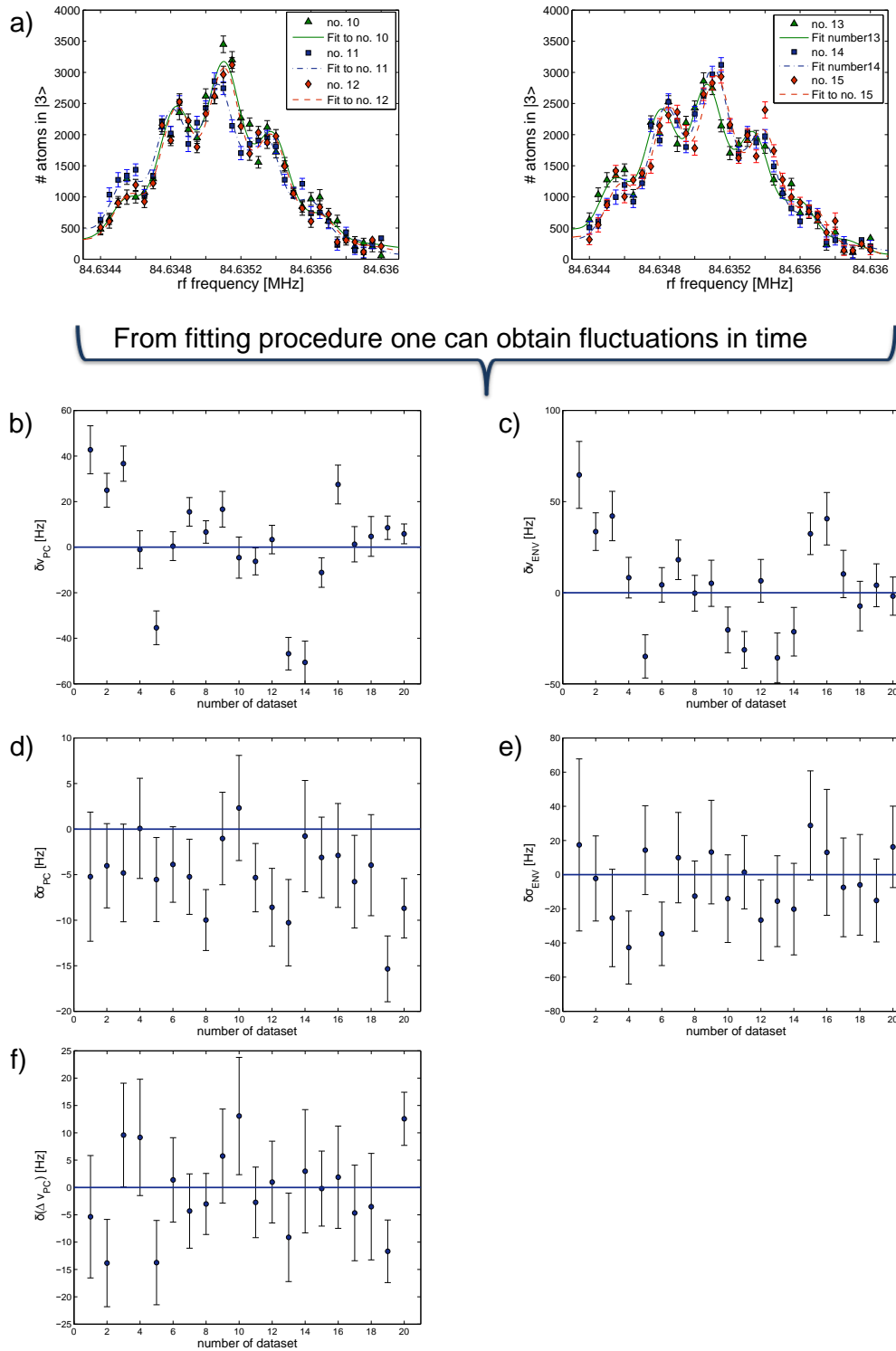


Figure 4.13.: **Fluctuation of the fit parameters as a function of measurement time.** a) An average of 11 consecutive runs, corresponding to about 78 min of measurement time, was fitted using equation (4.13). These fits were then taken to obtain the fluctuations of the fitting parameters in b)-f). The blue lines in each graph indicate the results obtained from the overall fit in Figure 4.11 and are listed in Table 4.1.

Long Term Stability

To evaluate long term drifts, which can occur when turning on and off the experiment, we took a second - somewhat smaller - dataset approximately a week later. We analyzed the data using the same methods as before and the result of this can be seen in Figure 4.14. From graph a) which shows the histograms of the center

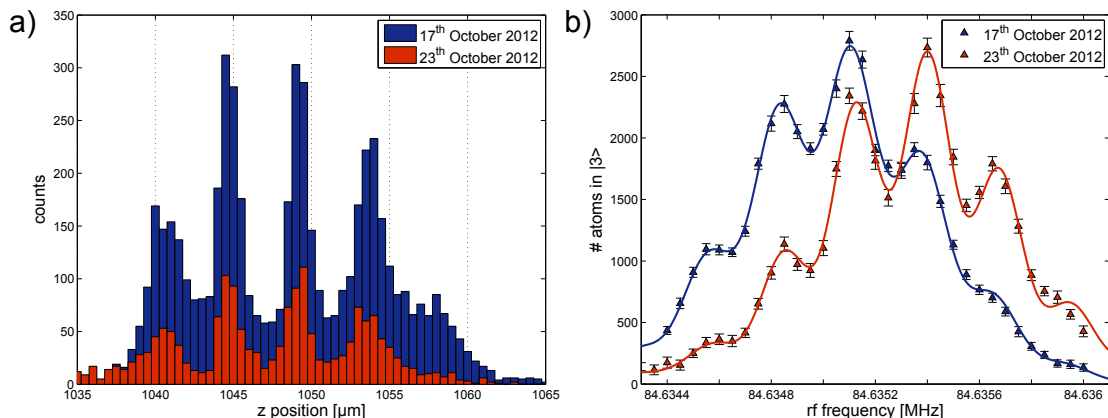


Figure 4.14.: **Comparison of the two separate measurements.** a) Histogram of the center positions of all individual shots. The bin size is $0.5 \mu\text{m}$. b) Number of atoms in state $|3\rangle$ as a function of the applied rf-frequency. The solid lines are fits to the data using equation (4.13).

position of all individual shots, we can see that the peaks of the pancakes coincide very well in both measurements¹⁰. As an upper bound we can estimate the stability of the pancake position to be better than $0.5 \mu\text{m}$, which corresponds to a phase drift $\Delta\phi \leq \pi/8$. This result gives us great confidence to deterministically prepare a single pancake with high fidelity in the future. The panel b) shows the transferred atom

fit parameter	data 17 th October 2012	data 23 th October 2012
ν_{ENV}	$(84.635059 \pm 0.000003) \text{ MHz}$	$(84.635339 \pm 0.000005) \text{ MHz}$
σ_{ENV}	$(373 \pm 8) \text{ Hz}$	$(358 \pm 7) \text{ Hz}$
ν_{PC}	$(84.635108 \pm 0.000002) \text{ MHz}$	$(84.635405 \pm 0.000002) \text{ MHz}$
σ_{PC}	$(103 \pm 2) \text{ Hz}$	$(93 \pm 2) \text{ Hz}$
$\Delta\nu_{\text{PC}}$	$(294 \pm 3) \text{ Hz}$	$(293 \pm 3) \text{ Hz}$

Table 4.2.: **Comparison of the fit results from the fits in Figure 4.14 b).** The magnetic field drifted between the measurements which leads to a shift in the measured frequencies. Note that the fitted frequencies only allow to make statements about the relative difference in the magnetic field between the measurements as we did not calibrate the systematic errors of our setup.

¹⁰The difference in height is due to the smaller dataset used in the second measurement.

number into state $|3\rangle$ as a function of the applied rf-frequency and the fit results are compared in Table 4.2. It is apparent that the profile has shifted by ~ 290 Hz to higher frequencies, which is one the same order as the pancake spacing $\Delta\nu_{PC}$. Because the position of the dipole trap is better than $1\ \mu\text{m}$, this indicates that we have long term drifts of the magnetic field. The shift in frequency space corresponds to ~ 19 mG within a week, which is reasonable with our magnetic field stability of the Feshbach coils better than 10 mG for short terms. However this means that we have to recalibrate the rf-transition frequency each time we want to do an radio-frequency dependent measurement.

Apart from this shift, one can see that the width of each pancake is smaller in our second measurement which is nicely visible in the graph in the form of deeper dips between two peaks. This is because we took less data the second time and thus fluctuations in the pancake position do not smear out the peaks that much. When comparing the pancake spacing, it is evident that it is constant over long times.

4.6. Towards the Preparation of Only a Single Pancake

In the future we want to do experiments with atoms only in a single pancake. Then we can with the help of two additional perpendicular lattice beams create a single layer of a two-dimensional optical lattice. Imaging this lattice from the top will then enable us to investigate the physics in a single lattice without the averaging over many realizations of the lattice at the same time.

There are in principle two paths for us to achieve this, either by directly loading only one pancake or by removing atoms from all but one pancake after filling several ones during the transfer. Both options are possible for future experiments and in the following our current progress with both methods is shortly summarized.

Transfer of a mBEC

In order to directly load a single pancake, one has to reduce the size of the cloud in vertical direction sufficiently before the transfer. In a mBEC all molecules have the same macroscopic wave function and there is no Fermi pressure. Therefore the size of the cloud is smaller for a mBEC than it is for a degenerate Fermi gas with the same number of atoms. But even for a mBEC the vertical size is larger than the size of a single pancake, therefore we create a time-averaged potential with larger horizontal extensions by modulating the ODT beam with an AOM in the horizontal plane. This increases the size of the cloud in the horizontal plane by a factor of two and thus decreases the size in the vertical direction. In addition to this 'painting', the center of the dipole trap can be shifted by applying a magnetic field gradient with the MOT coils. This is used to better overlap the dipole trap with the center pancake during the transfer.

We then prepare a mBEC in this time-averaged potential and repeat the rf-tomography measurement from Section 4.5. Because any interaction in the cloud leads to a shift and broadening of the rf-transition, we need again a one-component Fermi gas to perform the rf-tomography. Therefore we remove one component with

a resonant light pulse. In the case of a mBEC however, one cannot go to the zero-crossing of the scattering length since above the resonance there is none and the molecules are only stable close to the resonance on the BEC side. Thus in order to minimize the heating transferred to the atoms in state $|2\rangle$ when kicking out the atoms in state $|1\rangle$, we ramp the magnetic field across the resonance to $B \approx 1000$ G where the molecules dissociate and the interaction is as small as possible. We then apply the resonant light pulse to shoot out the atoms in state $|1\rangle$ and perform the same tomographic measurement as described in Section 4.5.

In Figure 4.15 the number of atoms in state $|3\rangle$ is plotted versus the applied rf-frequency - shown as the detuning δ relative to the center pancake resonance frequency - for a shift gradient which was optimized to load as much atoms as possible into only one pancake. As one can see it is possible to load a large fraction

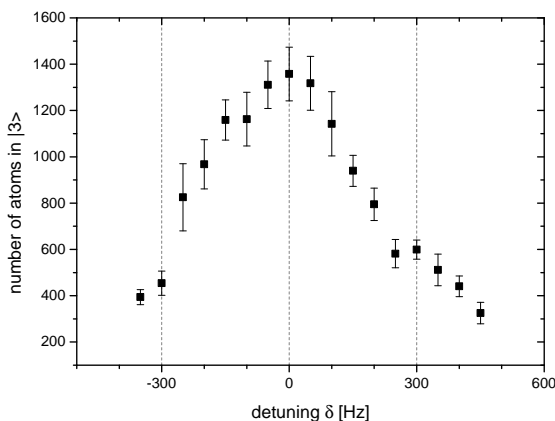


Figure 4.15.: **RF-tomography for a mBEC in the pancake traps.** The transferred number of atoms into state $|3\rangle$ is plotted versus the applied rf-frequency - given as the detuning δ relative to the center pancake resonance frequency. Each data point is an average of about 10 shots and the error bars are given by the standard error of the mean. Almost all atoms are in the center pancake with only a small population in the off-center pancakes.

of the atoms into the center pancake and thus with this technique we are already close to loading a single pancake. However there are still some atoms in the adjacent pancakes and the direct loading technique can only be done with a mBEC which is not desirable for some of the envisioned experiments.

Post-Selection of a Single Pancake

The other possibility to obtain only a single populated pancake is to selectively remove the atoms from all but one pancakes after the transfer. This can be done in several ways: either one transfers the atoms from the off-center pancakes into a third unoccupied state and then empties them using a resonant imaging pulse which 'kicks' the atoms out of the trap or one uses a third hyperfine state (e.g. $|3\rangle - |6\rangle$) to create a three-component mixture where the atoms are then lost due to

inelastic collisions. Both post-selection methods rely on a sufficient separation of the pancakes in frequency space in order to exclude the center pancake when doing the transfers. Currently the frequency separation and thus the rf-resolution is limited by the applicable magnetic field gradient with the MOT coils. The power supply we used for the measurements in this thesis was a Voltcraft SPS 1560 PFC which can supply a voltage up to 15 V and can drive currents up to 60 A. With our MOT coil setup we are limited by the maximal voltage of the power supply as we can only drive currents up to approximately 32 A. Therefore to be able to drive larger gradients in the future, we are currently exchanging this power supply for a Delta Elektronika SM45-70 B. It can supply voltages up to 45 V and drive currents up to 75 A. Therefore we should be able to increase the gradient for short times by up to a factor of three compared to our previous measurements.

In order to get a feeling on how a larger magnetic field gradient would affect the tomographic measurement, we scaled our results from Section 4.5 by this increased gradient as can be seen in Figure 4.16. As one can see already with a scaling factor of two (blue curve) and thus twice the current we should be able to separate the pancakes sufficiently to do the post-selection to obtain a single pancake. In

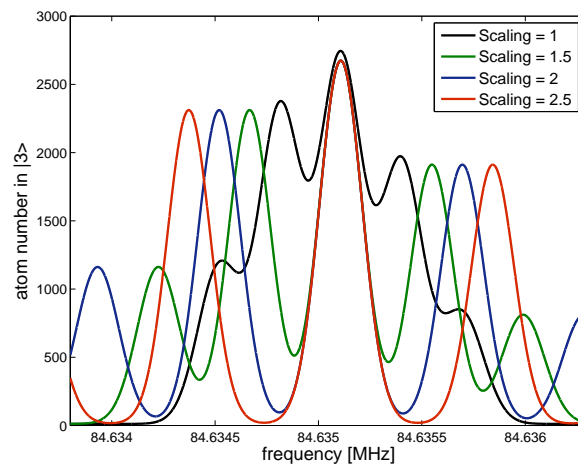


Figure 4.16.: **Effect of a larger gradient on the rf-tomography.** The black curve is our measured result (see Section 4.5). The colored curves show how this measurement would look like if one could apply a by the scaling factor larger gradient. Already an increase of the gradient by a factor of two should be sufficient to separate the pancakes well enough to selectively remove the off-center pancakes without affecting the center pancake.

conclusion, using the rf-tomography we showed that we load at most five pancakes with a degenerate Fermi gas and three pancakes with a mBEC where a large fraction is already in the center pancake. With the techniques described in this chapter we should thus be able to prepare a degenerate Fermi gas or mBEC in a single pancake as soon as the new power supply is tested. In combination with the lattice beams which are currently set up, this will enable us to start our investigation of the physics

4. Characterization of the Pancake Trap

in a single two-dimensional lattice very soon.

5. Conclusion and Outlook

During the course of this thesis we implemented the optical setup to create the pancake shaped quasi 2D dipole traps and set up the power stabilization for the pancake beam. In addition we also measured the laser noise to check that we are not limited by noise induced heating in the experiment.

After being able to load atoms into the vertical lattice of these pancake traps, we performed a Kapitza-Dirac diffraction measurement on a mBEC. The presence of the vertical lattice was beautifully observable and we used the measurement to verify our pancake spacing of about $4\ \mu\text{m}$ as well as estimate the trap depth. Comparing the estimated trap depth to a calculation, this was used as a further alignment tool for the pancake trap. Our next goal was then to see how many of the pancakes we load and what the populations in each are. Therefore we used a radio-frequency tomographic measurement. For this we loaded a single spin state of a Fermi gas into several pancakes and applied a magnetic field gradient with the MOT coils. This shifted the resonance frequency in each pancake and it was possible to selectively transfer atoms in each pancake into a previously unoccupied state which was then imaged using in-situ absorption imaging. This enabled us to count the population in each pancake and gave us a tool to detect how many pancakes we load. In addition, from fluctuations of the pancake positions during a run and from a repeat of the measurement after a week had passed, we were able to estimate the short and long term stability of the pancake trap position. We measured that the short term phase stability during a run was on the order of $\Delta\phi \leq \pi/12$ and that long term drifts were smaller than $\Delta\phi \leq \pi/8$. Since these phase drifts are much smaller than half the pancake spacing $\Delta\phi = \pi/2$, this should enable us to repeatedly load the same pancakes and thus implement a method to deterministically prepare an ultracold Fermi gas in a single pancake by removing the atoms in all but one pancake after the transfer. But we also observed that in order to implement such a method, we need a larger magnetic field gradient to separate the pancakes completely in frequency space and therefore we implemented recently a new power supply for our MOT coils with which we can drive such gradients.

After moving the experiment to our new labs in December, we began to set up the experiment again and were able to transfer atoms into the pancake traps in March. After realigning the pancake traps with the optical dipole trap, we characterized these in more detail than before the move, measuring the trap frequencies and the lifetime.

The measurement of the trap frequencies resulted in an aspect ratio $\omega_x : \omega_y : \omega_z \approx 1.2 : 1 : 357$, thus confirming that the traps are almost round and show only a slight ellipticity as well as proofing the tight confinement in the vertical axis. The lifetime in the trap was measured to be on the order of 50 s. We estimated the effect of hole heating and concluded that we should be able to observe the lattice dynamics before

heating becomes too severe.

In addition, we did the rf-tomography also with a mBEC in the trap and observed that we can load almost all atoms in a single pancake with only a small population in the off-center pancakes.

While writing this thesis, the first lattice beam was already set up and atoms have been successfully trapped in this lattice beam. In addition, the new power supply for the MOT coils was installed which allows us to apply stronger magnetic field gradients and therefore should enable us to prepare a single pancake in the near future due to the improved rf-resolution. Furthermore, microwave transitions into the low-field seeking states $|4\rangle - |6\rangle$ have been successfully driven with the implemented rf-setup and the second lattice beam is currently being set up.

Outlook

In the near future, as soon as the second lattice beam is set up we should be able to load atoms into a single layer of a quasi two-dimensional optical lattice. This will allow us to investigate the physics in the lattice directly when imaging in the top-down axis without the need of averaging over many realizations of the lattice. Therefore we will also implement a new objective (see Figure 5.1) into the experiment soon which will increase the resolution for the top-down imaging. This objective was designed both for $\lambda = 671\text{ nm}$ and $\lambda = 1064\text{ nm}$ light and thus it will also be possible to project a custom lattice via a spatial light modulator into the pancake layer. We plan to implement this in the future to prepare custom lattice geometries which we can change during the experiment and which will in combination with the increased resolution enable us to obtain a single-site resolution for the lattice. By

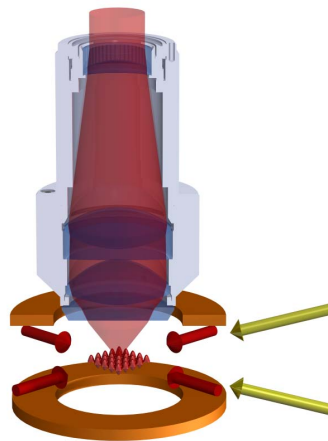


Figure 5.1.: **Illustration of the new objective with the optical lattice.** The new objective was designed both for $\lambda = 671\text{ nm}$ and $\lambda = 1064\text{ nm}$ light and thus one can also project a custom lattice via a spatial light modulator into the pancake plane. One can see that the objective is mounted very close to the Feshbach coils, which allows for the large numerical aperture and thus high resolution. The picture is taken from [Rie10].

loading first a two-component mixture into the lattice, we hope to see the transition from a superfluid into a fermionic Mott-insulator in-situ via the density profile¹. So far the transition to the fermionic Mott-insulator state has only been shown indirectly by measuring e.g. the double occupancy or the compressibility of the cloud [Jör08, Sch08]. After that we want to start investigating a three-component mixture in the 2D optical lattice where we hope to observe effects like Quantum Zeno loss-blocking, color superfluid phases or off-site trions [Kan09, Poh13].

¹Compare to [Gem09] for the bosonic case.

A. Fundamental Constants and Properties of Lithium

The following table shows a list of the constants which are used throughout this thesis. The fundamental constants are taken from [NIS] whereas the properties of the D₂ line of ⁶Li can be found in [Geh03].

Symbol	Value	Meaning
\hbar	$1.054571628 \times 10^{-34}$ Js	Planck's constant over 2π
h	$6.62606896 \times 10^{-34}$ Js	Planck's constant
c	2.99792458×10^8 m/s	Speed of light in vacuum
k_B	$1.3806504 \times 10^{-23}$ JK ⁻¹	Boltzmann's constant
a_0	$0.52917720859 \times 10^{-10}$ m	Bohr's radius
ϵ_0	$8.854187817 \times 10^{-12}$ Fm ⁻¹	Electric constant
m_e	$9.10938215 \times 10^{-31}$ kg	Mass of a electron
m_{Li}	$9.98834146 \times 10^{-27}$ kg	Mass of a ⁶ Li atom
Γ_{Li}	$2\pi \cdot 5.8724 \times 10^6$ s ⁻¹	Natural linewidth of the D ₂ line of ⁶ Li
λ_{Li}	$670.977338 \times 10^{-9}$ m	Wavelength of the D ₂ line of ⁶ Li in vacuum
T_{rec}	$3.53581152 \times 10^{-6}$ K	Recoil temperature of the D ₂ line of ⁶ Li
I_S	$25.4 \times \text{Wm}^{-2}$	Saturation intensity of the D ₂ line of ⁶ Li

B. Noise Characterization of the NUFERN

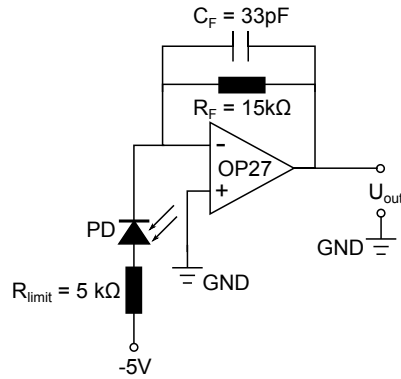


Figure B.1.: **Schematic of the photodiode circuit.** The photodiode is operated with a reverse bias voltage of -5 V . A resistor $R_{\text{limit}} = 5\text{ k}\Omega$ is put in front of the diode to limit the achievable current and thus protect the photodiode. At small photo currents the voltage drop across this resistor is negligible and the complete voltage is applied at the photodiode for reversed bias. An operational amplifier OP27 with an RC-feedback converts the photo current into an output voltage $U_{\text{out}} = R_F \cdot I_{\text{photo}}$. As feedback parameters we chose $R_F = 15\text{ k}\Omega$ and $C_F = 33\text{ pF}$. This leads to a 3dB-bandwidth of the transimpedance amplifier of $f_{-3\text{dB}} = \frac{1}{2\pi R_F C_F} \approx 3.2\text{ MHz}$ which is sufficient for our applications.

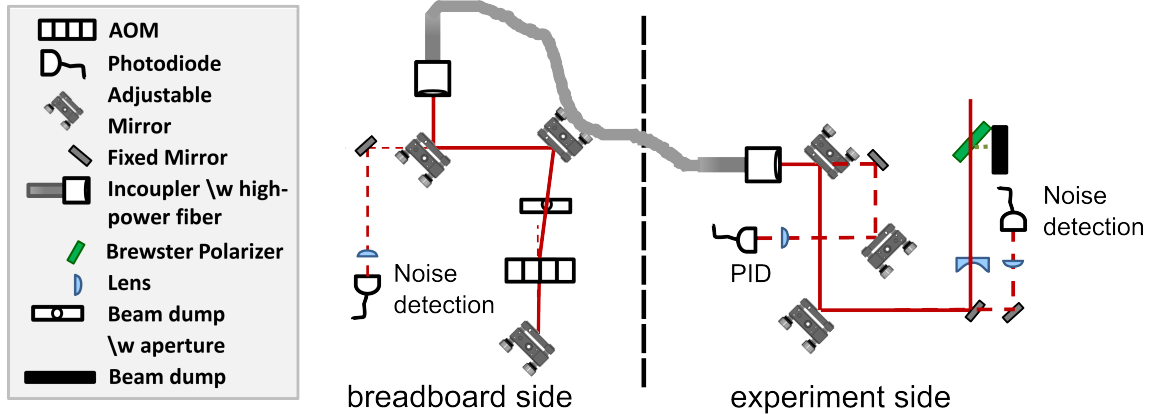


Figure B.2.: **Sketch of the position of the noise detection for the NUFERN.** The beam was focused on the photodiode such that its focal size was smaller than the active area of the photodiode. The lens was mounted on an adjustable lens tube to gain control of the beam position in the x-y-plane.

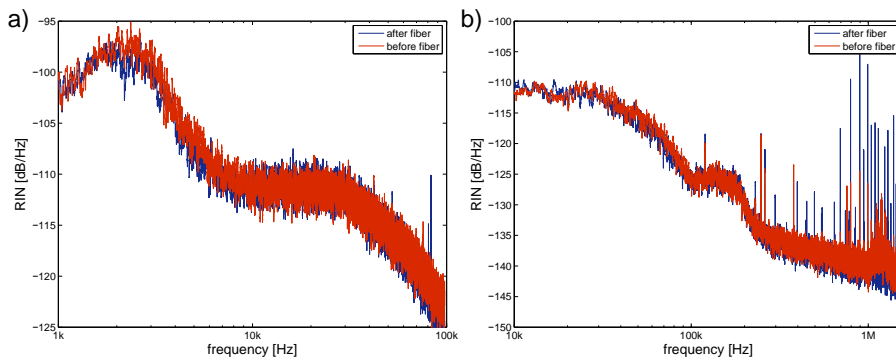


Figure B.3.: **RIN measurement of the NUFERN noise in front and after the high power fiber.** a) Sampling frequency $f_s = 196.315$ kHz and moving average over a span of 31 Hz. b) Sampling frequency $f_s = 3.125$ MHz and moving average over a span of 500 Hz. The NUFERN was free running at $P = 25$ W. The red data points were obtained detecting the beam before going through the high-power fiber whereas the blue data points were obtained detecting the beam after the high-power fiber. One can see that the high-power fiber has no effect on the laser noise.

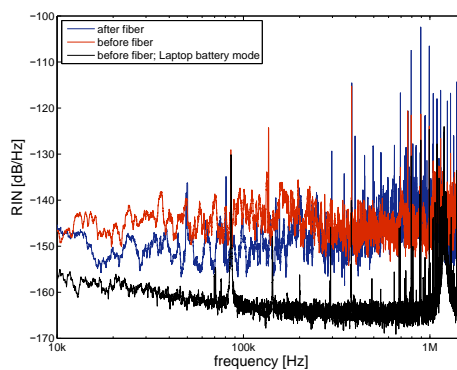


Figure B.4.: **RIN measurement of the photodiode background noise in front and after the high power fiber.** The sampling frequency was $f_s = 3.125$ MHz and a moving average was taken over a span of 500 Hz to smooth the curves. The spikes stem from a ground loop between the photodiode box and the laptop where the TiePie is connected. The photodiode box was grounded on the optical table whereas the laptop was grounded via its power supply. Thus the spikes depend on the detection position and they are larger after the fiber (blue) than in front of the fiber (red). When the power supply of the laptop was removed, the overall noise floor was decreased and the spikes become less pronounced (black).

Bibliography

- [Alt66] S. Altshuler, L. M. Frantz, R. Braunstein, *Reflection of Atoms from Standing Light Waves*, Phys. Rev. Lett. **17**, 231–232 (Aug 1966).
- [And95] M. H. Anderson, J. R. Ensher, M. R. Matthews, C. E. Wieman, E. A. Cornell, *Observation of Bose-Einstein Condensation in a Dilute Atomic Vapor*, Science **269**(5221), 198–201 (1995).
- [Bar57] J. Bardeen, L. N. Cooper, J. R. Schrieffer, *Theory of Superconductivity*, Phys. Rev. **108**, 1175–1204 (Dec 1957).
- [Bar04a] M. Bartenstein, A. Altmeyer, S. Riedl, S. Jochim, C. Chin, J. H. Denschlag, R. Grimm, *Collective Excitations of a Degenerate Gas at the BEC-BCS Crossover*, Phys. Rev. Lett. **92**, 203201 (May 2004).
- [Bar04b] M. Bartenstein, A. Altmeyer, S. Riedl, S. Jochim, C. Chin, J. H. Denschlag, R. Grimm, *Crossover from a Molecular Bose-Einstein Condensate to a Degenerate Fermi Gas*, Phys. Rev. Lett. **92**, 120401 (Mar 2004).
- [Ber13] A. Bergschneider, *Master Thesis* (to be published June 2013).
- [Boh12] J. Bohn, *Towards an ultracold three-component Fermi Gas in a two-dimensional optical lattice*, Diploma thesis (2012).
- [Bra03] B. H. Bransden, C. J. Joachain, *Physics of atoms and molecules* (Pearson education, 2003).
- [Chi04] C. Chin, M. Bartenstein, A. Altmeyer, S. Riedl, S. Jochim, J. H. Denschlag, R. Grimm, *Observation of the Pairing Gap in a Strongly Interacting Fermi Gas*, Science **305**(5687), 1128–1130 (2004).
- [Chi10] C. Chin, R. Grimm, P. Julienne, E. Tiesinga, *Feshbach resonances in ultracold gases*, Rev. Mod. Phys. **82**, 1225–1286 (Apr 2010).
- [Dal99] J. Dalibard, *Collisional dynamics of ultra-cold atomic gases*, in *Proceedings of the International School of Physics-Enrico Fermi*, Vol. 321 (1999).
- [Dal09] A. J. Daley, J. M. Taylor, S. Diehl, M. Baranov, P. Zoller, *Atomic Three-Body Loss as a Dynamical Three-Body Interaction*, Phys. Rev. Lett. **102**, 040402 (Jan 2009).
- [Dav95] K. B. Davis, M. O. Mewes, M. R. Andrews, N. J. van Druten, D. S. Durfee, D. M. Kurn, W. Ketterle, *Bose-Einstein Condensation in a Gas of Sodium Atoms*, Phys. Rev. Lett. **75**, 3969–3973 (Nov 1995).

- [Dav97] C. C. Davis, A. Yu, *Lasers and Electro-Optics*, Vol. 36 (International Society for Optics and Photonics, 1997).
- [DeM99] B. DeMarco, D. S. Jin, *Onset of Fermi Degeneracy in a Trapped Atomic Gas*, *Science* **285**(5434), 1703–1706 (1999).
- [DeM01] B. DeMarco, S. B. Papp, D. S. Jin, *Pauli Blocking of Collisions in a Quantum Degenerate Atomic Fermi Gas*, *Phys. Rev. Lett.* **86**, 5409–5412 (Jun 2001).
- [Ein25] A. Einstein, *Quantentheorie des einatomigen idealen Gases. Zweite Abhandlung*, *Sitzungsberichte der preussischen Akademie der Wissenschaften* **1** (1925).
- [Fes58] H. Feshbach, *Unified theory of nuclear reactions*, *Annals of Physics* **5**(4), 357 – 390 (1958).
- [Fey82] R. P. Feynman, *Simulating physics with computers*, *International journal of theoretical physics* **21**(6), 467–488 (1982).
- [Fre01] D. L. Freimund, K. Aflatooni, H. Batelaan, *Observation of the Kapitza-Dirac effect*, *Nature* **413**(6852), 142–143 (2001).
- [Fre02] D. L. Freimund, H. Batelaan, *Bragg scattering of free electrons using the Kapitza-Dirac effect*, *Physical review letters* **89**(28), 283602 (2002).
- [Gad09] B. Gadway, D. Pertot, R. Reimann, M. G. Cohen, D. Schneble, *Analysis of Kapitza-Dirac diffraction patterns beyond the Raman-Nath regime*, *Optics Express* **17**(21), 19173–19180 (2009).
- [Geh98] M. E. Gehm, K. M. O’Hara, T. A. Savard, J. E. Thomas, *Dynamics of noise-induced heating in atom traps*, *Phys. Rev. A* **58**, 3914–3921 (Nov 1998).
- [Geh03] M. E. Gehm, *Properties of ^6Li* , Jetlab, (2003).
- [Gem09] N. Gemelke, X. Zhang, C.-L. Hung, C. Chin, *In situ observation of incompressible Mott-insulating domains in ultracold atomic gases*, *Nature* **460**(7258), 995–998 (2009).
- [Gio08] S. Giorgini, L. P. Pitaevskii, S. Stringari, *Theory of ultracold atomic Fermi gases*, *Rev. Mod. Phys.* **80**, 1215–1274 (Oct 2008).
- [Gou86] P. L. Gould, G. A. Ruff, D. E. Pritchard, *Diffraction of atoms by light: The near-resonant Kapitza-Dirac effect*, *Physical review letters* **56**(8), 827–830 (1986).
- [Gre02] M. Greiner, O. Mandel, T. Esslinger, T. W. Hänsch, I. Bloch, *Quantum phase transition from a superfluid to a Mott insulator in a gas of ultracold atoms*, *Nature* **415**(6867), 39–44 (2002).

-
- [Gre03] M. Greiner, C. A. Regal, D. S. Jin, *Emergence of a molecular Bose–Einstein condensate from a Fermi gas*, *Nature* **426**(6966), 537–540 (2003).
- [Gri93] G. F. Gribakin, V. V. Flambaum, *Calculation of the scattering length in atomic collisions using the semiclassical approximation*, *Phys. Rev. A* **48**, 546–553 (Jul 1993).
- [Gri96] A. Griffin, *Conserving and gapless approximations for an inhomogeneous Bose gas at finite temperatures*, *Phys. Rev. B* **53**, 9341–9347 (Apr 1996).
- [Gri00] R. Grimm, M. Weidemüller, Y. B. Ovchinnikov, *Optical dipole traps for neutral atoms*, *Advances in atomic, molecular, and optical physics* **42**, 95–170 (2000).
- [Her08] I. V. Hertel, C.-P. Schulz, *Atome, Moleküle und Optische Physik 1: Atomphysik und Grundlagen der Spektroskopie* (Springer Verlag, 2008).
- [Heu11] S. Heupts, *A new radio frequency setup to manipulate spin mixtures of fermionic atoms*, Bachelor thesis (September 2011).
- [Hol00] M. J. Holland, B. DeMarco, D. S. Jin, *Evaporative cooling of a two-component degenerate Fermi gas*, *Phys. Rev. A* **61**, 053610 (Apr 2000).
- [Huc09] J. Huckans, I. Spielman, B. L. Tolra, W. Phillips, J. Porto, *Quantum and classical dynamics of a Bose-Einstein condensate in a large-period optical lattice*, *Physical Review A* **80**(4), 043609 (2009).
- [Ino98] S. Inouye, M. Andrews, J. Stenger, H.-J. Miesner, D. Stamper-Kurn, W. Ketterle, *Observation of Feshbach resonances in a Bose–Einstein condensate*, *Nature* **392**(6672), 151–154 (1998).
- [Jac75] J. Jackson, *Classical electrodynamics* (Wiley, 1975).
- [Joc03] S. Jochim, M. Bartenstein, A. Altmeyer, G. Hendl, S. Riedl, C. Chin, J. Hecker Denschlag, R. Grimm, *Bose-Einstein Condensation of Molecules*, *Science* **302**(5653), 2101–2103 (2003).
- [Joc04] S. Jochim, *Bose-Einstein Condensation of Molecules*, Dissertation, Universität Innsbruck (2004).
- [Jof93] M. A. Joffe, W. Ketterle, A. Martin, D. E. Pritchard, *Transverse cooling and deflection of an atomic beam inside a Zeeman slower*, *J. Opt. Soc. Am. B* **10**(12), 2257–2262 (Dec 1993).
- [Jör08] R. Jördens, N. Strohmaier, K. Günter, H. Moritz, T. Esslinger, *A Mott insulator of fermionic atoms in an optical lattice*, *Nature* **455**(7210), 204–207 (2008).
- [Kan09] A. Kantian, M. Dalmonte, S. Diehl, W. Hofstetter, P. Zoller, A. J. Daley, *Atomic Color Superfluid via Three-Body Loss*, *Phys. Rev. Lett.* **103**, 240401 (Dec 2009).

- [Kap33] P. Kapitza, P. Dirac, *The reflection of electrons from standing light waves*, in *Mathematical Proceedings of the Cambridge Philosophical Society*, Vol. 29, 297–300, Cambridge Univ Press (1933).
- [Ket99] W. Ketterle, D. S. Durfee, D. M. Stamper-Kurn, *Making, probing and understanding Bose-Einstein condensates*, in: M. Inguscio, S. Stringari and C. Wiemann (Eds.); *Bose-Einstein Condensation in Atomic Gases*, IOS Press (1999).
- [Ket08] W. Ketterle, M. W. Zwierlein, *Making, probing and understanding ultracold Fermi gases*, in: M. Inguscio, W. Ketterle, and C. Salomon (Eds.); *Ultracold Fermi Gases*, Proceedings of the International School of Physics - Enrico Fermi **Course CLXIV**, IOS Press (2008).
- [Kin04] J. Kinast, S. L. Hemmer, M. E. Gehm, A. Turlapov, J. E. Thomas, *Evidence for Superfluidity in a Resonantly Interacting Fermi Gas*, *Phys. Rev. Lett.* **92**, 150402 (Apr 2004).
- [Kin05] J. Kinast, A. Turlapov, J. E. Thomas, Q. Chen, J. Stajic, K. Levin, *Heat Capacity of a Strongly Interacting Fermi Gas*, *Science* **307**(5713), 1296–1299 (2005).
- [Lan81] L. D. Landau, L. M. Lifshitz, *Quantum Mechanics* (Butterworth Heine-
mann, 1981), 3rd Edn.
- [Lom08] T. Lompe, *An apparatus for the production of molecular Bose-Einstein condensates*, Diploma thesis (2008).
- [Lom10a] T. Lompe, T. B. Ottenstein, F. Serwane, K. Viering, A. N. Wenz, G. Zürn, S. Jochim, *Atom-Dimer Scattering in a Three-Component Fermi Gas*, *Phys. Rev. Lett.* **105**, 103201 (Sep 2010).
- [Lom10b] T. Lompe, T. B. Ottenstein, F. Serwane, A. N. Wenz, G. Zürn, S. Jochim, *Radio-Frequency Association of Efimov Trimers*, *Science* **330**(6006), 940–944 (2010).
- [McK11] D. C. McKay, B. DeMarco, *Cooling in strongly correlated optical lattices: prospects and challenges*, *Reports on Progress in Physics* **74**(5), 054401 (2011).
- [Mep] Mephisto, http://www.coherent.com/downloads/Mephisto_CoherentDatasheet_Jan2013.pdf
- [Met99] H. J. Metcalf, P. Van der Straten, *Laser cooling and trapping* (Springer Verlag, 1999).
- [Moe95] A. Moerdijk, B. Verhaar, A. Axelsson, *et al.*, *Resonances in ultracold collisions of 6Li , 7Li , and 23Na* , *Physical Review-Section A-Atomic Molecular and Optical Physics* **51**(6), 4852–4861 (1995).
- [Mot37] N. F. Mott, R. Peierls, *Discussion of the paper by de Boer and Verwey*, *Proceedings of the Physical Society* **49**(4S), 72 (1937).

-
- [NIS] NIST, <http://physics.nist.gov/cuu/Constants/>.
- [O'H02] K. M. O'Hara, S. L. Hemmer, M. E. Gehm, S. R. Granade, J. E. Thomas, *Observation of a Strongly Interacting Degenerate Fermi Gas of Atoms*, *Science* **298**(5601), 2179–2182 (2002).
- [Ott08] T. B. Ottenstein, T. Lompe, M. Kohnen, A. N. Wenz, S. Jochim, *Collisional Stability of a Three-Component Degenerate Fermi Gas*, *Phys. Rev. Lett.* **101**, 203202 (Nov 2008).
- [Ovc99] Y. B. Ovchinnikov, J. Müller, M. Doery, E. Vredenburg, K. Helmerson, S. Rolston, W. Phillips, *Diffraction of a released Bose-Einstein condensate by a pulsed standing light wave*, *Physical review letters* **83**(2), 284–287 (1999).
- [Par05] G. B. Partridge, K. E. Strecker, R. I. Kamar, M. W. Jack, R. G. Hulet, *Molecular Probe of Pairing in the BEC-BCS Crossover*, *Phys. Rev. Lett.* **95**, 020404 (Jul 2005).
- [Pet03] D. S. Petrov, *Three-body problem in Fermi gases with short-range inter-particle interaction*, *Phys. Rev. A* **67**, 010703 (Jan 2003).
- [Pet04] D. S. Petrov, C. Salomon, G. V. Shlyapnikov, *Weakly Bound Dimers of Fermionic Atoms*, *Phys. Rev. Lett.* **93**, 090404 (Aug 2004).
- [Pet05] D. S. Petrov, C. Salomon, G. V. Shlyapnikov, *Scattering properties of weakly bound dimers of fermionic atoms*, *Phys. Rev. A* **71**, 012708 (Jan 2005).
- [Poh13] J. Pohlmann, A. Privitera, I. Titvinidze, W. Hofstetter, *Trion and dimer formation in three-color fermions*, *Phys. Rev. A* **87**, 023617 (Feb 2013).
- [Pri11] A. Privitera, I. Titvinidze, S.-Y. Chang, S. Diehl, A. J. Daley, W. Hofstetter, *Loss-induced phase separation and pairing for three-species atomic lattice fermions*, *Phys. Rev. A* **84**, 021601 (Aug 2011).
- [Rap07] A. Rapp, G. Zaránd, C. Honerkamp, W. Hofstetter, *Color Superfluidity and “Baryon” Formation in Ultracold Fermions*, *Phys. Rev. Lett.* **98**, 160405 (Apr 2007).
- [Rap08] A. Rapp, W. Hofstetter, G. Zaránd, *Trionic phase of ultracold fermions in an optical lattice: A variational study*, *Phys. Rev. B* **77**, 144520 (Apr 2008).
- [Ric95] L. Ricci, M. Weidemüller, T. Esslinger, A. Hemmerich, C. Zimmermann, V. Vuletic, W. König, T. W. Hänsch, *A compact grating-stabilized diode laser system for atomic physics*, *Optics Communications* **117**(5), 541–549 (1995).
- [Rie10] M. Ries, *A magneto-optical trap for the preparation of a three-component Fermi gas in an optical lattice*, Diploma thesis (2010).

- [Sak11] J. J. J. Sakurai, J. Napolitano, *Modern quantum mechanics* (ADDISON WESLEY Publishing Company Incorporated, 2011).
- [Sal07] B. E. Saleh, M. C. Teich, *Fundamentals of photonics* (2007).
- [Sch04] F. Schwabl, *Quantenmechanik (Qm I): Eine Einführung* (Springer New York, 2004).
- [Sch08] U. Schneider, L. Hackermüller, S. Will, T. Best, I. Bloch, T. A. Costi, R. W. Helmes, D. Rasch, A. Rosch, *Metallic and Insulating Phases of Repulsively Interacting Fermions in a 3D Optical Lattice*, *Science* **322**(5907), 1520–1525 (2008).
- [Ser07] F. Serwane, *The setup of a magneto optical trap for the preparation of a mesoscopic degenerate Fermi gas*, Diploma thesis (2007).
- [Ser11] F. Serwane, *Deterministic preparation of a tunable few-fermion system*, Dissertation (2011).
- [Sim10] P. Simon, *Apparatus for the preparation of ultracold Fermi gases*, Diploma thesis (2010).
- [Sta12] J. Stachurska, *An optical dipole trap for two-dimensional confinement of lithium atoms*, Bachelor thesis (2012).
- [Tim01] E. Timmermans, *Degenerate Fermion Gas Heating by Hole Creation*, *Phys. Rev. Lett.* **87**, 240403 (Nov 2001).
- [Tre11] A. Trenkwalder, C. Kohstall, M. Zaccanti, D. Naik, A. I. Sidorov, F. Schreck, R. Grimm, *Hydrodynamic Expansion of a Strongly Interacting Fermi-Fermi Mixture*, *Phys. Rev. Lett.* **106**, 115304 (Mar 2011).
- [Wei09] M. Weidemüller, C. Zimmermann, *Cold atoms and molecules* (Wiley-VCH, 2009).
- [Wei11] M. Weidemüller, C. Zimmermann, *Interactions in ultracold gases: from atoms to molecules* (Wiley-VCH, 2011).
- [Wen08] A. N. Wenz, *Few-Body Physics in a Three-Component Fermi Gas*, Diploma thesis (2008).
- [Wen09] A. N. Wenz, T. Lompe, T. B. Ottenstein, F. Serwane, G. Zürn, S. Jochim, *Universal trimer in a three-component Fermi gas*, *Phys. Rev. A* **80**, 040702 (Oct 2009).
- [Wil07] F. Wilczek, *Quantum chromodynamics: Lifestyles of the small and simple*, *Nature Physics* **3**(6), 375–376 (2007).
- [Wol] Wolfram, <http://mathworld.wolfram.com/Wiener-KhinchinTheorem.html>.
- [Zür09] G. Zürn, *Realization of an Optical Microtrap for a Highly Degenerate Fermi Gas*, Diploma thesis (2009).

- [Zür12] G. Zürn, *Few-fermion systems in one dimension*, Dissertation (2012).
- [Zür13] G. Zürn, T. Lompe, A. N. Wenz, S. Jochim, P. S. Julienne, J. M. Hutson, *Precise Characterization of ^6Li Feshbach Resonances Using Trap-Sideband-Resolved RF Spectroscopy of Weakly Bound Molecules*, Phys. Rev. Lett. **110**, 135301 (Mar 2013).
- [Zwi03] M. W. Zwierlein, C. A. Stan, C. H. Schunck, S. M. F. Raupach, S. Gupta, Z. Hadzibabic, W. Ketterle, *Observation of Bose-Einstein Condensation of Molecules*, Phys. Rev. Lett. **91**, 250401 (Dec 2003).
- [Zwi05] M. W. Zwierlein, J. R. Abo-Shaeer, A. Schirotzek, C. H. Schunck, W. Ketterle, *Vortices and superfluidity in a strongly interacting Fermi gas*, Nature **435**(7045), 1047–1051 (2005).

Danksagung

An dieser Stelle bedanke ich mich bei allen die zum Gelingen dieser Arbeit beigetragen haben:

Zuallererst bei Selim für die hervorragende Betreuung dieser Arbeit. Er war bei Fragen und Problemen immer ansprechbar und hat wertvollen Input gegeben. Seine motivierende Art macht das Arbeiten in seiner Gruppe sehr angenehm.

Bei allen Mitgliedern der Gruppe: Andrea, Andre, Martin, Thomas, Gerhard, Simon, Puneeth, Vincent, Jan Hendrik, Sebastian, Nils und Sven. Durch eure Geduld und Erklärungen habe ich das Experiment von Kopf bis Fuß kennen gelernt und konnte in dieser Zeit einiges lernen. Von den täglichen Tisch-Kicker Duellen über die vielen mitgebrachten Kuchen bis hin zum Doktorhut bauen ... mit euch kam der Spaß nie zu kurz. Danke auch noch einmal an Andre, Martin, Thomas und Gerhard, die sich durch die Korrektur dieser Arbeit gekämpft haben.

Bei den ehemaligen Mitgliedern Johanna und Juliana für die Vorarbeit die sie beim Bau und Test der neuen ‚Pancake‘ Falle geleistet haben; dadurch war der Einbau ins Experiment fast nur noch Plug&Play.

Bei Prof. Markus Oberthaler für die Zweitkorrektur dieser Arbeit.

Bei Sebastian fürs Korrekturlesen der Arbeit.

Bei der PI Werkstatt, insbesondere Herrn Ziegler, die unsere neuen Labore super vorbereitet und uns so einen reibungslosen Umzug ermöglicht haben.

Bei der Fa. Hasenkamp, die unsere optischen Tische mitsamt den aufgebauten Experimenten ohne Blessuren ins Neuenheimer Feld gebracht hat.

Und zu guter Letzt bei Nathalie: Danke!

Erklärung

Ich versichere, dass ich diese Arbeit selbstständig verfasst und keine anderen als die angegebenen Quellen und Hilfsmittel benutzt habe.

Heidelberg, den 12.05.2013

.....
(Unterschrift)